

**Triphenylamine based semiconducting polymers for
organic/hybrid photovoltaics and sensors**

DISSERTATION

zur Erlangung des akademischen Grades
eines Doktors der Naturwissenschaften (Dr. rer. nat.)
im Promotionsprogramm
Photophysik synthetischer und multichromophorer Systeme
der Bayreuther Graduiertenschule für Mathematik und Naturwissenschaft

vorgelegt von

Katharina Ulrike Elfriede Neumann

geboren in Naila / Deutschland

Bayreuth, 2014

Die vorliegende Arbeit wurde in der Zeit von Oktober 2010 bis Juni 2014 in der Arbeitsgruppe Angewandte Funktionspolymere am Lehrstuhl für Makromolekulare Chemie I der Universität Bayreuth unter der Betreuung von Prof. Dr. Mukundan Thelakkat angefertigt.

Amtierender Direktor der Graduiertenschule: Prof. Dr. Franz X. Schmid

Datum der Einreichung: 30.06.2014

Datum des wissenschaftlichen Kolloquiums: 25.07.2014

Prüfungsausschuss:

Prof. Dr. Mukundan Thelakkat	(Erstgutachter)
Prof. Dr. Peter Strohrigl	(Zweitgutachter)
Prof. Dr. Markus Retsch	(Vorsitz)
Prof. Dr. Anna Köhler	

Für meine Familie

*“Ich bin immer noch verwirrt,
aber auf einem höheren Niveau”*

Enrico Fermi

Table of contents

1	Summary	1
2	Introduction	7
3	Objective of the thesis	47
4	Overview of the thesis	49
5	Crystallization-driven phase separation towards one pot fabrication of bilayer perovskite/polymer solar cells	61
6	Perovskite Solar Cells Involving Poly(tetraphenylbenzidine)s: Investigation of Hole Carrier Mobility, Doping effects and Photovoltaic Properties	75
7	Undoped and doped Poly(tetraphenylbenzidine) as Sensitive Material for an Impedimetric NO ₂ Gas Dosimeter	109
8	Influence of the Excited-State Charge-Transfer Character on the Exciton Dissociation in Donor–Acceptor Copolymers	119
9	Synthesis and characterization of donor-acceptor copolymers carrying triphenylamine units for photovoltaic applications	161
	List of publications	167
	Danksagung	169
	Erklärung	173

Summary

This thesis concerns the tailor-made synthesis of tetraphenylbenzidine (TPD) and triphenylamine (TPA) based organic semiconducting polymers and the investigation of the charge carrier transport, doping effects and the application in organic/hybrid photovoltaics and sensors. The specific design of TPD and TPA main-chain polymers enabled the use of this class of well-known hole transport materials for new applications such as injecting layers in perovskite solar cells and impedimetric gas sensors. Furthermore, a detailed study on the delocalization and charge-transfer (CT) character in donor-acceptor (D-A) copolymers was achieved through the design of D-A copolymers with different CT-character.

A great challenge in the field of perovskite solar cells, which are highly efficient and underwent an extraordinary development recently, is the uniform film formation resulting in big perovskite crystals and smooth surfaces. In the first part of this thesis, a one-pot fabrication method towards bilayer devices was developed to reach this goal. Hereto, the crystallization of the perovskite was guided within a polymer matrix. For that, a TPD homopolymer (PTPD) with oligo ethylene glycol side chains was designed and synthesized in order to obtain solubility and miscibility in the perovskite precursor ($\text{CH}_3\text{NH}_3\text{I} + \text{PbI}_2$) solution. In a single step, the blend solution containing PTPD and the perovskite precursors was spin coated. Through thermal annealing a crystallization driven vertical phase separation occurred and the desired bilayer structure (PTPD/perovskite) was formed. Big perovskite crystals with a smooth surface could be achieved, which offer an optimal geometry for efficient solar cells. It was demonstrated that solar cells prepared with this novel approach worked well with an underlying mesoporous TiO_2 layer as scaffold. Thus, this system is of great relevance for the emerging field of perovskite solar cells because it is a simple and scalable method leading to smooth and uniform crystal formation.

The second part deals with the influence of the polarity of the side chains of PTPDs acting as hole injecting layer at the interface to the perovskite layer. Therefore, perovskite solar cells were prepared using a commonly used two step method. First, a PbI_2 layer is prepared and immersed into a $\text{CH}_3\text{NH}_3\text{X}$ solution, annealed and second coated with a hole conductor. Important questions regarding the influence of properties of the hole conducting material are examined. In detail, the molecular weight dependence of the hole transport mobility in PTPDs was

investigated by space charge limited current (SCLC) measurements. It could be shown that the hole transport mobility is independent on the molecular weight for these amorphous polymers and the attachment of polar side chains does also not affect the hole transport behavior. Furthermore, SCLC, UV-vis, and spectroelectrochemical measurements revealed that the doping with a Co(III)-complex increases the charge carrier concentration via oxidation, which leads to an increased conductivity and therefore a better power conversion efficiency (PCE). The solar cells were characterized in detail taking into account the question of storage and hysteresis effects due to measurement conditions. After storing the devices, the PCE increased due to improved absorption leading to improved EQE. Additionally, the PTPD with polar side chains lead to a less pronounced hysteresis effect and a higher stability under illumination compared to the polymer carrying non-polar side chains.

In the third part PTPDs are presented as active materials for impedimetric NO₂ gas dosimeters. The advantage of gas dosimeters is the simultaneous detection of the actual concentration as well as the exposure in dependence of time. Therefore, the active material has to accumulate the analyte during exposure and no recovery of the signal after exposure has to occur. The PTPD is a suitable active material for the detection of NO₂ because of its oxidizability. The oxidation of the PTPD lead to a measureable change of the conductivity and resistivity. We showed that the pure, undoped PTPD behaves as a classical NO₂ sensor with a certain recovery of the sensor signal. However, the doping of the PTPD with a Co(III)-salt and the addition of a conducting Li-salt lead to a reduction of the recovery and the accumulation of NO₂ in the PTPD layer. Thus, the adsorption and desorption rates could be tailored by doping and addition of the conducting salt.

The fourth part addresses the question of tuning the absorption behavior of PTPDs and presents a detailed study of the influence of the chemical structure on delocalization in donor-acceptor copolymers. It is known in the literature that the optical gap can be reduced using the D-A concept. For the implementation of the D-A concept two strategies are known: 1) incorporation of the acceptor unit in the main chain in an alternating way and 2) attachment of the acceptor to the side chain of the polymer. These strategies were compared in this work to understand the influence on exciton delocalization and the effect of the CT-character on charge transport. Additionally, the charge separation in bilayer solar cells with C₆₀ was studied. Therefore, two novel D-A copolymers based on TPA as donor unit were synthesized. Cyclic voltammetry, UV-vis, fluorescence, and SCLC measurements revealed that the two D-A copolymers have a different degree of CT-character and delocalization. Thus, also the hole transport mobilities vary. We found that the strong exciton localization that exists in the D-A copolymer with acceptor in the side chain together with a lowered conjugation in this system hinders the charge separation with C₆₀. However, the weak CT-character and strong conjugation/delocalization in the D-A main-chain copolymer leads to improved charge separation in the bilayer solar cells.

Zusammenfassung

Diese Arbeit beschäftigt sich mit der maßgeschneiderten Synthese von organischen, halbleitenden Polymeren basierend auf Tetraphenylbenzidin (TPD) und Triphenylamin (TPA) und deren Untersuchung hinsichtlich des Ladungsträgertransports, des Einflusses von Dotierung und der Anwendung in organischen/Hybrid-Solarzellen und Sensoren. Das spezifische Design der TPD- und TPA-Hauptkettenpolymere ermöglicht die Nutzung dieser Materialklasse als namhafte Lochtransportmaterialien für neue Anwendungen wie den Einsatz als Injektionsschichten in Perovskit Solarzellen und als impedimetrische Gassensoren. Weiterhin wurde eine Studie über die Delokalisierung und den Ladungstransfercharakter in Donor-Akzeptor (D-A) Copolymeren durchgeführt, indem D-A Copolymere mit unterschiedlichem Ladungstransfercharakter konzipiert wurden.

Eine große Herausforderung auf dem Gebiet der hoch effizienten Perovskit Solarzellen, die bisher eine außergewöhnliche Entwicklung durchlaufen haben, ist eine gleichmäßige Filmbildung, die es ermöglicht große Perovskit-Kristalle und glatte Oberflächen zu erhalten. Um dieses Ziel zu erreichen, wurde im ersten Teil dieser Arbeit eine Eintopfmethod für die Herstellung von Zweischicht solarzellen entwickelt. Hierfür wurde die Kristallisation des Perovskits innerhalb einer Polymermatrix gesteuert. Daher wurde ein TPD Homopolymer (PTPD) mit Oligoethylenglykol-Seitenketten maßgeschneidert synthetisiert, um die nötige Löslichkeit und Mischbarkeit in der Lösung der Perovskit-Edukte ($\text{CH}_3\text{NH}_3\text{I}$ und PbI_2) zu erzielen. In einem einzigen Schritt wurde die Blend-Lösung aus PTPD und Perovskit-Edukten durch Lackschleudern aufgetragen. Durch anschließende thermische Behandlung trat eine kristallisationsgetriebene vertikale Phasenseparation auf und die gewünschte Zweischichtstruktur (PTPD/Perovskit) bildete sich aus. Große Perovskit-Kristalle mit einer glatten Oberfläche, welche eine optimale Geometrie für effiziente Solarzellen aufweisen, konnten erhalten werden. Die mit diesem neuen Ansatz hergestellten Solarzellen zeigten eine sehr gute Funktionsweise bei Verwendung einer unterliegenden, mesoporösen TiO_2 -Schicht als Gerüst. Daher ist dieses System von großer Relevanz für das aufstrebende Gebiet der Perovskit-Solarzellen, da es eine einfache und skalierbare Methode darstellt, um eine glatte und einheitliche Kristallbildung zu erzielen.

Der zweite Teil beschäftigt sich mit dem Einfluss der Polarität der Seitenkette der PTPDs als Lochinjektionsschicht an der Grenzfläche zur Perovskit-Schicht. Für diese Untersuchungen wurden Perovskit-Solarzellen mit Hilfe der gängigen, zweistufigen Methode hergestellt. Zunächst erfolgte die Herstellung der PbI_2 -Schicht, welche einer $\text{CH}_3\text{NH}_3\text{X}$ -Lösung ausgesetzt wurde. Nach einem Tempervorgang wurde im zweiten Schritt der Lochleiter aufgetragen.

Wichtige Fragestellungen im Hinblick auf den Einfluss der Eigenschaften des lochleitenden Materials wurden untersucht. Der Einfluss des Molekulargewichts auf die Lochtransportmobilität der PTPDs wurde mittels „Space charge limited current“ (SCLC) Messungen betrachtet. Es konnte gezeigt werden, dass die Lochtransportmobilität unabhängig vom Molekulargewicht dieser amorphen Polymere ist und die Anbindung von polaren Seitenketten das Lochtransportverhalten ebenfalls nicht beeinflusst. Weiterhin zeigten SCLC, UV-vis und spektroelektrochemische Messungen, dass durch Dotierung mit einem Co(III)-Komplex die Ladungsträgerkonzentration durch Oxidation erhöht wird, was zu einer erhöhten Leitfähigkeit und daher einem verbesserten Wirkungsgrad der Solarzellen führt. Die Solarzellen wurden im Detail charakterisiert, wobei Fragen der Lagerung und Hystereseeffekte aufgrund von Messbedingungen adressiert wurden. Nach Lagerung der Solarzellen erhöhte sich der Wirkungsgrad aufgrund der verbesserten Absorption, welche zu einer verbesserten externen Quantenausbeute führte. Zusätzlich resultierte der Einsatz von polaren Seitenketten am PTPD im Vergleich zum Polymer mit unpolaren Seitenketten in einem weniger stark ausgeprägten Hystereseeffekt und einer höheren Stabilität unter Beleuchtung.

Im dritten Teil dieser Arbeit werden PTPDs als aktive Materialien für impedimetrische NO₂-Gasdosimeter vorgestellt. Der Vorteil von Gasdosimetern ist die gleichzeitige Detektion der aktuellen Konzentration und der Exposition in Abhängigkeit der Zeit. Daher muss das aktive Material den Analyten während der Exposition akkumulieren und es darf keine Regeneration des Signals nach der Exposition auftreten. PTPD ist aufgrund seiner Oxidierbarkeit ein geeignetes aktives Material für die Detektion von NO₂. Die Oxidation des PTPDs führt zu einer messbaren Änderung der Leitfähigkeit und des Widerstands. Wir konnten zeigen, dass das reine, undotierte PTPD als klassischer Gassensor für NO₂ fungiert, wobei eine Regeneration des Sensorsignals auftritt. Allerdings führen die Dotierung des PTPDs mittels Co(III)-Komplex und die Zugabe eines Li-Leitsalzes zur Reduktion der Regeneration des Sensorsignals und einer Akkumulation von NO₂ in der PTPD-Schicht. Folglich wurden die Adsorptions- und Desorptionsraten durch Dotierung und Zugabe des Leitsalzes auf den Einsatz als Dosimetermaterial zugeschnitten.

Der vierte Teil beschäftigt sich mit der Frage der Variation des Absorptionsverhaltens von PTPDs und zeigt eine detaillierte Studie hinsichtlich des Einflusses der chemischen Struktur auf die Delokalisierung in D-A-Copolymeren. Aus der Literatur ist bekannt, dass die optische Lücke mit Hilfe des D-A-Konzepts reduziert werden kann. Zur Umsetzung des D-A-Konzepts sind zwei Strategien bekannt: 1) Alternierender Einbau der Akzeptoreinheit in die Polymerhauptkette und 2) Anbindung des Akzeptors an die Seitenkette des Polymers. Diese Strategien wurden in dieser Arbeit verglichen, um den Einfluss auf die Exzitationendelokalisierung und den Effekt des Ladungstransfercharakters auf den Ladungstransport zu verstehen. Zusätzlich wurde die

Ladungstrennung in Zweischichtsolarzellen mit C_{60} untersucht. Dafür wurden zwei neue D-A-Copolymere, basierend auf TPA als Donoreinheit, synthetisiert. Cyclovoltammetrie-, UV-vis-, Fluoreszenz- und SCLC-Messungen ergaben, dass die beiden D-A-Copolymere einen unterschiedlichen Anteil an Ladungstransfercharakter und Delokalisierung besitzen. Daher variieren auch die Ladungstransportmobilitäten. Wir konnten zeigen, dass die starke Lokalisierung des Exzitons im D-A-Copolymer mit Akzeptor in der Seitenkette zusammen mit der verringerten Konjugation des Systems die Ladungsseparation mit C_{60} hindert. Allerdings führen der schwächere Ladungstransfercharakter und die starke Konjugation/Delokalisierung im D-A-Hauptkettencopolymer zu einer verbesserten Ladungsseparation in Zweischichtsolarzellen.

Introduction

1.1 Organic/hybrid photovoltaics - Motivation

In 2014, the first organic photovoltaic (OPV) test park was settled in Denmark.^[1] A platform with a capacity of 1000 m² with four tilted rows was installed at the technical university of Denmark's Department and Energy Conversion campus. The energy payback time of this prototype park, which is the time a plant has to operate until the amount of energy needed for the setup of the plant has been harvested, is 180 days when located in southern Europe.^[2] In an article about the OPV-based solar park, Frederik Krebs, one of Europe's leading researchers on OPV technology, comments: „Of all known renewable energy technologies the polymer solar cell is the only one that inherently enables fast manufacture of a given energy producing unit with a very thin outline using only abundant elements“.^[2] For the solar panels in this park, the so called bulk heterojunction solar cells composed of poly(3-hexylthiophene) (P3HT) and [6,6]-phenyl C₆₁ butyric acid methyl ester (PC₆₁BM) are applied. On the lab scale such types of solar cells can achieve power conversion efficiencies (PCEs) up to ~ 5 %.



Figure 1. Top left: Semitransparent organic solar cell by Heliatek; top right: Façade of EPFL's SwissTech Convention Center with dye sensitized solar cells from Solaronix; bottom: front row of the solar park at the technical university of Denmark with lanes of stretches of solar cell foil.^[2-4]

Another example of a large area application of organic solar cells is the façade of the École polytechnique fédérale de Lausanne's SwissTech Convention Center. Here, dye sensitized solar cells (DSSCs) were integrated in the building-architecture. Due to the transparency and multicolour of the DSSC devices they are very attractive for applications in architecture and design (see Figure 1).

The great advantage of OPVs is their production on large areas including fast manufacturing rates. A good performance-to-weight ratio and the optimal energy payback time give rise to low cost applications. Furthermore, OPVs can be solution processed making them highly suitable for roll-to-roll fabrication processes on curved and flexible substrates. Most important, the properties of the active materials can be tailored by organic synthesis. This offers numerous possibilities for achieving better performing solar cells.^[5]

On the lab scale high efficiencies up to 9.2 % for single junction polymer solar cells and 10.2 % for polymer tandem cells have been reached.^[6,7] However, the transfer to large area modules is still a challenge. For example, the cells produced by roll-to-roll printing on a large scale for the above mentioned solar park exhibit around 1.53 %. Also, the number of synthetic steps towards the active materials have to be reduced and large amount syntheses need to be optimized.^[8] Nevertheless, OPVs are of great interest for commercial applications. Heliatek holds the world record for opaque organic solar cells with a PCE of 12 % using small molecules. Semitransparent devices already reach a PCE of 7.2 %.^[9] The mentioned efficiencies were gained with different approaches to realize an organic solar cell. In the following chapter the different types of organic solar cells will be presented.

1.2 Types of organic solar cells

The research on organic solar cells started with the bilayer solar cell reported by Tang in 1986.^[10] He used copper phthalocyanine as donor and a perylene tetracarboxylic derivative as acceptor material. In Figure 2a) a schematic illustration of the bilayer setup is shown. The physical processes of such a solar cell involves light absorption, formation of bound electron-hole pairs (excitons), exciton dissociation into free charge carriers, and transport of the holes and electrons to the corresponding electrodes. In more detail, the excitons migrate/diffuse until they reach the interface of donor and acceptor material. Here, if the necessary driving force to separate the excitons into free charges is given, the charge carrier separation occurs. Afterwards, these free charge carriers can be transported to the electrodes. The electrons move through the acceptor and the holes through the donor material. The limiting factor for the overall performance in bilayer cells is the fast recombination of the excitons due to their short diffusion lengths ($\sim 10\text{-}15\text{ nm}$).^[11,12] But, reducing the layer thickness does not help for better efficiencies because approximately $> 200\text{ nm}$ layer thicknesses are required for sufficient light absorption. Therefore, nowadays such simple bilayer solar cells are usually used for fundamental studies on exciton diffusion and charge transport only. However, a thin bilayer device can be optimized in a p-i-n structure, if all separated charges are extracted out using doped injection layers.^[13] The dilemma between exciton diffusion length and layer thickness can be overcome by blending the donor and acceptor material resulting in a bulk-heterojunction solar cell (see Figure 2b)).^[14] Here, the mixture of the materials creates a large interface area, where the excitons can be separated. Furthermore, nanostructured conduction pathways through the materials (percolations ways) guarantee the proper operation of the solar cell even for thicker active layers. Thus, the current produced in the solar cell can be adjusted by the absorption of the active layer through thickness variation.^[15]

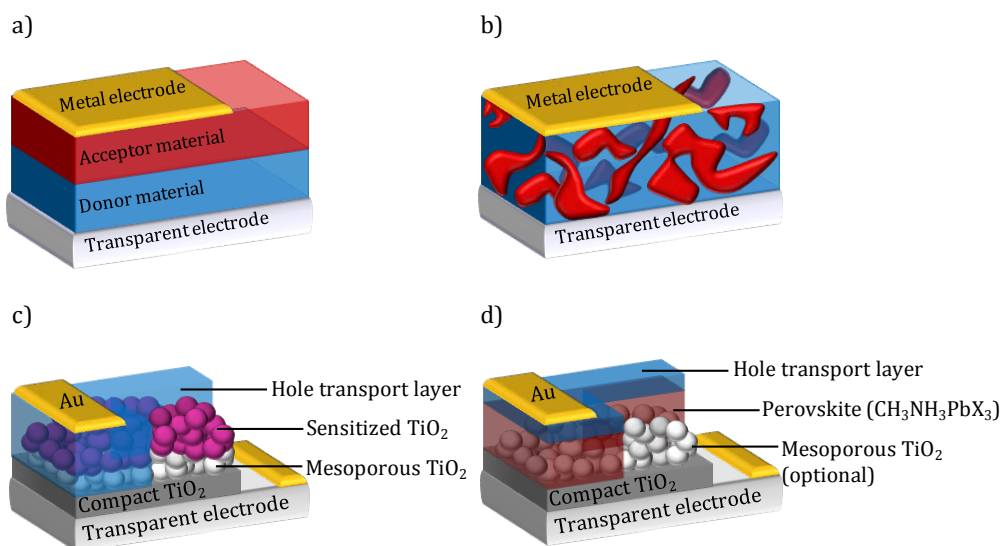


Figure 2. Schematic illustration of a) bilayer solar cell, b) bulk heterojunction solar cell, c) dye-sensitized solar cell, and d) perovskite solar cell.

Another approach towards highly efficient organic solar cells is the dye-sensitized solar cell (DSSC). It was firstly reported in 1991 by O'Regan and Grätzel.^[16] The principle of the DSSC is based on a broad band inorganic semiconductor scaffold, e. g. TiO_2 , which is sensitized, i. e. the surface is chemisorbed with a strongly absorbing dye. The pores of the scaffold are filled with a hole conducting material. This hole conductor can be either liquid (Grätzel cell) or solid (solid state DSSC). High efficiencies up to 12 % were reached with the Grätzel cell, however the long time stability due to the use of the liquid electrolyte is limited.^[17] This can be overcome by the use of solid state hole conductors.^[18] But, up to now the record efficiency is still lower (7.2 %) compared to the DSSCs with liquid electrolytes.

An emerging new and extremely successful concept in the field of solution processed photovoltaics is the perovskite solar cell.

Perovskite solar cells

Generally, the perovskite crystal structure was discovered for calcium titanate which crystallizes in a cubic ABX_3 type. The same crystal structure was found for the inorganic-organic hybrid semiconductors with the composition $\text{CH}_3\text{NH}_3\text{PbX}_3$ ($\text{X} = \text{Cl}, \text{Br}, \text{I}$), which recently had a breakthrough in solar cell research. The first report on the incorporation of perovskites into a solar cell as absorber was by Miyasaka in 2009 who reported an efficiency of 3.8 % using liquid electrolytes in DSSCs.^[19] Up to now, the small area perovskite solar cells (LHPSCs) have reached a record certified value of 17.9 % published in the "National Renewable Energy Laboratory"

(NREL) tables.^[20] This extraordinary development has never happened so fast for other solar technologies. The perovskites exhibit ambipolar transport, high conductivity, and high absorption of light in the visible wavelength region.^[21] To date, the perovskite analogues $\text{CH}_3\text{NH}_3\text{PbI}_3$ and $\text{CH}_3\text{NH}_3\text{PbI}_{3-x}\text{Cl}_x$ are the most prominently used systems in highly efficient devices. In a $\text{CH}_3\text{NH}_3\text{PbI}_3$ perovskite crystal, the Pb^{2+} coordinates to six I^- anions forming PbI_6 -octahedra. These octahedra are connected at their corners to build up a framework of Pb^{2+} and I^- . The CH_3NH_3^+ cation is located at the centre of PbI_6 -octahedra (see Figure 3). The resulting cubic crystal structure was first found by Weber at high temperatures.^[22] However, the structure is heavily disordered with high atomic displacement parameters especially for the anions. This was shown by single crystal X-ray diffraction of $\text{CH}_3\text{NH}_3\text{PbX}_3$ ($X = \text{Cl}, \text{Br}, \text{I}$). Furthermore, in these disordered materials phase changes appear as the temperature increases. At 327.4 K a tetragonal structure forms, while at 162.2 K the structure rearranges to an orthorhombic phase. When we consider the organic cations, their size has to match the space that is formed by eight adjacent octahedra connected through the halide corners. The size of the organic ammonium cation strongly influences the band gap of the semiconductor. For instance, methylammonium, formamidinium, and tetramethylammonium are suitable cations for the formation of a 3D-network.^[23] However, ethylammonium is already large enough to force the system into a 2D structure.^[24] There are also attempts to replace the Pb-cation. One possibility are Sn-perovskite compounds of the type $\text{CH}_3\text{NH}_3\text{SnI}_3$ with high electron and hole mobilities of $2000 \text{ cm}^2 \text{ V}^{-1} \text{ s}^{-1}$ and $300 \text{ cm}^2 \text{ V}^{-1} \text{ s}^{-1}$. Due to their facile oxidizability, these compounds behave as p-type semiconductors with metal-like conductivities.^[25] Recently, Noel et. al were able to prepare solar cells based on $\text{CH}_3\text{NH}_3\text{SnI}_3$ with an efficiency of 6.4 %.^[26]

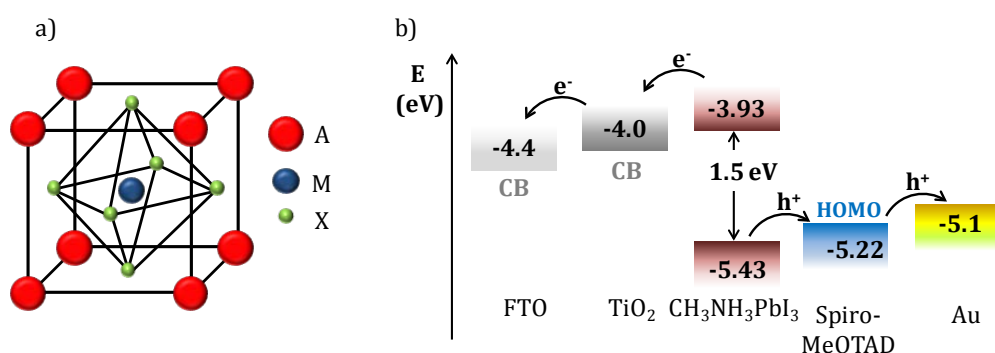


Figure 3. a) Schematic representation of the perovskite crystal structure (AMX_3). $A = \text{CH}_3\text{NH}_3^+$, $M = \text{Pb}$, $X = \text{I}, \text{Cl}$, etc. b) Schematic energy diagram of a perovskite solar cell using TiO_2 as electron conductor and spiro-MeOTAD as hole conductor. Adapted from^[27,28]

In principle, perovskite devices can be prepared in two different architectures. First, the active perovskite layer is placed on top of either a nanostructured metal oxide, such as TiO_2 , ZnO or ZrO_2 , or an Al_2O_3 scaffold (confer Figure 2d)). Second, only a planar electron conducting layer, e. g. ZnO or TiO_2 , is used without a nanostructuring of the metal oxide. Since the transport rate is similar in devices with and without nanostructured TiO_2 , the general working principle of perovskites was found to be dominated by the perovskite material itself.^[27] A strong difference exists between $\text{CH}_3\text{NH}_3\text{PbI}_3$ and mixed halide $\text{CH}_3\text{NH}_3\text{PbI}_{3-x}\text{Cl}_x$ compounds. The incorporation of Cl-ions does not change the band gap, however the diffusion length of charge carriers increases from 130 nm for $\text{CH}_3\text{NH}_3\text{PbI}_3$ to > 1000 nm for $\text{CH}_3\text{NH}_3\text{PbI}_{3-x}\text{Cl}_x$.^[29,30] This is supposed to be the reason why $\text{CH}_3\text{NH}_3\text{PbI}_3$ cells work efficiently with a mesoporous layer that can drain electrons, and $\text{CH}_3\text{NH}_3\text{PbI}_{3-x}\text{Cl}_x$ can also be used in planar setups or with an insulating Al_2O_3 layer.^[31] Using the mixed halide $\text{CH}_3\text{NH}_3\text{PbI}_{3-x}\text{Cl}_x$, highly efficient charge generation and collection can be achieved without nano- or mesostructures. This was shown for the first time by Liu et al. in a fully solution processed solar cell with a record PCE of 15.4 %.^[32] Nevertheless, a complete surface coverage is more difficult to achieve for planar devices compared to the mesoporous devices, which is still a drawback of the planar cell especially in case of reproducibility. The optimal surface coverage and careful optimization of the electron conducting oxide layer are the most important factors to reach high efficiencies. For example, planar devices with ZnO and $\text{CH}_3\text{NH}_3\text{PbI}_3$ reached a record efficiency up to 15.7 %.^[33] The record efficiencies have to be treated with caution, since a scattering of data and strong deviations of the performances using different architectures in various laboratories are reported in the literature.

In this thesis, the following concept was used for the preparation of perovskite solar cells. It is a straight forward processing technique presented by Burschka et al. who demonstrated a very good performing cell with 15 % PCE.^[34] Here, a mesoporous TiO_2 layer adapted from the DSSC concept is used. The $\text{CH}_3\text{NH}_3\text{PbI}_3$ perovskite was formed by a sequential dipping technique. First, PbI_2 was spin-coated on top of the mesoporous TiO_2 . Then, the substrate was dipped into a solution of $\text{CH}_3\text{NH}_3\text{I}$ to form the perovskite crystals. This crystallization process in film can also be realized using $\text{CH}_3\text{NH}_3\text{I}$ vapour.^[35] The role of the mesoporous TiO_2 is still under discussion.^[31] In order to understand the characterization methods applied in organic solar cells, the following chapter gives an overview.

1.3 Characterization of organic solar cells

Usually, organic solar cells are analyzed by two important characterization methods: the measurement of the current density-voltage (J - V)-characteristics and the external quantum efficiency (EQE). A J - V -curve is typically recorded in dark and under illumination of the device. Under dark conditions, no current flows until the injection barrier at a certain threshold voltage is reached. Then, a current starts flowing in forward bias. The threshold voltage is similar to the photovoltage under illumination, when the cell produces a photocurrent in the fourth quadrant. Figure 4a) illustrates a typical J - V -curve under illumination and in dark. For the measurement in light, typically a solar simulator is used which produces a solar-like irradiation spectrum. This spectrum is equivalent to the air mass 1.5 solar spectrum (AM 1.5) and the light intensity is normally set to “1 sun”, corresponding to 1000 W m^{-2} . The resulting photovoltaic parameters derived from the J - V -characteristics are the short circuit current density J_{sc} , the open circuit voltage V_{oc} , the fill factor (FF), and the PCE.

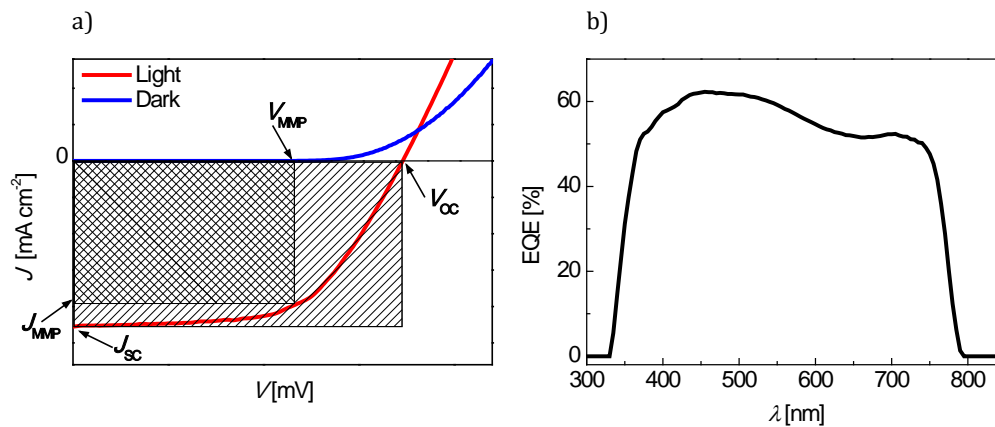


Figure 4. a) Examples of a J - V -characteristic of an organic solar cell under illumination and in dark. The Intersections with the abscissa and the ordinate give the parameters V_{oc} and J_{sc} . The maximum power point (MPP) represents the point where the product of voltage and current density is maximal. b) External quantum efficiency (EQE) spectrum of a solar cell.

The quotient of the maximum power P_{max} and the incident power P_{in} gives the PCE of the cell as shown in equation (1).

$$PCE = \frac{P_m}{P_{in}} = \frac{J_{sc} \cdot V_{oc} \cdot FF}{P_{in}} \cdot 100\% \quad \text{Equation (1)}$$

As depicted in Figure 4a), the J_{SC} and the V_{OC} determine the power production of the solar cell. However, the maximum power density produced (P_{max}) occurs at the maximum voltage (V_{max}) and the maximum current density (J_{max}). Due to the resistance and recombination losses as well as the diode behavior, the V_{max} is always lower than the V_{OC} ; the same applies for J_{SC} . The difference is described by the FF (equation (2)).

$$FF = \frac{P_m}{J_{SC} \cdot V_{OC}} \quad \text{Equation (2)}$$

In order to analyze the J - V -characteristic in more detail, the series resistance (R_S) and the shunt resistance (R_{SH}) can be calculated by taking the inverse of the slopes near to the J_{SC} and V_{OC} . A low R_S and a very high R_{SH} are desirable for a perfect working solar cell with high FF. The R_S strongly influences the FF.

The EQE, or incident photon to current efficiency (IPCE), is defined as the ratio of the number of incident photons to the number of generated charge carriers at a specific wavelength λ (equation 3), where h is the Plank's constant, c the speed of light, q the elementary charge, $J_{SC}(\lambda)$ the short circuit current density at the wavelength λ and $P(\lambda)$ the monochromatic incident optical power.

$$EQE = \frac{h \cdot c}{q} \cdot \frac{J_{SC}(\lambda)}{P(\lambda)\lambda} \quad \text{Equation (3)}$$

In OPVs the EQE value is determined by the absorption behavior of the used active materials. Hereafter, an overview over organic semiconducting polymers used in OPV is given to understand the crucial influence of the materials on the device performance and photogeneration induced charge generation processes.

1.4 Organic semiconducting polymers

The semiconducting properties of conjugated polymers arise from their π -electrons which delocalize over the monomer units via alternating single and double C-C bonds resulting in an extended π -system. This is possible, because p_z orbitals carrying electrons are left over from the sp^2 hybridization of the carbon atoms in the double bonds. Due to the delocalization to other π -bonds in the neighborhood, the mobility of charge carriers is possible. Another important prerequisite for optoelectronic applications is the solubility of the materials. Only soluble materials can be utilized in straight-forward processing techniques such as printing on a large scale. Organic semiconducting polymers are classified into hole and electron conducting polymers. For both types, homopolymers or copolymers are known in the literature. The unique feature of organic semiconducting polymers is the tunability of their electronic and optical properties by structural changes using smart synthetic approaches. Especially the variation of the electronic location of highest occupied molecular orbital (HOMO) and lowest unoccupied molecular orbital (LUMO) levels and the optical gap (E_{opt}) is an important research field. For the use of semiconducting polymers in OPVs, a low E_{opt} is desirable to realize strong absorption over a broad wavelength range. Therefore, the donor-acceptor (D-A) strategy was developed.

Donor-acceptor concept

The concept of achieving lower optical gaps in conjugated polymers via the D-A strategy (also known as low band gap strategy) was applied successfully over the last 10 years.^[36,37] Generally, five energetic contributions determine the E_{opt} of polyaromatic conjugated systems: the energy appendant to the bond length alternation, the planarity, the aromatic resonance energy of the cycle, the inductive or mesomeric electronic effects of the substitution, and the intermolecular or intramolecular coupling.^[38] De facto, the enlargement of the π -system, the stabilization of the quinoidal form, and the use of electron-pulling and pushing units lead to a reduction of the E_{opt} . A schematic picture of the fundamental energy of quinoidal vs. aromatic form and the orbital interaction between donor and acceptor units are illustrated in Figure 5. As depicted below, a low E_{opt} results from the orbital interaction overlap of the HOMO/LUMO. Thus, the energy levels have to be close to each other. Usually, strong electron donating groups are used as the donor part and strong electron deficient units for the acceptor part.

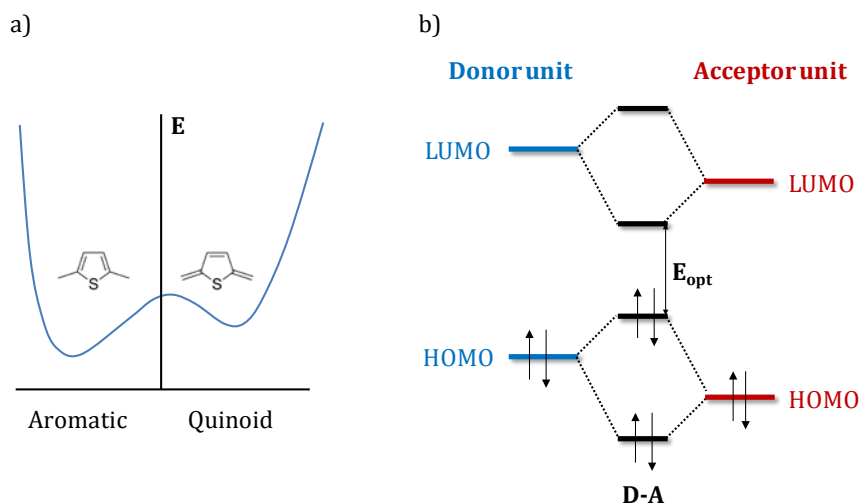


Figure 5. Schematic illustration of a) energetic comparison of the aromatic and quinoid structure of a thiophene subunit and b) Interaction between donor and acceptor unit which leads to a lowered optical gap E_{opt} . Reproduced from^[39,40]

The modern polymer chemistry allows the design of a variety of homo- and copolymers. Thus, many different synthetic approaches towards semiconducting polymers are used in the literature. In the following, the most frequently applied methods are presented. In this theses Suzuki and Yamamoto polycondensation were the methods of choice for the synthesis of the semiconducting polymers and copolymers

Polymerization methods

The common feature in the structure of the above mentioned semiconducting polymers is their polyarylene backbone. In order to obtain aryl-aryl C-C coupling, so called cross-coupling techniques were developed in the 1970's. For example, poly(phenylene)s were synthesized by Yamamoto.^[41] He used the Kumada cross-coupling for the polycondensation, which was just discovered four years before.^[42] The Kumada cross-coupling has reached a high level of development, e. g. living polymerizations with full endgroup control and the possibility to synthesize block copolymers were presented for P3HT.^[43,44] The living Kumada chain-transfer polymerization was also applied for the polymerization of other monomers such as fluorenes or carbazoles.^[45]

Another important and well developed polymerization method for the synthesis of semiconducting polymers is the Suzuki polycondensation. The coupling reaction towards low molecular weight compounds itself was developed by Suzuki.^[46] As depicted in Figure 6, the first step of the reaction mechanism is the oxidative addition of the aryl-halide to the Pd(0)-complex.

This is the rate-determining step. The higher the reactivity and the weaker the aryl-halide bond, the faster the rate-determining step. The relative reactivity of the halides decreases in the order of $I > Br \gg Cl$. In the next step the transmetalation takes place after which the reductive elimination results in the aryl-aryl C-C bond leading to the coupled product.

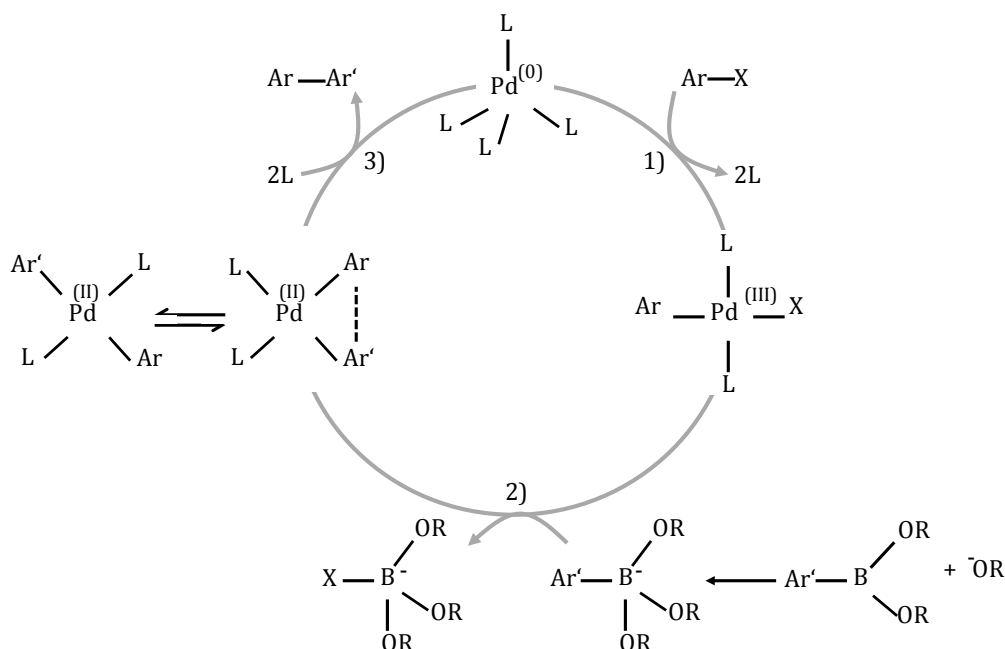


Figure 6. Illustration of the catalytic cycle of a Suzuki coupling reaction involving the steps oxidative addition (1), transmetalation (2), and reductive elimination (3). Adapted from^[46].

The first synthesis of poly(*para*-phenylene) via Pd-catalyzed coupling was shown in 1989.^[47] To date, Suzuki polycondensation is among the widely used methods to synthesize conjugated polymers.^[48] The polycondensation occurs via a step-growth mechanism using either AA/BB or the AB type monomers. In the AA/BB type, two monomers are used for the polymerization, usually one carrying two halide groups and the other one carrying two boronic acid derivatives. The AB approach uses one single monomer holding both functional groups necessary for the reaction. Figure 7 shows a schematic picture of the two described Suzuki approaches.

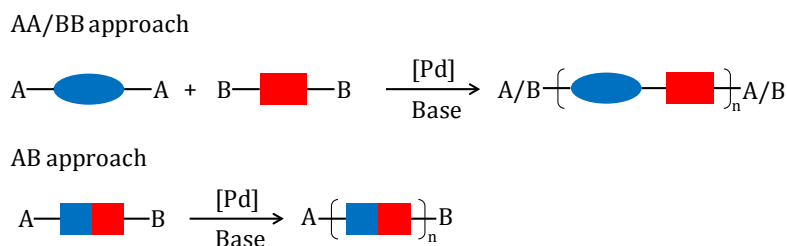


Figure 7. Schematic illustration of the AA/BB and AB approach for Suzuki polycondensation. A: Halide, B: boronic acid derivative. In AA/BB type all possible end groups are present, whereas in AB-type condensations, the possibilities are limited. Adapted from^[48]

The AA/BB type approach is advantageous for the synthesis of alternating copolymers. Subsequently, it is mainly applied for the preparation of D-A polymers. In contrast, the AB approach requires the synthesis of an asymmetrically substituted monomer. This can be challenging when alternating copolymer structures, e. g. for D-A copolymers, are desired.^[49] However, the AB approach enables a Suzuki living chain-growth polymerization which offers new routes for end group functionalization towards block copolymers.^[50,51]

Another prominent polymerization method, mostly established for the synthesis of D-A polymers, is the Stille-polycondensation. In Stille coupling reactions, stannanes instead of boronic acid derivatives are coupled with aryl halides, triflates, or acyl chlorides in a Pd-catalyzed cross-coupling reaction.^[52,53] Similar to the Suzuki-polycondensation, the Stille-reaction can be utilized to prepare semiconducting polymers via aryl-aryl coupling in an AA/BB approach.^[54] Advantageous are the mild reaction conditions and the tolerance of many functional groups. Additionally, higher molecular weight polymers were usually obtained by this method. Hence, a variety of monomers were polymerized via Stille-coupling.^[55] For the sake of completeness, the coupling methods Sonogashira (alkin-halide coupling) and Heck (vinyl-halide coupling) should be mentioned as further polycondensation methods for the synthesis of conjugated semiconducting polymers.^[56,57]

Contrary to the above mentioned cross-coupling reactions which require bifunctional groups, the Yamamoto reaction can be carried out with monofunctional organohalides using zerovalent nickel complexes.^[58] It was shown that linear polymers or cycles of poly(*N*-(2-ethylhexyl)carbazol-3,6-diyl) can be synthesized by Yamamoto polycondensation efficiently.^[59] Generally, a bis(cyclooctadiene)nickel(0) (Ni(COD)₂) catalyst is used in combination with a 2,2'-bipyridyl (bpy) coligand. Figure 8 gives the catalytic cycle of the Yamamoto cross coupling as proposed by the group around Yamamoto. The reaction mechanism starts with a ligand exchange (COD vs. bpy) followed by the oxidative addition of the aryl halide (e. g. ArBr) to the (bpy)Ni(COD)-complex leading to (bpy)Ni(Br)(Ar). This complex undergoes a

disproportionation to $(\text{bpy})\text{Ni}(\text{Br}_2)$ and $(\text{bpy})\text{Ni}(\text{Ar}_2)$. After reductive elimination the coupled aryl-aryl compound is formed. A disadvantage of the Yamamoto-coupling is the need of a stoichiometric amount of the Ni(0) catalyst.^[60]

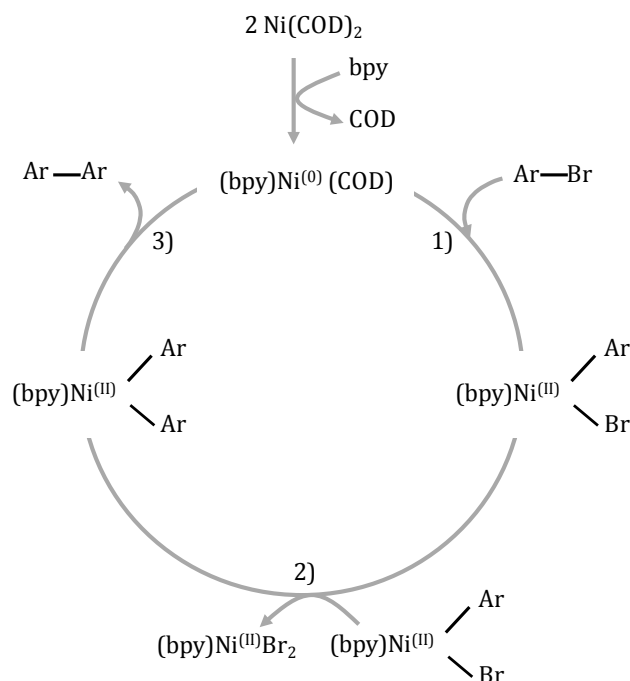


Figure 8. Schematic catalytic cycle of a Yamamoto cross coupling reaction starting from the precatalyst $\text{Ni}(\text{COD})_2$ involving the steps oxidative addition (1), transmetalation (2), and reductive elimination (3).^[60]

The above mentioned synthetic approaches are frequently used in the synthesis of organic semiconducting polymers. Since this thesis is dealing with the design of hole transporting polymers, the next part will give an overview of typical polymers reported in the literature followed by a short part about electron transporting polymers.

Hole transporting materials

All materials presented in the following have in common that their hole transporting nature is based on the strong electron donating ability of the conjugated systems. The overview over the hole transport materials (HTMs) given below represents an excerpt of the known materials to date. Two recent reviews by Cheng and Zhang can be consulted for more detailed information.^[61,62] Figure 9 gives a choice of homopolymers and D-A copolymers.

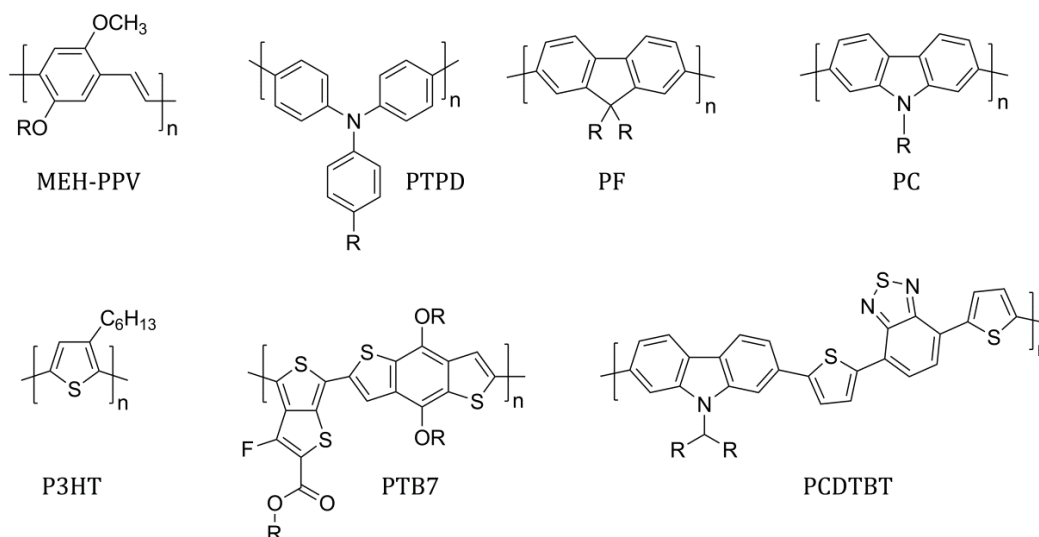


Figure 9. Examples for hole transport materials used in OPVs. Top: Homopolymers with large optical gap. Down: P3HT and D-A copolymers with low optical gap.

The most prominent example of a HTM for the use in OPVs is P3HT. It possesses excellent optical and electrical properties in combination with high thermal and chemical stability. An important step towards the structural control of P3HT was found by McCullough.^[63] He demonstrated a polymerization method where highly regioregular P3HT is produced. The regioregularity as well as the molecular weight are essential for the packing of P3HT and consequently the hole transport properties.^[64,65] Among the numerous synthetic routes towards P3HT and its derivatives, the living chain growth polymerization via Kumada coupling is well understood and applied e. g. for the preparation of well-defined block copolymers.^[43] Since the HOMO and LUMO values fit properly to the commonly used PC₆₁BM, a lot of research effort has been put in the investigation of OPVs using the P3HT/PC₆₁BM system.

In the beginning of the era of OPVs, poly(*p*-phenylenevinylene) (PPV) and poly[2-methoxy-5-(2-ethylhexyloxy)-1,4-phenylenevinylene] (MEH-PPV) were studied intensively. The synthesis can be carried out via the Gilch-Route.^[66] Initial bilayer solar cells were prepared in combination with PC₆₁BM by Inganäs.^[67] Later, bulk heterojunction solar cells were shown and e. g. thiophene was used as a comonomer to reach higher efficiencies.^[68,69]

Another family of materials with strong electron-donating nature are poly(triarylamine)s. They stand out due to their excellent hole transport mobilities and good electrochemical stability. The corresponding monomer triphenylamine (TPA) is used in commercial xerographic applications because of its excellent physical, photochemical and electrochemical properties of this hole conductor.^[70] Within the functional TPA moiety, the nitrogen center can be easily oxidized resulting in effective transport of positive charge carriers via a radical cation species. The

unsubstituted TPA can undergo dimerization to tetraphenylbenzidine (also triphenyldiamine, TPD).^[71] Low molecular weight TPDs showed high hole transport mobilities up to $10^{-2} \text{ cm}^2 \text{ V}^{-1} \text{ s}^{-1}$.^[72] The TPA or TPD units can be incorporated either in the main chain or in the side chain of a polymer with a non-conducting backbone, e. g. poly(styrene). These polymeric analogues are used as HTMs in OLEDs or OPVs.^[73] In order to realize the solubility of TPA main chain polymers either methyl groups, alkyl or alkoxy chains have to be attached. One commercially available TPA main chain polymer, poly[bis(4-phenyl)(2,4,6-trimethylphenyl)amine], is soluble due to the three methyl groups that lead to a twist of the polymer backbone and reduced interaction between the chains. The synthesis is carried out via AB-type Suzuki polycondensation. This polymer showed a high hole transport mobility of $6 \cdot 10^{-3} \text{ cm}^2 \text{ V}^{-1} \text{ s}^{-1}$ in organic field effect transistors (OFETs) and was e. g. used in air-stable OFETs.^[74,75] In the case of alkoxy side chains, it was shown by Sim et al. that the polymer containing alkoxy substituents is more easily oxidized resulting in a change of the optical and hole transport properties.^[76] The polymerization method used in this study was FeCl_3 -catalyzed oxidative coupling.^[77] Suzuki coupling was also used to synthesize polyelectrolytes with a TPD backbone, or polymers with an additional phenyl spacer.^[78,79] Another suitable approach towards TPA main chain polymers is the application of the Buchwald-Hartwig reaction as polymerization technique.^[80,81] In the literature, also TPA containing polymers without direct aryl-aryl coupling leading to less conjugated systems are demonstrated. These polymers are connected for example by small alkyl spacers or ether linkages.^[82-84]

Besides, the styryl-type TPA/TPD side chain polymers should be mentioned. The synthesis of such polymers can be realized by controlled polymerization such as the nitroxide mediated radical polymerization (NMRP) or anionic polymerization.^[85,86] But all these TPA-containing main-chain or side-chain polymers have only a limited absorption in the visible range with E_{opt} around 3.5 eV.^[87]

Another well-known HTM which was first used in OLEDs are poly(fluorene)s (PFs). Their rigid and planar backbone, the high hole transport mobility, and the low lying HOMO are promising properties for the use in OPVs as well. In order to synthesize PF, the straight-forward Suzuki polycondensation can be used.^[88] However, the drawback of PFs is the large E_{opt} of 3.0 eV. Approaches towards the reduction of the E_{opt} will be given later on.

The substitution of the carbon atom in fluorene with nitrogen leads to another prominent monomer for conjugated polymers, the carbazole. Poly(2,7-carbazole)s were used as homopolymers in bulk heterojunction solar cells but only moderate efficiencies were reached because of the high E_{opt} similar to PFs.^[89] Furthermore, the fusion of two carbazoles gives another monomer, the indolo[3,2-*b*]carbazole. A corresponding homopolymer showed a very

high hole mobility in OFETs. This is due to the large coplanar π -system.^[90,91] Other fused monomers such as isothianaphthene, cyclopenta[2,1-*b*:3,4-*b'*]dithiophene, silafluorene, dithieno[3,2-*b*:2',3'-*d*]silole, dithieno[3,2-*b*:2',3'-*d*]pyrrole, benzo[1,2-*b*:4,5-*b'*]dithiophene, thieno[3,4-*b*]thiophene, and thieno[3,2-*b*]thiophene are applicable as HTMs.^[92-98]

All the homopolymers reviewed above, except for P3HT, possess a large E_{opt} which is unfavorable for their use in OPVs. A breakthrough was gained by the introduction of the D-A strategy which was explained above (confer Figure 5). In the following a few examples for highly efficient D-A-materials are given. The successful use of D-A polymers for photovoltaic applications has caused a tremendous interest in this class of materials.^[99] Commercial products such as copolymers with 2,7-carbazole, 9,9-dioctylfluorene or benzodithiophene were developed in between (see PTB7 and PCDTBT in Figure 9). Especially these three monomers have attracted attention for OPV applications.^[100-102]

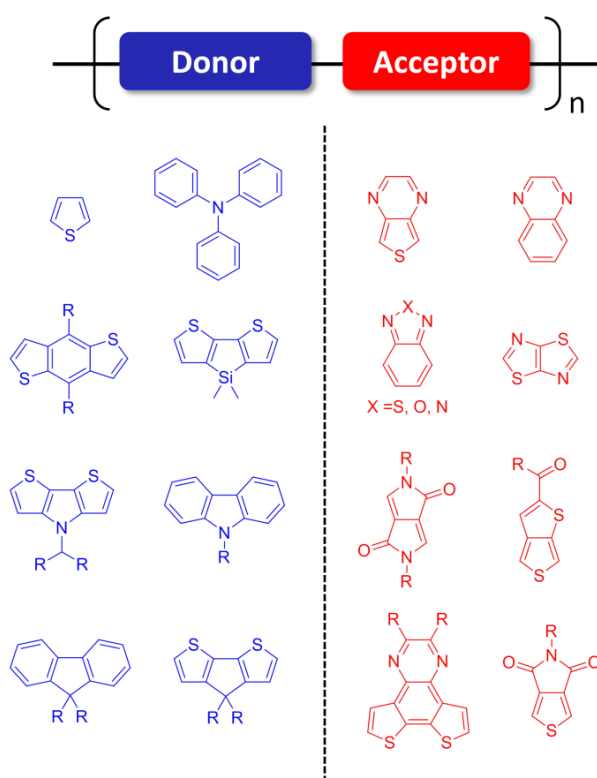


Figure 10. Summary of selected donor and acceptor units for the synthesis of D-A-copolymers to achieve low optical gaps. Adapted from^[99].

Furthermore, D-A copolymers were also efficiently used in OFETs. For example, the copolymer poly[4-(4,4-dihexadecyl-4*H*-cyclopenta[1,2-*b*:5,4-*b'*]dithiophen-2-yl)-*alt* -[1,2,5]thiadiazolo[3,4-*c*]pyridine] (PCDTPT) showed a very high hole transport mobility of $23.7 \text{ cm}^2 \text{ V}^{-1} \text{ s}^{-1}$.^[103] A class of very efficient D-A-copolymers are based on diketopyrrolopyrrole (DPP) and have provided

PCEs of $\sim 8\%$ in OPV cells.^[104] Furthermore, through clever combination of D-A units a very high V_{oc} up to 1.1 V could be reached in D-A copolymers.^[105] Figure 10 gives an overview over typical D- and A-moieties for the synthesis of D-A-polymers.

The TPA-unit as donor for D-A-copolymers was successfully used in combination with benzothiadiazole as acceptor.^[106] An enhancement of the optical absorption was achieved and a PCE of 2.8 % was found for devices in combination with PC₆₁BM^[106] Different other copolymers using comonomers such as thiophene, 3,4-ethylenedioxythiophene, carbazole and fluorene were also used to tailor the optical and electrochemical properties of TPA-containing copolymers.^[107-109]

A new D-A strategy that benefits from a different arrangement of D and A units was effectively applied in OPVs with TPA as donor unit. Here, the polymer backbone is composed of electron rich units whereas the acceptor moiety is located in the side chain of the polymer either directly coupled or separated by a π -bridge. The concept was first shown by Huang.^[110] Copolymers comprised of TPA and fluorene or TPA and carbazole were used.^[37,111] Due to the improvement of the absorption behavior and a high hole transport mobility a PCE of 4.74 % was achieved with [6,6]-phenyl-C₇₁-butyric acid methyl ester (PC₇₁BM).^[112] In Figure 11 some examples for TPA copolymers using these two different D-A approaches are shown.

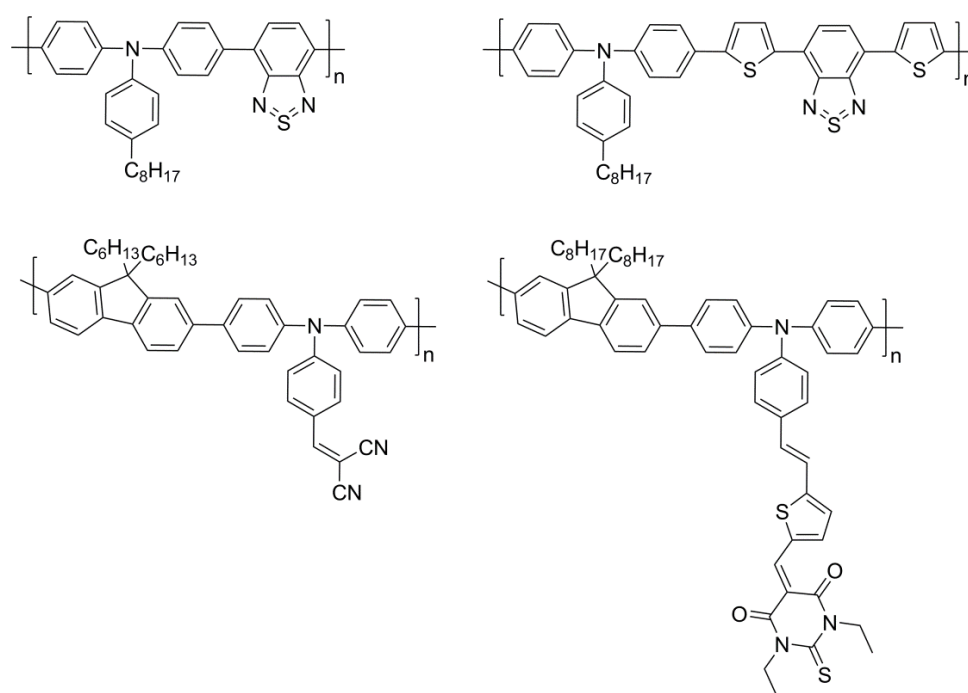


Figure 11. D-A-copolymers with TPA as donor unit. Top: classical D-A-strategy, bottom: D-A-strategy with the acceptor moiety in the side chain of the copolymer.

Electron transporting materials

Similar to the HTMs presented above, electron transporting materials (ETMs), should provide good transport and light harvesting properties as well as stability under the processing and operational conditions. Generally, electron transporting materials are electron deficient and possess a low lying LUMO level. Therefore, they can be easily reduced to radical anions. The majority of ETMs are low molecular weight compounds. However, there are some examples of well operating polymeric ETMs (see Figure 12).

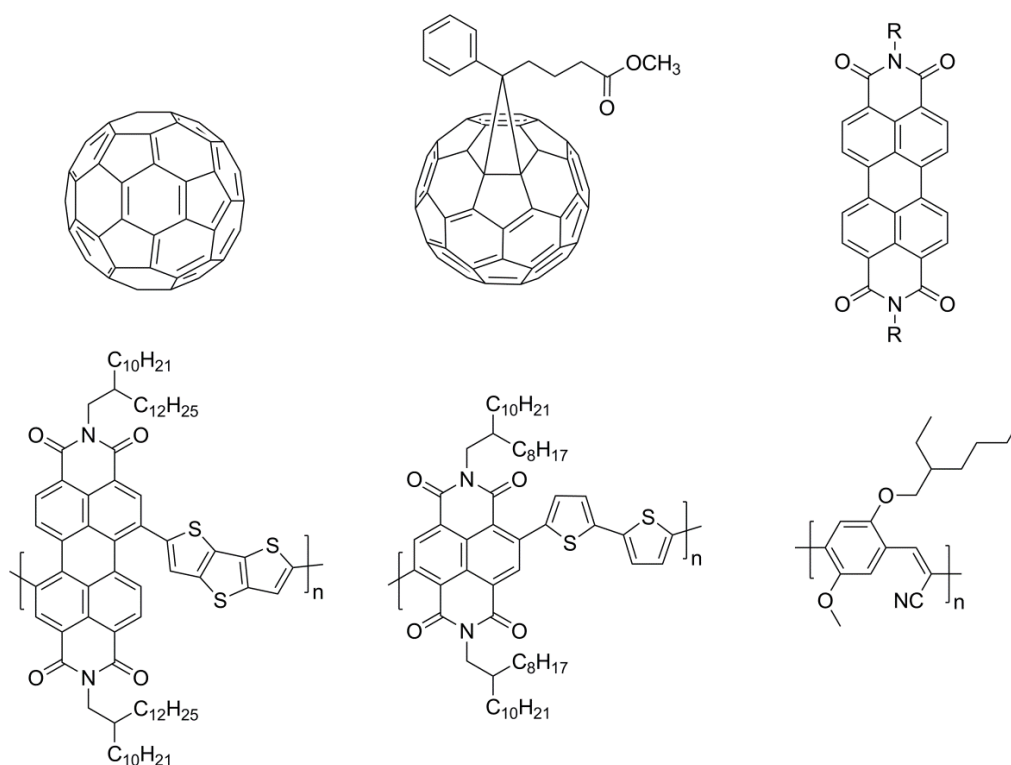


Figure 12. Examples for small molecule and polymeric ETMs. Top: C₆₀, PC₆₁BM, perylene bisimide; down: perylene bisimide and naphthalene bisimide based copolymers, poly[2-methoxy-5-(2'-ethylhexyloxy)-1,4-(1-cyanovinylene)phenylene].

The most common ETM used in OPVs is the fullerene derivative PC₆₁BM, which was reported by Hummelen et al. in 1995 for the first time.^[113] It is a soluble C₆₀-derivative, and provides, similar to C₆₀ itself, a high electron mobility.^[114] The disadvantage of PC₆₁BM is the low absorption in the visible wavelength region. An improvement of the absorption was achieved by developing the C₇₀ analogue (PC₇₁BM). Nevertheless, both fullerene derivatives are used in OPVs with suitable HTMs reaching high efficiencies (8-10 %). Other low molecular weight ETMs for the application in OPVs are for example based on perylene bisimide (PBI).^[115] They possess high electron affinity and good electron mobilities in combination with strong absorption in the

visible light. Substitution of the imide functionality with alkyl or ethylene glycol side chains can improve the solubility in common organic solvents. By contrast, the substitution of the core positions leads to changes in the optical and electrochemical properties. Thus, a variety of tailor made molecules have been synthesized for the use as ETMs in OPVs as well as in OFETs.^[116,117]

In the field of polymeric ETMs, good performances in OFETs were found for some of these acceptor materials.^[118-122] Here, also the polymer analogues of the above mentioned perylene bisimides were used.^[123] Among the best performing ETM for OFETs is the alternating copolymer poly{[*N,N'*-bis(2-octyldodecyl)-naphthalene-1,4,5,8-bis(dicarboximide)-2,6-diyl]-*alt*-5,5'-(2,2'-bithiophene)}. A very high electron mobility of 0.45–0.85 cm² V⁻¹ s⁻¹ was reported for this material.^[124] The record electron mobility measured in OFETs to date is 6.3 cm² V⁻¹ s⁻¹ shown by Sun et al.^[125] However, the application for OPVs is still a challenge. For example, a PBI containing copolymer with a low optical gap and high electron mobility of 1.3 · 10⁻² cm² V⁻¹ s⁻¹ in OFETs reached an efficiency of 1.5 % in combination with a bi(thienylenevinylene)-substituted polythiophene.^[126]

A very promising cyano-substituted derivative of MEH-PPV was reported by Friend et al. in 1998, showing a very high peak external quantum efficiency of 28 % at that time. Nevertheless, the PCE in the corresponding solar cells were only modest.^[127,128] In combination with the more suitable poly[3-(4-*n*-octyl)-phenylthiophene] a PCE of 2 % was achieved.^[129] For further reading a recent review reports on polymeric ETMs.^[130]

1.5 Charge transport in organic semiconducting polymers

The charge transport in organic semiconductors is different from the transport in classical inorganic semiconductors. Therefore, other theoretical models have to be applied. The following part summarizes in short a review about charge transport in organic semiconductors where more detailed information can be found.^[131]

When talking about charge transport, the main parameter for its description is the charge carrier mobility. In general, in the absence of an external potential, transport is diffusive and can be expressed by the simple diffusion equation:

$$\langle x^2 \rangle = nDt \quad \text{Equation (4)}$$

where $\langle x^2 \rangle$ is the mean-square displacement of the charges, D the diffusion coefficient, t the time, and n represents an integer number equal to 2, 4, or 6 for one-, two-, and three-dimensional systems. Via the Einstein-Smoluchowski equation the charge mobility μ can be expressed using the diffusion coefficient:

$$\mu = \frac{eD}{k_B T} \quad \text{Equation (5)}$$

where k_B is the Boltzmann constant and e is the electron charge. If an external electric field (F) is applied, a drift of the charge carriers is induced. Thus, the mobility can be described as

$$\mu = \frac{v}{F} \quad \text{Equation (6)}$$

with the velocity of the charges v . The charge transport mechanism in organic materials is predominantly hopping between localized states. Thus, the mobility increases with electric field and charge concentration, and decreases with decreasing temperature. The Poole-Frenkel equation (7) describes the dependence of the mobility on the electric field.

$$\mu = \mu_0 \exp(\beta\sqrt{E}) \quad \text{Equation (7)}$$

Where β stands for material dependent parameters, including the temperature dependence.

Many other factors influence the charge carrier mobility, e. g. molecular packing disorder, presence of impurities, charge carrier density, and molecular weight. However, if no chemical or physical defects are present, the charge transport depends on the electronic and electron-vibration (phonon) interactions. A phonon is a "particle-like quantized mode of vibrational energy arising from the collective oscillations of atoms within a crystal".^[131] The electron-phonon interactions in organic semiconductors are large compared to the electronic

interactions. Thus, electron-phonon coupling leads to the formation of polarons. In the literature, two main models are present for the description of charge transport in organic semiconductors: the polaron model^[132-134] and the disorder model^[135-137].

The polaron model considers the strong electron-phonon interaction in a situation where chemical and physical defects are absent. According to general models, the mobility is the sum of two contributions:^[138-140]

$$\mu = \mu_{tun} + \mu_{hop} \quad \text{Equation (8)}$$

The first contribution arises from electron tunneling (μ_{tun}) and dominates the transport at low temperatures. At higher temperatures the second term (μ_{hop}) is dominant, which is related to the hopping motion. The relative contributions of these mechanisms depend on electron-phonon coupling, electronic and phonon bandwidths, and phonon energy.

The disorder model describes the charge transport in the presence of static disorder. This disorder arises from chemical or structural defects of the polymeric backbone, resulting in kinks or twists. Due to the disordered structure of conjugated polymers, the mobility in those systems is orders of magnitudes lower than for organic crystals. In contrast to standard semiconductor models, where the concept of a band conduction is used, the disorder model assumes that localized states are present in organic semiconductors. The charge carriers have to hop between these localized states. Thus, the charge transport sites are delocalized and can be described by a Gaussian density of states (DOS). The disorder of the system can be quantified by the shape of the DOS. In highly ordered systems the band states delocalize. Due to increasing disorder the band states localize until all states are localized in strong disorder. The charge transport occurs in the hopping regime where the charges can hop between interacting molecules (see Figure 13a)). Bässler and his co-workers developed this hopping transport in a Gaussian DOS for a disordered system.^[135] The DOS can be described as a Gaussian function, where the width σ of the DOS is a measure of the disorder of the transport states. Thus, the charge carrier mobility dependence on the temperature T and the electric field E can be derived by:

$$\mu = \mu_0 \exp \left[- \left(\frac{2\sigma}{3kT} \right)^2 \right] \exp C \left[\left(\frac{\sigma}{kT} \right)^2 - \Sigma^2 \right] \sqrt{E} \quad \text{Equation (9)}$$

where μ is the mobility, μ_0 the mobility at zero field, C an empirical constant, and Σ the quantity which describes the positional disorder. The Gaussian shape originates from the absorption bands in the disordered organic materials and has no direct experimental proof (see Figure 13b)). Within this model the charge carrier mobility is dependent on the temperature (non-Arrhenius) and the electric field. In particular, the field dependence resembles a Poole-Frenkel behavior. The results of simulations done with the standard Gaussian disorder model can only

explain experimental data at high fields. Thus, an extended version of the Gaussian disorder model was introduced.^[141] It includes spatial correlation among hopping sites.

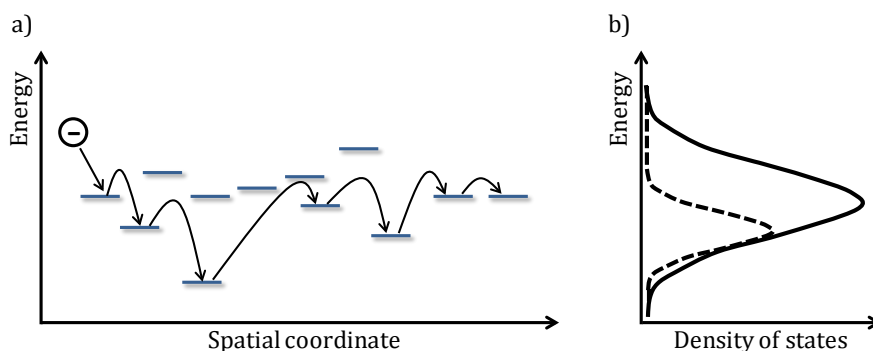


Figure 13. a) Arbitrary pathway of an electron through a molecular ensemble. The horizontal lines represent energy levels of individual molecules. Hopping to lower energy states happens more often since hopping to higher energy states needs an activation energy. b) Schematic picture of the density of states (solid line) and occupied states (dashed line) for a disordered semiconductor. Adapted from^[142]

The charge carrier mobility can be determined by a variety of methods. In the following, some important methods are presented.

Time of flight technique

The time of flight (ToF) technique is a classical method to determine the charge carrier mobility in an organic semiconductor.^[143,144] Figure 14 depicts a typical setup and the corresponding schematic photocurrent transient.

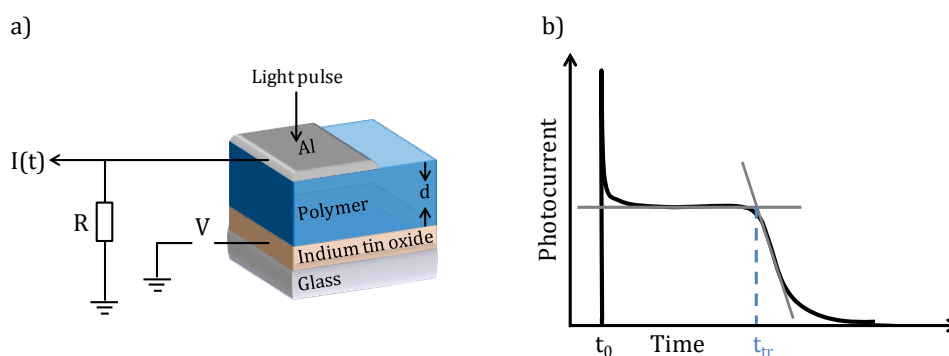


Figure 14. a) Schematic TOF setup and b) schematic representation of a photocurrent transient. Adapted from^[144]

For the experiment, the sample is sandwiched between two electrodes. A short laser pulse generates a spatially narrow sheet of charge carriers at one electrode. The applied electric field pushes the charges and the mean arrival time (t_{tr}) at the exit contact is recorded. Together with the sample thickness d , the electric field F and the mobility μ the following relation can be used:

$$t_{tr} = \frac{\mu}{dF} \quad \text{Equation (10)}$$

For the observation of an ideal ToF signal several requirements have to be fulfilled. Before photoexcitation the sample has to be free of charges, the thickness of the sheet of charge carriers should be small in comparison to the film thickness, and the charges cannot interact due to their low concentration. Furthermore, the mobility should be time independent. Therefore, no deep trapping should be present because they would lead to a time dependent mobility. Thus, to meet the above criteria the sample thickness for the ToF measurement is kept high (in the range of μm).

Space charge limited current

Space charge limited current (SCLC) measurements are based on a diode setup where the organic semiconductor is placed between two electrodes. Those devices are called single carrier devices including the differentiation of hole-only or electron-only devices. The current-voltage curve is determined by the mobility and concentration of charge carriers and the electric field. The choice of the electrodes is crucial since exclusively Ohmic injection from one electrode and charge collection from the other electrode has to be ensured. In hole-only devices the charge injection into the HOMO of the semiconductor should take place and charge transport occurs through the HOMO states only. For electron-only devices electrons are to be injected into the LUMO and are transported through the LUMO states. Experimentally, for hole-only devices often poly(3,4-ethylenedioxythiophene):poly(styrene-sulfonate) (PEDOT:PSS) or MoO_3 coated indium tin oxide (ITO) in combination with gold as extraction electrode is used. Figure 15 shows a typical setup of a hole-only device. In the case of electron-only devices mainly zinc oxide coated ITO and calcium fluoride application as electrode configurations. The selection of electrodes depends on the HOMO/LUMO values of the material in general.

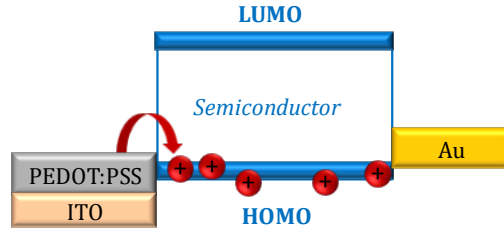


Figure 15. Schematic illustration of a hole-only device with PEDOT:PSS and gold as electrodes. The holes are injected by the PEDOT:PSS electrode and migrate to the Au electrode only through the HOMO states.

If the cathode and the anode are Ohmic contacts, which means that the current is not injection limited, the current will be only limited by the organic semiconductor itself.^[145] As a rule of thumb the difference in work function of the injecting electrode and the energy level of the semiconductor should be < 0.3 eV to achieve Ohmic injection.^[146] “Ohmic contact” can be a misleading term. It does not mean that the current follows Ohm’s law across the whole measurement, i. e. a linear dependence of the current density J on the voltage V . But, the relation of J and V is only linear at low V . Here, fewer charge carriers per volume are injected than are present in the material. The corresponding resistance is Ohmic. In an ideal organic semiconductor without intrinsic charge carriers and only a small charge carrier density (n_0), the current density at low applied voltage is only due to these charge carriers. The current is in this case linear ($J = \sigma F$), assuming that the specific conductivity $\sigma = en_0\mu$ is constant and the electric field F is constant. An increase of the applied voltage leads to injection of charge carriers. When the density of excess charge carriers becomes larger than n_0 , the organic semiconductor contains a space charge. This space charge will determine the internal field and the current density extensively. Therefore, the J - V -characteristic becomes nonlinear. This can be explained by the SCLC model which was originally derived for molecular crystals.^[147,148]

We assume that the current is bulk-limited and the current density is determined by the drift current for large enough fields and mobility. The diffusive processes can be neglected since they are only significant near the contact and only the drift current determines the overall current. Thus, the current density can be described by

$$J = e\mu F - eD \frac{dn}{dx} \cong e\mu F \quad \text{Equation (11)}$$

with the mobility μ , the charge carrier density n , and the applied electric field F . The Poisson’s equation (equation 12) gives the electric field from the injected space charge.

$$\nabla F = \frac{en}{\varepsilon} \quad \text{Equation (12)}$$

where ϵ is the dielectric constant of the material. Consequently, the trap-free SCLC, known as Mott-Gurney law or SCLC square-law, is obtained by solving equations (11) and (12) for one dimension and constant mobility

$$J = \frac{9}{8} \epsilon \epsilon_0 \mu \frac{V^2}{L^3} \quad \text{Equation (13)}$$

with ϵ_0 being the permittivity of free space. Therefore, the current flowing through the insulator is proportional to the square of the Voltage and inversely proportional to the third power of the sample thickness. This current is named space charge limited current (SCLC). Thus, in an experiment one can clearly distinguish between an Ohmic current ($\propto VL^{-1}$) and SCLC ($\propto V^2 L^{-3}$). In the real case, the two electrodes commonly have different work functions. Therefore, a built-in potential V_{bi} exists which has to be taken into consideration for the evaluation of the J - V -curves. Also, the mobility is field dependent and traps are often present in organic semiconductors. For the evaluation of SCLC measurements the quadratic dependence of J and V , as well as the L^{-3} dependence have to be valid.^[149] For organic semiconductor polymers the dielectric constant is assumed to be 3.

Figure 16 illustrates the different regimes of a J - V curve in an exemplary single carrier device. First, the current density increases linearly with the voltage (Ohmic regime). For higher voltages it changes over to a quadratic dependence (SCLC regime). Here, the current is reduced by a factor that represents the ratio of free and total number of charge carrier. After all traps are filled, the trap-filling limit voltage V_{TFL} is reached and the device is in the SCLC trap-free regime.^[150] In most experiments, the trap-free regime cannot be found because high voltages are required.

Finally, the SCLC method can be used to characterize the charge transport properties of organic semiconductors. In recent years, this is done for many materials used in OPV.^[151,152] Thus, the determination of the hole and electron mobilities via SCLC measurements has become a versatile method. An advantage is that the layer thicknesses are often comparable to active layer thicknesses in OPV devices and the bulk charge carrier transport perpendicular to the substrate plane is monitored. Thus, one gets a realistic impression of the charge transport in an OPV cell by measuring an SCLC device compared to other methods such as OFET experiments. In this thesis, the SCLC method was extensively used for the investigation of charge transport properties of the synthesized polymers, especially for the comparison among them.

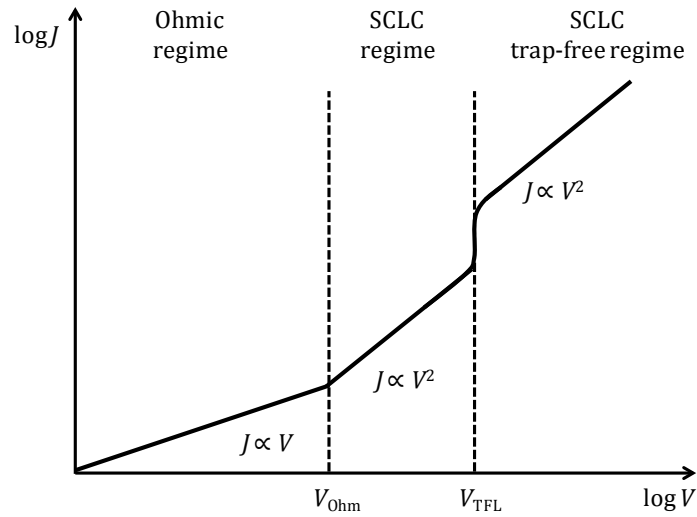


Figure 16. Log J vs. log V plot of an SCLC-characteristic including the three cases: I) linear regime, II) trap limited regime, and III) trap-free regime. Adapted from^[150]

Organic field effect transistors (OFET)

Another prominent method to determine the charge carrier mobility is the OFET measurement.^[153] In contrast to the methods described above, the OFET mobility does not describe the bulk property of the material. Rather a mobility in a very thin layer at the semiconductor/dielectric interface as a function of the gate voltage V_g is obtained. The setup of an OFET consists of three electrodes (see Figure 17): the source, drain and gate contact. A thin layer of the semiconducting material/polymer is placed between the source and drain of width W (channel width) having the distance L (channel length) between them. The semiconducting layer is separated from the gate electrode, often highly doped silicon, by an insulating gate dielectric (e. g. SiO_2).

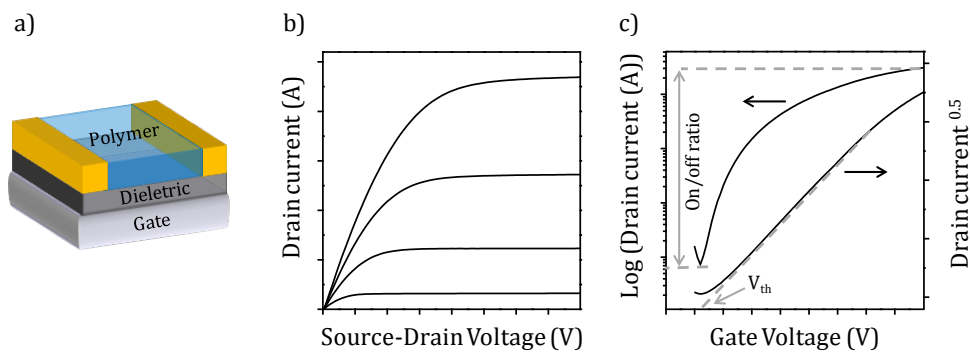


Figure 17. a) Schematic of an OFET in bottom gate architecture, b) OFET output characteristic, and c) OFET transfer characteristic in the saturation regime showing the on/off ratio and the threshold voltage V_{th} (intersection with the x-axis of the linear fit to the square root of the drain current).

Generally, voltage is applied to the gate electrode (V_g) and the drain electrode (V_d), whereas the source electrode is grounded ($V_s = 0$). The term V_g is used for the potential difference between gate and source and V_{ds} is used for the potential difference between source and drain. A negative gate voltage will accumulate positive charges (holes) at the insulator/semiconductor interface. As long as no source-drain bias is applied, the charge carrier concentration in the transistor channel is uniform (linear regime) and the current is directly proportional to V_{ds} . Increasing the source-drain voltage leads to an increase of the charge carrier concentration at the drain electrode. Further increase of the source-drain voltage gives rise to a depletion region next to the drain. Here, a so called “pinch off” point $V_{ds} = V_g - V_{th}$ is reached. After this point, increasing the voltage leads to a saturation of the current. For the evaluation of the OFET parameters two current-voltage characteristics have to be measured: the output and the transfer characteristic. First, the output characteristic (drain current vs. source-drain voltage for different constant gate voltages) shows the linear regime at low V_{ds} and the saturation regime at high V_{ds} . Second, from the transfer characteristic (drain current vs. gate voltage at constant V_{ds}), measured in the linear regime of the transistor, one can extract the onset voltage (V_{on}). In case of the transfer characteristic measured in the saturation regime, the square root of the drain current should be linearly dependent on the gate voltage. According to equation (16) one can calculate the mobility μ_{sat} , where C_i is the capacitance of the dielectric insulator.^[154]

$$I_{SD} = \frac{W}{2L} \mu_{sat} C_i (V_G - V_T)^2 \quad \text{Equation (16)}$$

For the complete characterization of the OFET the threshold voltage (V_{th}) has to be calculated. This can be done by extrapolating the linear fit to zero.

Consequently, the OFET measurement is a versatile tool for the characterization of organic semiconducting polymers. The p- or n-type behavior of unknown materials can be verified easily. The OFET mobility represents the properties of a very thin layer of the active material at the interface to the dielectric. Thus, the mobilities obtained from OFETs cannot be compared to the mobility of the bulk material, e. g. present in an organic solar cell.

1.6 Organic semiconductors for sensor applications

The unique properties of semiconducting polymers were not only used in OPVs, OLEDs, and OFETs but also for electrical sensor applications. In general, the analyte interaction with the sensor is transformed into an electrical signal. The configurations that are built up to evaluate the sensing behavior include chemiresistors, transistors, diodes, optic devices, piezoelectric crystal sensors, and amperometric sensors. Two overview reviews by Nylander and Bai can be addressed for further reading.^[155,156] In the following, the sensor configurations which are mainly used for organic semiconductors will be introduced: a) chemiresistors, b) OFETs, and c) diodes. Figure 18 illustrates the setups schematically.

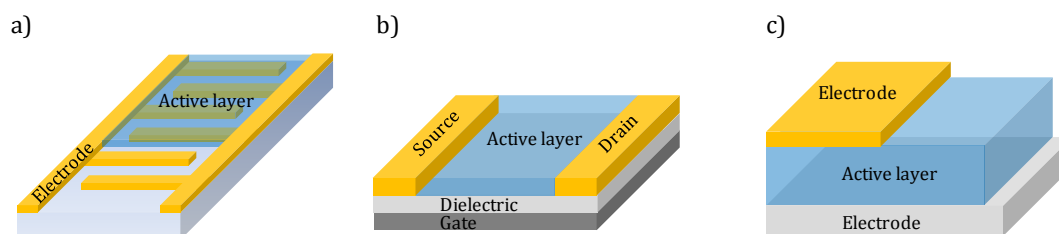


Figure 18. Schematic illustration of sensor configurations. a) Chemiresistor based on interdigitated electrodes, b) OFET with source, gate, and drain electrodes, and c) diode where the active layer is sandwiched between two electrodes.

A very simple and most commonly used setup is the two-terminal chemiresistor (Figure 18 a)). The electric resistance of that type of resistor is sensitive to the environment. Therefore, the measurement signal can be for example the resistance, a potential, or a current change. In order to improve the performance, interdigitated electrodes are applied.^[157] Usually, metal oxides as sensitive layers are used at high temperatures (200 to > 400 °C) in air. When a sensor with n-type metal oxide as active material is exposed to air, oxygen is adsorbed onto the semiconductor surface. Thus, a potential barrier at the grain boundaries is built up. At the high operating temperatures, the oxygen is able to trap electrons from the active material leading to a lower free charge carrier concentration and the formation of a depletion layer. Simultaneously, the resistance increases. Exposing the chemiresistor to a reducing gas, such as H₂, CH₄, CO or H₂S, the electrical resistance decreases due to the reduction of the depletion layer and the potential energy barrier. In contrast, an oxidizing gas, e. g. NO₂, increases the potential barrier and the thickness of the depletion layer leading to a higher measurable resistance.^[158] For p-type materials the same processes happen inversely. Thus, e. g. NO₂ leads to a decrease of the resistance and the conductivity increases. In order to find sensors for low temperature

operating, organic semiconducting polymers are under investigation for the detection of gases at room temperature. As an example, conducting poly(aniline) and poly(thiophene) films were shown to be efficient as NO₂ sensors using resistivity measurements.^[159,160]

OFET setups have emerged as an alternative to chemiresistors and are widely used for sensing applications. Here, a variety of materials exists for the detection in vapor or aqueous phase.^[161] The general setup and working principle of an OFET, which is a three-terminal device, was already described in chapter 1.5. The main advantage of an OFET sensor is the current modulation, which is possible due to the additional gate electrode. Hence, the current through the semiconductor can be adjusted over orders of magnitude resulting in an amplified sensor response. During the interaction with an analyte, the electrical characteristics of the OFET change. Thus, the bulk conductivity, the mobility, or the threshold voltage alter and can be monitored. There are several possible sensing mechanisms, including doping of the semiconductor or changes of the Schottky barrier height at the interface. However, it was shown by Andringa et al. that the sensing behavior in ZnO-based transistors arises from trapped charge carriers that are located at the gate dielectric.^[162] A similar behavior could be shown for n-type, p-type, and ambipolar organic semiconductors including a TPD based polymer.^[163]

In contrast to the more difficult setup of an OFET sensor, a diode setup is very simple (see Figure 18 b)). If the diode is exposed to an analyte, electric parameters such as the current density and the rectification behavior vary. It was shown that poly(pyrrole)/gold junctions have a significant response to NO_x gas which is due to the change in the Schottky barrier height and in the charge carrier concentration in the active layer.^[164] Both transistors and diodes have the advantage of providing more details of the semiconducting layer and the sensing behavior.

All the above mentioned sensors have in common that the electrical properties of the active material change upon exposure to an analyte. In a standard experiment, the sensor is exposed to different concentration pulses of a specific gas/gas mixture in a given period of time. The corresponding sensor signal is monitored. For a classical sensor the analyte is adsorbed during exposure to a certain gas and the actual concentration can be detected. When the sensor is not exposed to the analyte, desorption occurs and the signal recovers. In order to achieve information about the overall concentration for a given time period, the sensor signal has to be mathematically integrated in an additional step. This is not precise because of slow sensor response and recovery times as well as baseline drifts. Furthermore, the detection of integrated concentration values inherits the disadvantage of continuous switching between clean air and the analyte.^[165] However, for many applications maximum concentration requirements in emission or immission (the amount of adsorbed pollutant or the concentration taken in) have to be fulfilled. A promising approach to overcome these disadvantages is the so called dosimeter-

type, accumulating, or integrating sensing principle.^[166] Here, the analyte molecules accumulate in the sensitive layer. This leads to an additive change of electrical properties. The accumulation is either due to strong analyte sorption or a chemical reaction between analyte and receptor. In Figure 19 a comparison of the classical sensor behavior and the dosimeter behavior is shown.

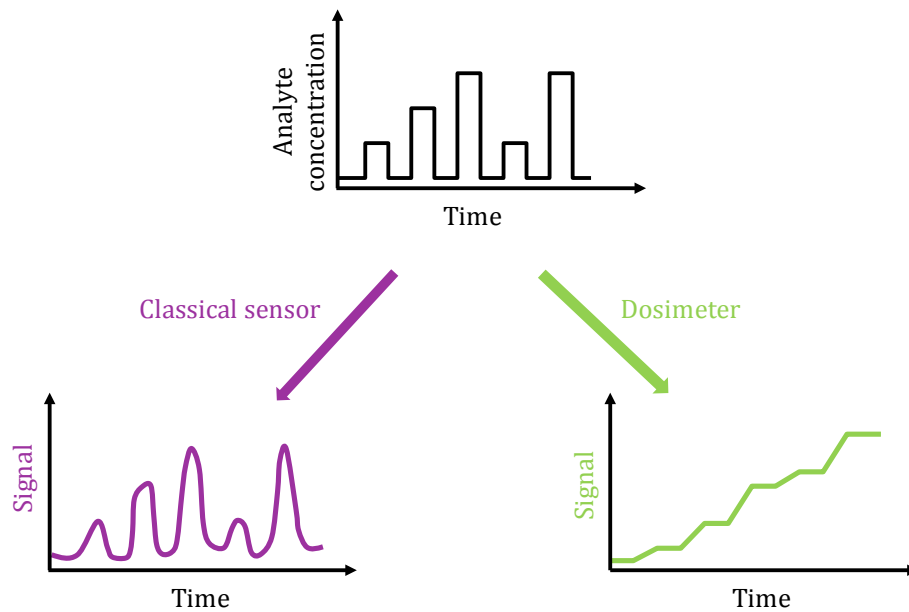


Figure 19. Comparison of the classical sensor (violet) and a dosimeter (green) behavior. Adapted from^[166]

In the case of a dosimeter, through equation (15) the analyte amount or cumulated exposure A_c is given by the time integral of the analyte concentration ($c(t)$) with the starting point of the sorption interval (t_0) in accordance with the sensor signal.

$$A_c = \int_{t_0}^t c(t) dt \quad \text{Equation (15)}$$

The analyte molecules can be released in a regeneration step. This can be done e. g. thermally or chemically.

1.7 References

- [1] R. R. Søndergaard, N. Espinosa, M. Jørgensen, F. C. Krebs, *Energy Environ. Sci.* 2014, 7, 1006.
- [2] F. C. Krebs, N. Espinosa, M. Hösel, R. R. Søndergaard, M. Jørgensen, *Adv. Mater.* 2014, 26, 29.
- [3] http://www.heliatek.com/newscenter/latest_news/heliatek-erzielt-effizienzrekord-mit-40-transparenten-organischen-solarzellen/?lang=en, 28.04.2014.
- [4] <http://www.robaid.com/tech/epfls-new-convention-center-west-facade-features-dye-solar-cells.htm>, 28.04.2014.
- [5] C. J. Brabec, V. Dyakonov, U. Scherf, *Organic photovoltaics: Materials, device physics and manufacturing technologies*, Wiley-VCH, Weinheim 2008.
- [6] Z. He, C. Zhong, S. Su, M. Xu, H. Wu, Y. Cao, *Nature Photonics (Nature Photonics)* 2012, 6, 593.
- [7] J. You, C.-C. Chen, Z. Hong, K. Yoshimura, K. Ohya, R. Xu, S. Ye, J. Gao, G. Li, Y. Yang, *Adv. Mater. Weinheim* 2013, 25, 3973.
- [8] R. Po, A. Bernardi, A. Calabrese, C. Carbonera, G. Corso, A. Pellegrino, *Energy Environ. Sci.* 2014, 7, 925.
- [9] http://www.heliatek.com/newscenter/latest_news/heliatek-erzielt-effizienzrekord-mit-40-transparenten-organischen-solarzellen/?lang=en.
- [10] C. W. Tang, *Appl. Phys. Lett.* 1986, 48, 183.
- [11] Halls, J. J. M., K. Pichler, R. H. Friend, S. C. Moratti, A. B. Holmes, *Appl. Phys. Lett.* 1996, 68, 3120.
- [12] A. Haugeneder, M. Neges, C. Kallinger, W. Spirkl, U. Lemmer, J. Feldmann, U. Scherf, E. Harth, A. Gügel, K. Müllen, *Phys. Rev. B* 1999, 59, 15346.
- [13] B. Maennig, D. Gebeyehu, P. Simon, F. Kozlowski, A. Werner, F. Li, S. Grundmann, S. Sonntag, M. Koch, K. Leo, M. Pfeiffer, H. Hoppe, D. Meissner, N. S. Sariciftci, I. Riedel, V. Dyakonov, J. Parisi, J. Drechsel, *Applied Physics A: Materials Science & Processing* 2004, 79, 1.

- [14] G. Yu, J. Gao, J. C. Hummelen, F. Wudl, A. J. Heeger, *Science* 1995, 270, 1789.
- [15] C. J. Brabec, N. S. Sariciftci, J. C. Hummelen, *Advanced Functional Materials* 2001, 11, 15.
- [16] B. O'Regan, M. Grätzel, *Nature* 1991, 353, 737.
- [17] A. Yella, H.-W. Lee, H. N. Tsao, C. Yi, A. K. Chandiran, M. K. Nazeeruddin, E. W.-G. Diao, C.-Y. Yeh, S. M. Zakeeruddin, M. Gratzel, *Science* 2011, 334, 629.
- [18] J. Burschka, A. Dualeh, F. Kessler, E. Baranoff, N.-L. Cevey-Ha, C. Yi, M. K. Nazeeruddin, M. Grätzel, *J. Am. Chem. Soc.* 2011, 133, 18042.
- [19] A. Kojima, K. Teshima, Y. Shirai, T. Miyasaka, *J. Am. Chem. Soc.* 2009, 131, 6050.
- [20] National Renewable Energy Laboratory 2014,
http://www.nrel.gov/ncpv/images/efficiency_chart.jpg.
- [21] H. J. Snaith, *J. Phys. Chem. Lett.* 2013, 4, 3623.
- [22] D. Weber, *Z. Naturforsch., B: Anorg. Chem., Org. Chem.* 197, 33, 1445.
- [23] T. Baikie, Y. Fang, J. M. Kadro, M. Schreyer, F. Wei, S. G. Mhaisalkar, M. Graetzel, T. J. White, *J. Mater. Chem. A* 2013, 1, 5628.
- [24] J.-H. Im, J. Chung, S.-J. Kim, N.-G. Park, *Nanoscale Res Lett* 2012, 7, 353.
- [25] C. C. Stoumpos, C. D. Malliakas, M. G. Kanatzidis, *Inorg. Chem.* 2013, 52, 9019.
- [26] N. K. Noel, S. D. Stranks, A. Abate, C. Wehrenfennig, S. Guarnera, A. Haghighirad, A. Sadhanala, G. E. Eperon, S. K. Pathak, M. B. Johnston, A. Petrozza, L. Herz, H. Snaith, *Energy Environ. Sci.* 2014.
- [27] S. Kazim, M. K. Nazeeruddin, M. Grätzel, S. Ahmad, *Angew. Chem. Int. Ed.* 2014, 53, 2812.
- [28] H.-S. Kim, C.-R. Lee, J.-H. Im, K.-B. Lee, T. Moehl, A. Marchioro, S.-J. Moon, R. Humphry-Baker, J.-H. Yum, J. E. Moser, M. Grätzel, N.-G. Park, *Sci. Rep.* 2012, 2.
- [29] S. D. Stranks, G. E. Eperon, G. Grancini, C. Menelaou, Alcocer, M. J. P., T. Leijtens, L. M. Herz, A. Petrozza, H. J. Snaith, *Science* 2013, 342, 341.
- [30] G. Xing, N. Mathews, S. Sun, S. S. Lim, Y. M. Lam, M. Grätzel, S. Mhaisalkar, T. C. Sum, *Science* 2013, 342, 344.
- [31] E. Edri, S. Kirmayer, A. Henning, S. Mukhopadhyay, K. Gartsman, Y. Rosenwaks, G. Hodes, D. Cahen, *Nano Lett.* 2014, 14, 1004.

- [32] M. Liu, M. B. Johnston, H. J. Snaith, *Nature* 2013, 501, 395.
- [33] D. Liu, T. L. Kelly, *Nature Photon* 2013, 8, 133.
- [34] J. Burschka, N. Pellet, S.-J. Moon, R. Humphry-Baker, P. Gao, M. K. Nazeeruddin, M. Grätzel, *Nature* 2013, 499, 316.
- [35] Q. Chen, H. Zhou, Z. Hong, S. Luo, H.-S. Duan, H.-H. Wang, Y. Liu, G. Li, Y. Yang, *J. Am. Chem. Soc.* 2014, 136, 622.
- [36] E. E. Havinga, W. ten Hoeve, H. Wynberg, *Synthetic Metals* 1993, 55, 299.
- [37] Q. T. Zhang, J. M. Tour, *J. Am. Chem. Soc.* 1998, 120, 5355.
- [38] J. Roncali, *Chem. Rev.* 1997, 97, 173.
- [39] C. L. Chochos, S. A. Choulis, *Progress in Polymer Science* 2011, 36, 1326.
- [40] E. Bundgaard, F. C. Krebs, *Solar Energy Materials and Solar Cells* 2007, 91, 954.
- [41] T. Yamamoto, Y. Hayashi, A. Yamamoto, *Bull. Chem. Soc. Jpn.* 1978, 51, 2091.
- [42] K. Tamao, K. Sumitani, M. Kumada, *J. Am. Chem. Soc.* 1972, 94, 4374.
- [43] I. Osaka, R. D. McCullough, *Acc. Chem. Res.* 2008, 41, 1202.
- [44] R. H. Lohwasser, M. Thelakkat, *Macromolecules* 2011, 44, 3388.
- [45] M. C. Stefan, A. E. Javier, I. Osaka, R. D. McCullough, *Macromolecules* 2009, 42, 30.
- [46] N. Miyaoura, K. Yamada, A. Suzuki, *Tetrahedron Letters* 1979, 20, 3437.
- [47] M. Rehahn, A.-D. Schlüter, G. Wegner, W. Feast, *Polymer* 1989, 30, 1060.
- [48] J. Sakamoto, M. Rehahn, G. Wegner, A. D. Schlüter, *Macromol. Rapid Commun.* 2009, 30, 653.
- [49] A. Neubig, M. Thelakkat, *Polymer* 2014, 55, 2624.
- [50] T. Yokozawa, R. Suzuki, M. Nojima, Y. Ohta, A. Yokoyama, *Macromol. Rapid Commun.* 2011, 32, 801.
- [51] E. Elmalem, A. Kiriy, W. T. S. Huck, *Macromolecules* 2011, 44, 9061.
- [52] D. Milstein, J. K. Stille, *J. Am. Chem. Soc.* 1978, 100, 3636.
- [53] J. K. Stille, *Angew. Chem. Int. Ed. Engl.* 1986, 25, 508.

- [54] Z. Bao, W. K. Chan, L. Yu, *J. Am. Chem. Soc.* 1995, *117*, 12426.
- [55] B. Carsten, F. He, H. J. Son, T. Xu, L. Yu, *Chem. Rev.* 2011, *111*, 1493.
- [56] W. A. Braunecker, S. D. Oosterhout, Z. R. Owczarczyk, R. E. Larsen, B. W. Larson, D. S. Ginley, O. V. Boltalina, S. H. Strauss, N. Kopidakis, D. C. Olson, *Macromolecules* 2013, *46*, 3367.
- [57] J. Pei, S. Wen, Y. Zhou, Q. Dong, Z. Liu, J. Zhang, W. Tian, *New J. Chem.* 2011, *35*, 385.
- [58] T. Yamamoto, A. Morita, Y. Miyazaki, T. Maruyama, H. Wakayama, Z. H. Zhou, Y. Nakamura, T. Kanbara, S. Sasaki, K. Kubota, *Macromolecules* 1992, *25*, 1214.
- [59] J. Ostrauskaite, P. Strohriegl, *Macromol. Chem. Phys.* 2003, *204*, 1713.
- [60] T. T. Tsou, J. K. Kochi, *J. Am. Chem. Soc.* 1979, *101*, 7547.
- [61] Y.-J. Cheng, S.-H. Yang, C.-S. Hsu, *Chem. Rev.* 2009, *109*, 5868.
- [62] L. Bian, E. Zhu, J. Tang, W. Tang, F. Zhang, *Progress in Polymer Science* 2012, *37*, 1292.
- [63] R. D. McCullough, R. D. Lowe, M. Jayaraman, D. L. Anderson, *J. Org. Chem.* 1993, *58*, 904.
- [64] H. Sirringhaus, P. J. Brown, R. H. Friend, M. M. Nielsen, K. Bechgaard, Langeveld-Voss, B. M. W., Spiering, A. J. H., Janssen, R. A. J., E. W. Meijer, P. Herwig, de Leeuw, D. M., *Nature* 1999, *401*, 685.
- [65] C. R. Singh, G. Gupta, R. Lohwasser, S. Engmann, J. Balko, M. Thelakkat, T. Thurn-Albrecht, H. Hoppe, *J. Polym. Sci. Part B: Polym. Phys.* 2013, *51*, 943.
- [66] C. J. Neef, J. P. Ferraris, *Macromolecules* 2000, *33*, 2311.
- [67] F. Zhang, M. Johansson, M. R. Andersson, J. C. Hummelen, O. Inganäs, *Advanced Materials* 2002, *14*, 662.
- [68] V. Shrotriya, E. H.-E. Wu, G. Li, Y. Yao, Y. Yang, *Appl. Phys. Lett.* 2006, *88*, 64104.
- [69] K. Colladet, S. Fourier, T. J. Cleij, L. Lutsen, J. Gelan, D. Vanderzande, Le Huong Nguyen, H. Neugebauer, S. Sariciftci, A. Aguirre, G. Janssen, E. Goovaerts, *Macromolecules* 2007, *40*, 65.
- [70] S. Ducharme, P. M. Borsenberger, *Xerographic photoreceptors and photorefractive polymers: Conference Papers*, SPIE 1995.
- [71] M. Thelakkat, *Macromolecular Materials and Engineering* 2002, *287*, 442.

- [72] P. M. Borsenberger, W. T. Gruenbaum, L. J. Sorriero, N. Zumbulyadis, *Jpn. J. Appl. Phys.* 1995, *34*, L1597.
- [73] A. Iwan, D. Sek, *Progress in Polymer Science* 2011, *36*, 1277.
- [74] J. Veres, S. Ogier, G. Lloyd, D. de Leeuw, *Chem. Mater.* 2004, *16*, 4543.
- [75] Iain McCulloch, Martin Heeney, *Material Matters* 2009.
- [76] J. H. Sim, K. Yamada, S. H. Lee, S. Yokokura, H. Sato, *Synthetic Metals* 2007, *157*, 940.
- [77] C. Takahashi, S. Moriya, N. Fugono, H. C. Lee, H. Sato, *Synthetic Metals* 2002, *129*, 123.
- [78] W. Shi, S. Fan, F. Huang, W. Yang, R. Liu, Y. Cao, *J. Mater. Chem.* 2006, *16*, 2387.
- [79] W.-L. Yu, J. Pei, W. Huang, A. J. Heeger, *Chem. Commun.* 2000, *8*, 682.
- [80] F. E. Goodson, S. I. Hauck, J. F. Hartwig, *J. Am. Chem. Soc.* 1999, *121*, 7527.
- [81] M. Horie, Y. Luo, J. J. Morrison, L. A. Majewski, A. Song, B. R. Saunders, M. L. Turner, *J. Mater. Chem.* 2008, *18*, 5230.
- [82] H. Sato, K. Ogino, H. Hirai, *Macromolecular Symposia* 2001, *175*, 159.
- [83] J. M. Son, T. Mori, K. Ogino, H. Sato, Y. Ito, *Macromolecules* 1999, *32*, 4849.
- [84] M. Thelakkat, J. Hagen, D. Haarer, H.-W. Schmidt, *Synthetic Metals* 1999, *102*, 1125.
- [85] E. M. Barea, G. Garcia-Belmonte, M. Sommer, S. Hüttner, H. J. Bolink, M. Thelakkat, *Thin Solid Films* 2010, *518*, 3351.
- [86] M. Zorn, Weber, Stefan A L, M. N. Tahir, W. Tremel, H.-J. Butt, R. Berger, R. Zentel, *Nano Lett.* 2010, *10*, 2812.
- [87] E. Bellmann, S. E. Shaheen, R. H. Grubbs, S. R. Marder, B. Kippelen, N. Peyghambarian, *Chem. Mater.* 1999, *11*, 399.
- [88] U. Scherf, E. List, *Advanced Materials* 2002, *14*, 477.
- [89] J. Li, F. Dierschke, J. Wu, A. C. Grimsdale, K. Müllen, *J. Mater. Chem.* 2006, *16*, 96.
- [90] Y. Li, Y. Wu, B. S. Ong, *Macromolecules* 2006, *39*, 6521.
- [91] P.-L. T. Boudreault, S. Wakim, N. Blouin, M. Simard, C. Tessier, Y. Tao, M. Leclerc, *J. Am. Chem. Soc.* 2007, *129*, 9125.

- [92] F. Wudl, M. Kobayashi, A. J. Heeger, *J. Org. Chem.* 1984, *49*, 3382.
- [93] P. Coppo, M. L. Turner, *J. Mater. Chem.* 2005, *15*, 1123.
- [94] S. Yamaguchi, K. Tamao, *Bull. Chem. Soc. Jpn.* 1996, *69*, 2327.
- [95] K. Ogawa, S. C. Rasmussen, *Macromolecules* 2006, *39*, 1771.
- [96] H. Pan, Y. Li, Y. Wu, P. Liu, B. S. Ong, S. Zhu, G. Xu, *J. Am. Chem. Soc.* 2007, *129*, 4112.
- [97] K. Lee, G. A. Sotzing, *Macromolecules* 2001, *34*, 5746.
- [98] D. R. Rutherford, J. K. Stille, C. M. Elliott, V. R. Reichert, *Macromolecules* 1992, *25*, 2294.
- [99] Z. Zhang, J. Wang, *J. Mater. Chem* 2012, *22*, 4178.
- [100] M. Svensson, F. Zhang, S. C. Veenstra, W. Verhees, J. C. Hummelen, J. M. Kroon, O. Inganäs, M. R. Andersson, *Adv. Mater.* 2003, *15*, 988.
- [101] N. Blouin, A. Michaud, D. Gendron, S. Wakim, E. Blair, R. Neagu-Plesu, M. Belletête, G. Durocher, Y. Tao, M. Leclerc, *J. Am. Chem. Soc.* 2008, *130*, 732.
- [102] Y. Liang, Z. Xu, J. Xia, S.-T. Tsai, Y. Wu, G. Li, C. Ray, L. Yu, *Adv. Mater* 2010, *22*, E135.
- [103] H.-R. Tseng, H. Phan, C. Luo, M. Wang, L. A. Perez, S. N. Patel, L. Ying, E. J. Kramer, T.-Q. Nguyen, G. C. Bazan, A. J. Heeger, *Adv. Mater.* 2014, *26*, 2998.
- [104] K. H. Hendriks, Heintges, Gaël H L, V. S. Gevaerts, M. M. Wienk, Janssen, René A J, *Angew. Chem. Int. Ed. Engl.* 2013, *52*, 8341.
- [105] J. Warnan, C. Cabanetos, R. Bude, A. El Labban, L. Li, P. M. Beaujuge, *Chem. Mater.* 2014, *26*, 2835.
- [106] T. Yasuda, Y. Shinohara, T. Matsuda, L. Han, T. Ishi-i, *J. Mater. Chem* 2012, *22*, 2544.
- [107] S. Beaupré, J. Dumas, M. Leclerc, *Chem. Mater.* 2006, *18*, 4011.
- [108] A. R. Rabindranath, Y. Zhu, K. Zhang, B. Tieke, *Polymer* 2009, *50*, 1637.
- [109] J. Lee, S. Cho, J. H. Seo, P. Anant, J. Jacob, C. Yang, *J. Mater. Chem.* 2011, *22*, 1504.
- [110] F. Huang, K.-S. Chen, H.-L. Yip, S. K. Hau, O. Acton, Y. Zhang, J. Luo, A. K.-Y. Jen, *Journal of the American Chemical Society* 2009, *131*, 13886.
- [111] Z.-G. Zhang, K.-L. Zhang, G. Liu, C.-X. Zhu, K.-G. Neoh, E.-T. Kang, *Macromolecules* 2009, *42*, 3104.

- [112] F. Huang, K.-S. Chen, H.-L. Yip, S. K. Hau, O. Acton, Y. Zhang, J. Luo, A. K.-Y. Jen, *J. Am. Chem. Soc.* 2009, *131*, 13886.
- [113] J. C. Hummelen, B. W. Knight, F. LePeq, F. Wudl, J. Yao, C. L. Wilkins, *J. Org. Chem.* 1995, *60*, 532.
- [114] H. W. Kroto, J. R. Heath, S. C. O'Brien, R. F. Curl, R. E. Smalley, *Nature* 1985, *318*, 162.
- [115] V. Kamm, G. Battagliarin, I. A. Howard, W. Pisula, A. Mavrinskiy, C. Li, K. Müllen, F. Laquai, *Adv. Energy Mater.* 2011, *1*, 297.
- [116] L. Schmidt-Mende, A. Fechtenkötter, K. Müllen, E. Moons, R. H. Friend, J. D. MacKenzie, *Science* 2001, *293*, 1119.
- [117] F. Lüttich, D. Lehmann, M. Friedrich, Z. Chen, A. Facchetti, C. v. Borczyskowski, Zahn, Dietrich R. T., H. Graaf, *Phys. Status Solidi A* 2012, *209*, 585.
- [118] Y.-J. Hwang, N. M. Murari, S. A. Jenekhe, *Polym. Chem.* 2013, *4*, 3187.
- [119] S. Hüttner, M. Sommer, M. Thelakkat, *Appl. Phys. Lett.* 2008, *92*, 93302.
- [120] A. Babel, S. A. Jenekhe, *J. Am. Chem. Soc.* 2003, *125*, 13656.
- [121] H. Li, F. S. Kim, G. Ren, S. A. Jenekhe, *J. Am. Chem. Soc.* 2013, *135*, 14920.
- [122] Y. Takeda, T. L. Andrew, J. M. Lobez, A. J. Mork, T. M. Swager, *Angew. Chem. Int. Ed.* 2012, *51*, 9042.
- [123] X. Zhan, Z. Tan, B. Domercq, Z. An, X. Zhang, S. Barlow, Y. Li, D. Zhu, B. Kippelen, S. R. Marder, *J. Am. Chem. Soc.* 2007, *129*, 7246.
- [124] H. Yan, Z. Chen, Y. Zheng, C. Newman, J. R. Quinn, F. Dötz, M. Kastler, A. Facchetti, *Nature* 2009, *457*, 679.
- [125] B. Sun, W. Hong, Z. Yan, H. Aziz, Y. Li, *Adv. Mater. Weinheim* 2014, *26*, 2636.
- [126] X. Zhao, X. Zhan, *Chem Soc Rev* 2011, *40*, 3728.
- [127] R. H. Friend, M. Granström, K. Petritsch, A. C. Arias, A. Lux, M. R. Andersson, *Nature* 1998, *395*, 257.
- [128] L. C. Chen, D. Godovsky, O. Inganäs, J. C. Hummelen, Janssens, R. A. J., M. Svensson, M. R. Andersson, *Advanced Materials* 2000, *12*, 1367.

- [129] T. W. Holcombe, C. H. Woo, Kavulak, David F J, B. C. Thompson, Fréchet, Jean M J, *J. Am. Chem. Soc.* 2009, *131*, 14160.
- [130] Y. Kim, E. Lim, *Polymers* 2014, *6*, 382.
- [131] V. Coropceanu, J. Cornil, D. A. da Silva Filho, Y. Olivier, R. Silbey, J.-L. Brédas, *Chem. Rev.* 2007, *107*, 926.
- [132] J. Yamashita, T. Kurosawa, *Journal of Physics and Chemistry of Solids* 1958, *5*, 34.
- [133] T. Holstein, *Annals of Physics* 1959, *8*, 325.
- [134] K. Fesser, A. Bishop, D. Campbell, *Phys. Rev. B* 1983, *27*, 4804.
- [135] H. Bässler, *phys. stat. sol. (b)* 1993, *175*, 15.
- [136] A. Miller, E. Abrahams, *Phys. Rev.* 1960, *120*, 745.
- [137] R. Marcus, *Rev. Mod. Phys.* 1993, *65*, 599.
- [138] T. Holstein, *Annals of Physics* 1959, *8*, 343.
- [139] D. Emin, *Advances in Physics* 1975, *24*, 305.
- [140] L. Friedman, *Phys. Rev.* 1964, *135*, A233.
- [141] Y. Gartstein, E. M. Conwell, *Chemical Physics Letters* 1995, *245*, 351.
- [142] M. O'Neill, S. M. Kelly, *Adv. Mater. Weinheim* 2011, *23*, 566.
- [143] D. Hertel, H. Bässler, U. Scherf, H. H. Hörhold, *J. Chem. Phys.* 1999, *110*, 9214.
- [144] S. Baranovski, *Charge transport in disordered solids with applications in electronics*, Wiley, Chichester, England 2006, 276.
- [145] M. Schwoerer, H. C. Wolf, *Organic Molecular Solids*, Wiley-VCH, Hoboken 2008, 217-305.
- [146] P. S. Davids, I. H. Campbell, D. L. Smith, *J. Appl. Phys.* 1997, *82*, 6319.
- [147] Lampert, M. A., Mark, P., *Current Injection in Solids (Academic Press, New York)* 1970.
- [148] N. F. Mott, R. W. Gurney, *Electronic processes in ionic crystals (Clarendon Press, Oxford)*, 1940, 172.
- [149] U. Wolf, S. Barth, H. Bässler, *Appl. Phys. Lett.* 1999, *75*, 2035.

- [150] O. Ostroverkhova, *Handbook of organic materials for optical and (opto)electronic devices: Properties and applications*, Elsevier, 2013, 358.
- [151] Y. Liang, D. Feng, Y. Wu, S.-T. Tsai, G. Li, C. Ray, L. Yu, *J. Am. Chem. Soc.* 2009, *131*, 7792.
- [152] C. Goh, R. J. Kline, M. D. McGehee, E. N. Kadnikova, J. M. J. Fréchet, *Applied Physics Letters* 2005, *86*, 122110.
- [153] J. Zaumseil, H. Sirringhaus, *Chem. Rev.* 2007, *107*, 1296.
- [154] J. R. Groza, *Organic field-effect transistors*, Taylor & Francis, Boca Raton 2007.
- [155] C. Nylander, *Journal of Physics E: Scientific Instruments* 1985, *18*, 750.
- [156] Hua Bai, Gaoquan Shi, *Sensors* 2007, *7*, 307.
- [157] N.E. Agbor, M.C. Petty, A.P. Monkman, *Sensors and Actuators B: Chemical* 1995, *28*, 173.
- [158] A.-M. Andringa, C. Piliago, I. Katsouras, P. W. M. Blom, D. M. de Leeuw, *Chem. Mater.* 2013, *26*, 785.
- [159] M. K. Ram, O. Yavuz, M. Aldissi, *Synthetic Metals* 2005, *151*, 77.
- [160] P. Schottland, M. Bouguettaya, C. Chevrot, *Synthetic Metals* 1999, *102*, 1325.
- [161] M. E. Roberts, A. N. Sokolov, Z. Bao, *J. Mater. Chem.* 2009, *19*, 3351.
- [162] A.-M. Andringa, J. R. Meijboom, E. C. P. Smits, S. G. J. Mathijssen, P. W. M. Blom, de Leeuw, Dago M., *Adv. Funct. Mater.* 2011, *21*, 100.
- [163] F. Gholamrezaie, A.-M. Andringa, Roelofs, W. S. Christian, A. Neuhold, M. Kemerink, P. W. M. Blom, de Leeuw, Dago M., *Small* 2012, *8*, 241.
- [164] V.C. Nguyen, K. Potje-Kamloth, *Thin Solid Films* 1999, *338*, 142.
- [165] A. Schütze, N. Pieper, J. Zacheja, *Sensors and Actuators B: Chemical* 1995, *23*, 215.
- [166] I. Marr, A. Groß, R. Moos, *Journal of Sensors and Sensor Systems* 2014, *3*, 29.

Objective of the Thesis

The aim of this thesis is, on the one hand, to derive a fundamental correlation between delocalization effects in a polymer chain and exciton dissociation. On the other hand, the suitability of triphenylamine (TPA)-type main-chain polymers for novel applications such as perovskite solar cells and dosimeters to detect and assay NO_x was tested. For this purpose, tailor-made main-chain polymers based on tetraphenylbenzidine (TPD) and TPA were synthesized. The focus is laid on the development of polymers with an optimal designed structure in order to achieve essential properties such as hole transport, light absorption or solubility for the desired application. Detailed investigations regarding charge carrier transport, electronic and optical properties as well as doping effects are addressed.

Lead halide perovskite solar cells are an emerging new research field which recently underwent a tremendous development. However, there are still challenges to improve the performance of these solar cells. Key issues are a) how to form big perovskite ($\text{CH}_3\text{NH}_3\text{PbX}_3$, X = Cl, Br, I) crystals and smooth surfaces? And b) what is the design rule for suitable hole injecting layers? In the first part of this thesis, a one-pot fabrication method shall be tested to improve the morphology of the solar cell and simplify the preparation procedure. Therefore, a tailor-made PTPD needs to be designed for the requirements such as solubility and compatibility with the perovskite precursors in a common solvent. A particular focus will be laid on the fabrication method. In order to characterize the corresponding solar cells, measurements of the current-voltage characteristics, the external quantum efficiency, and the optical absorption shall be employed. Furthermore, the question of suitable hole injecting materials for devices shall be investigated. Therefore, in the second part perovskite solar cells with the different PTPDs shall be prepared in a conventional two step approach and characterized in detail. A comparison of PTPDs with polar and non-polar side chains and a detailed investigation of the hole transport mobility and doping effects shall be addressed.

Further, PTPDs shall be investigated as active materials for detecting and assay of NO_2 in gas-sensors. Integrating gas-sensors (dosimeters) can accumulate the analyte gas which enables the detection of the exposure during a period of time and the actual concentration in one system. Conventional integrating gas-sensors based on metal oxides operate at elevated temperatures. Thus, the use of organic semiconducting polymers which can be used at room temperature is

desirable. Furthermore, the processability from solution allows a low cost fabrication of the sensors with printing techniques. In this work, PTPDs shall be used due to their suitable oxidation potential and good hole carrier transport. The resistivity measured by impedance spectroscopy shall be applied as sensor signal and the influence of doping and addition of conducting salts on the sensor performance shall be investigated.

In the above mentioned applications PTPD homopolymers with a large optical gap are used. However, it is desirable to tune the absorption behavior of PTPDs towards the long wavelength region to improve the light harvesting property for the use in organic solar cells. The donor-acceptor (D-A) concept is a well-known method to lower the optical gap. Here, two strategies are known in the literature: 1) Donor and acceptor alternating in the polymer main-chain and 2) incorporation of the acceptor to the polymer (donor) side chain. To evaluate the advantages of these concepts, a comparison of the two strategies with respect to the influence of the excited state charge-transfer (CT) character, delocalization and hole transport on charge separation shall be investigated. Therefore, novel D-A copolymers based on TPA involving both strategies shall be synthesized. A variety of techniques such as cyclic voltammetry, UV-vis and fluorescence spectroscopy and SCLC measurements shall be employed for characterization. Finally, the influence of the CT-character/delocalization on the charge separation shall be investigated in bilayer solar cells in a joint work with the physics.

Overview of the Thesis

This thesis focuses on charge carrier transport, doping and application of main-chain triphenylamine (TPA) and tetraphenylbenzidine (TPD) based organic semiconducting polymers in organic/hybrid photovoltaics and sensors. In particular, the effect of structural compositions of these hole transporting polymers on electronic and optical properties is addressed. Fundamental investigations of the properties tailored by the polymer structure are discussed. This is crucial, since PTPAs/PTPDs are widely used for applications such as organic field effect transistors (OFETs), organic light emitting diodes (OLEDs), sensors, and organic photovoltaics (OPVs). In this thesis, main-chain homopolymers as well as copolymers were synthesized. The polymers were applied in lead halide perovskite solar cells, bilayer solar cells and chemiresistors for gas sensing as depicted in Figure 1.

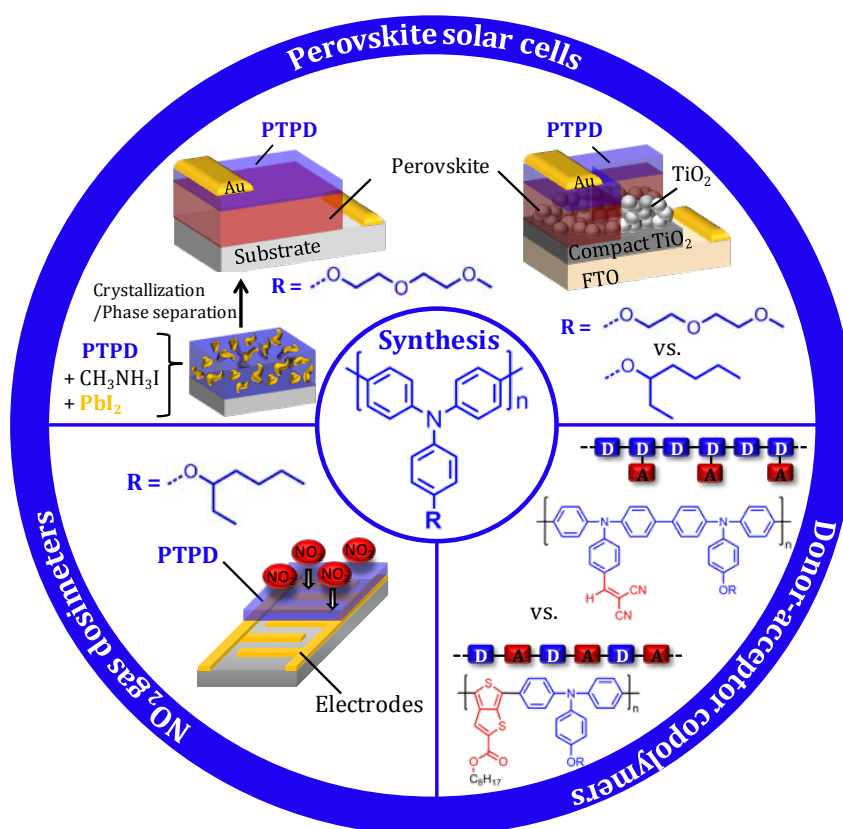


Figure 1. Overview of the thesis including the three main parts: perovskite solar cells, NO₂ gas dosimeters, and donor-acceptor copolymers.

In the case of the homopolymers, the properties were tailored by the introduction of either polar or non-polar side-chains and the control of the molecular weight. For the copolymers well selected comonomers were incorporated to change their optical and electronic properties in the desired way. Hence, the central issue combining all chapters is the design of PTPA/PTPD with variable properties which are necessary for each application. The thesis is divided into three main sections and contains five papers. Four appear in the main part and one can be found in the appendix.

In the first section, the design of PTPD homopolymers as suitable hole transport materials for perovskite solar cells is presented which is shown in the chapters 5 and 6. In chapter 5 an elegant novel approach towards the deposition of the active perovskite ($\text{CH}_3\text{NH}_3\text{PbI}_3$) and the hole transport layer in one single step was studied to improve and simplify the fabrication process. The strategy involves a controlled crystallization of the perovskite within a polymer matrix which leads to the formation of large crystals and a flat surface. For this, a PTPD with polar side chains was applied. The benefits of using the PTPD are the combination of good hole transport mobilities, solubility in polar solvents, and compatibility as well as miscibility with the perovskite precursors ($\text{CH}_3\text{NH}_3\text{I} + \text{PbI}_2$). Thus, we show that after spin coating and annealing a mixture of the PTPD and the precursors leads to a crystallization driven vertical phase separation resulting in the desired bilayer structure. In Chapter 6 the influence of the polarity of the side chains on the PTPD acting as hole conducting material at the interface to the perovskite layer in solar cells is addressed. Therefore, the perovskite solar cells were prepared in the conventional way, meaning that the perovskite layer and the hole transport material were deposited in two steps. Important questions regarding the properties of the hole conducting material for devices are presented.

The second section deals with the use of PTPDs for impedimetric NO_2 gas dosimeters (chapter 7). Gas dosimeters possess the particular feature that the actual concentration as well as the accumulated exposure of the analyte can be detected in one device. Therefore, the active material has to accumulate the analyte during exposure and no recovery after exposure is desirable to obtain the accumulated exposure. For the detection of NO_2 it is beneficial to apply an oxidizable material. The oxidation leads to a change of the conductivity and resistivity of the material. Thus, PTPDs with their suitable oxidation behavior in combination with good hole transport mobilities are presented as very promising materials. The pure, undoped PTPD behaves as a classical NO_2 sensor with a certain recovery of the sensor signal. However, it could be shown that doping of the PTPD and the addition of a conducting salt can lead to a reduction of the recovery and the accumulation of NO_2 in the PTPD layer. Thus, the adsorption and desorption rates can be tailored by doping and addition of conducting salt.

The third chapter addresses the question of tuning the optical behavior of PTPDs (chapter 8). Usually, PTPDs exhibit a large optical gap resulting in absorption in the short wavelength region. It is desirable to tune the absorption behavior in order to improve light harvesting in organic solar cells. Two strategies are known in the literature to reduce the optical gap by applying the donor-acceptor (D-A) concept: 1) Attachment of the acceptor unit to the side chain of the polymer and 2) incorporation of the acceptor unit into the main chain. Here, we study comparatively the two strategies. Two new D-A copolymers applying the two strategies resulting in different charge transfer (CT) character and delocalization were synthesized for this purpose. The effect of the delocalization on charge transport as well as on charge separation was investigated in detail.

In the following, an overview of the main results of each chapter is given. The detailed description of the experiments and results can be found in the individual chapters and their supporting information.

Crystallization-driven phase separation towards one pot fabrication of bilayer perovskite/polymer solar cells

This chapter deals with an innovative approach to fabricate the bilayer structure of perovskite and the hole transport layer in one step with improved control of the perovskite crystallization within a polymer matrix. The benefit of this strategy is to simplify the processing conditions of perovskite solar cells which is at the moment very challenging. Most important is the uniform film formation of the highly crystalline perovskite layer and full surface coverage. Therefore, we tailored a PTPD which is soluble in polar solvents and miscible as well as compatible with the perovskite precursors ($\text{CH}_3\text{NH}_3\text{I}$ and PbI_2). The PTPD carries ethylene glycol side chains to guarantee solubility in e. g. dimethylformamide or γ -butyrolactone. Furthermore, the amorphous character and low glass transition temperature of the polymer is favorable for this approach. In more detail, the perovskite precursors and the PTPD were dissolved in one solvent and spin coated on a fluorine doped tin oxide substrate having TiO_2 as blocking layer together with a mesoporous TiO_2 scaffold layer. Due to thermal annealing the crystallization driven vertical phase separation starts from the scaffold layer and the desired bilayer structure (PTPD on top of the perovskite layer) is formed. The strategy is depicted in Figure 2.

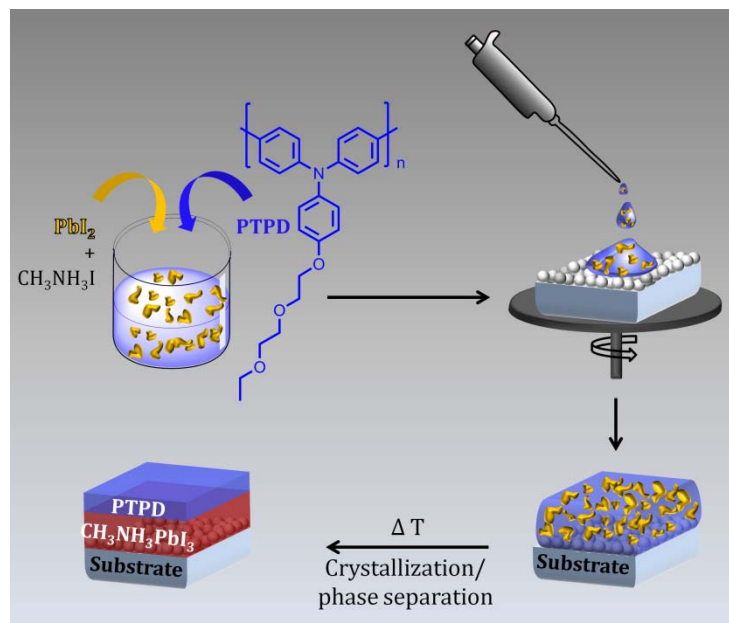


Figure 2. Schematic illustration of the crystallization driven phase separation towards the one pot fabrication of bilayer structure of perovskite and hole transport material. The precursor solution contains PTPD, $\text{CH}_3\text{NH}_3\text{I}$, and PbI_2 and. After thermal annealing and crystallization of the perovskite, the two-layer structure is formed.

In order to investigate the layered structure of the device, scanning electron microscopy (SEM) pictures were recorded. Figure 3 shows the structure of a device prepared by the one-pot fabrication method of hole transport material and perovskite layer as well as an top-view image.

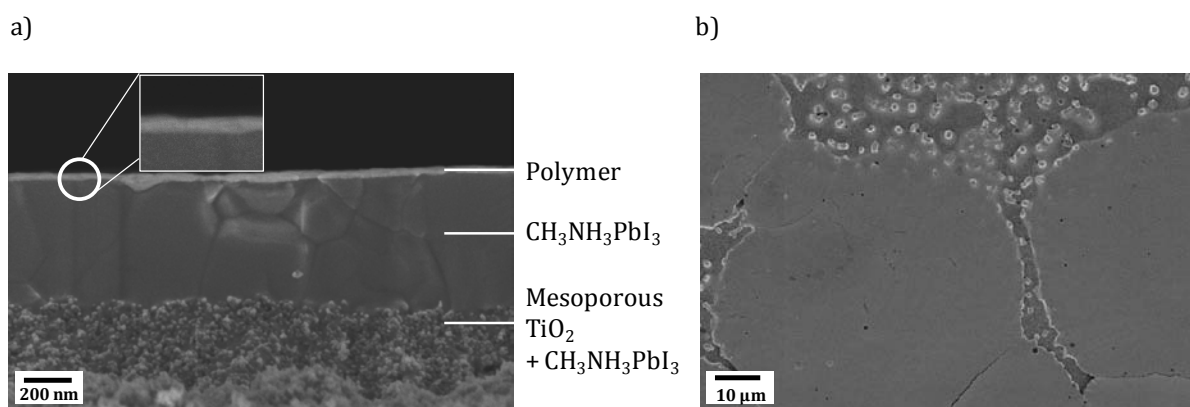


Figure 3. a) Cross-sectional SEM image of a device with perovskite/polymer layer prepared by spin-coating on mesoporous TiO_2 from precursor solution (PTPD + $\text{CH}_3\text{NH}_3\text{I}$ + PbI_2). Annealing was done at $135\text{ }^\circ\text{C}$ for 10 min. b) Corresponding top-view.

Finally, the photovoltaic characterization of the devices revealed appreciably high efficiency. The devices showed a good fill factor of 0.59 % and an efficiency of around 5 %. Additionally, the crystallization driven one-pot strategy was also compared on a substrate without mesoporous TiO₂ layer as scaffold. This further supports the relevance of the scaffold layer to process the hole transport and the perovskite layer in only one simple step.

Perovskite Solar Cells Involving Poly(tetraphenylbenzidine)s: Investigation of Hole Carrier Mobility, Doping effects, and Photovoltaic Properties

In perovskite solar cells, the most important requirements, besides the active perovskite layer itself, are suitable extraction layers for holes and electrons. Thus, the hole transport layer (HTL) plays a crucial role to obtain high PCEs. This chapter deals with the application of PTPDs as HTLs in CH₃NH₃PbI₃ perovskite solar cells. In particular, the following fundamental questions are addressed in detail: 1) Is there a molecular weight dependence or an optimum molecular weight for charge carrier transport? 2) What is the nature and mechanism of the doping of the PTPD with a Co(III)-complex and what is its effect on charge carrier mobility and the photovoltaic properties? 3) What is the influence of the side chain polarity on charge transport and on solar cell performance in CH₃NH₃PbI₃ devices? To answer these questions, we carried out a study on the charge transport in view of the varied molecular weight distributions, the mechanism of doping and the application in perovskite solar cells involving a series of PTPDs. Therefore, three polymers carrying ethylhexyloxy side chains (**PTPD1-3**) and one carrying hydrophilic oligo ethylene glycol (OEG) side chains (**PTPD4**) were synthesized and investigated. The SCLC method revealed that there is neither a dependence of the hole transport mobility on the molecular weight nor on the polydispersity of the PTPD polymers. Furthermore, nature of the side chains has no effect on the hole transport mobility. Doping of the PTPDs with a Co(III)-complex shows an increase of the charge carrier density in SCLC devices which was further investigated by UV-vis-NIR measurements (Figure 4a). Thus, the addition of a Co(III)-complex leads to typical new absorption bands which could be attributed to radical cation species as confirmed by spectroelectrochemical measurements (Figure 4b).

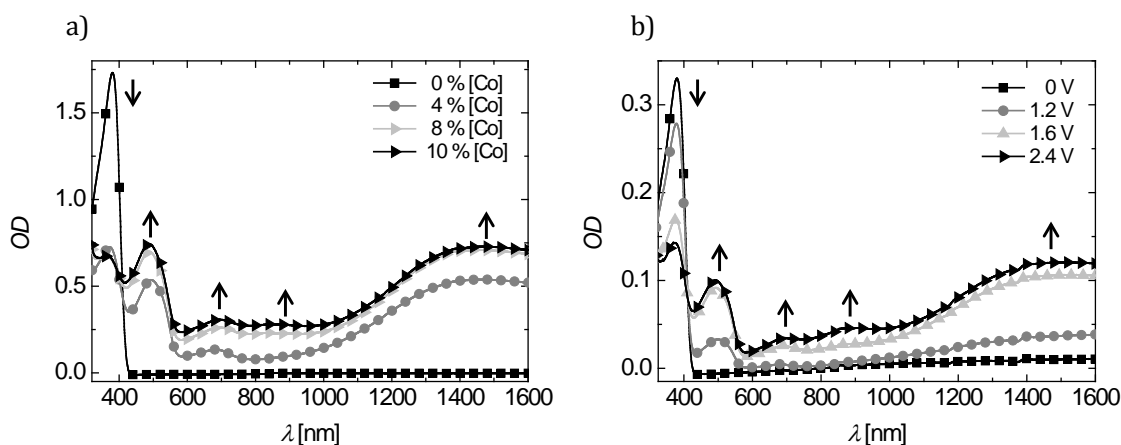


Figure 4. a) UV-vis and b) spectroelectrochemical measurements of **PTPD2**. In both, new absorption bands arise due to oxidation of the polymer.

The influence of the Co(III) doping was further investigated in photovoltaic measurements. Additionally, a conducting Li-salt (lithium bis(trifluoromethanesulfonyl)imide) was added which improved the photovoltaic performance of the devices drastically. In a further experiment we compared the influence of the nature of side chains of the PTPDs on PCE. Here, **PTPD2** with ethylhexyl and **PTPD4** with OEG side chains give a similar PCE. However, there is an influence of the side chains on the hysteresis behavior of the solar cells and on the device stability under illumination. **PTPD4** with OEG side chains shows a less pronounced hysteresis on forward and backward measurement and a higher device stability under illumination probably due to a better interface formation with the rough and polar perovskite surface.

Further, we investigated the effect of storage on the photovoltaic parameters. All the photovoltaic parameters except the fill factor were improved drastically after storage under nitrogen. This is very surprising and it is an unexpected result. Therefore, a comparison of EQE and UV-vis absorption was carried out to understand this improvement. We can attribute the effect of storage to an increased absorption in the long wavelength region. This can be observed in EQE and UV-vis measurements for the stored devices (Figure 5). The reason for this is probably a post-crystallization effect and decreasing defects.

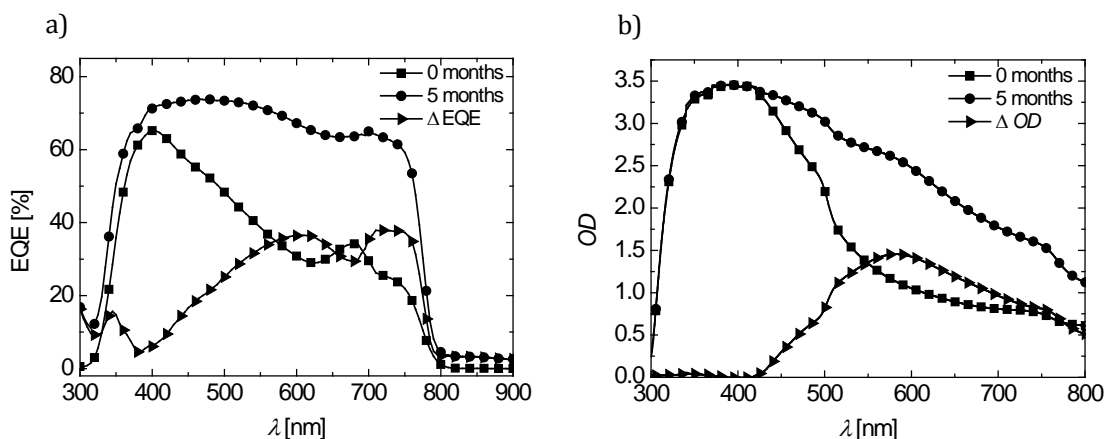


Figure 5. Comparison of freshly prepared devices (squares) and devices stored for 5 months under nitrogen (circles). a) EQE spectra, b) UV-vis spectra.

Undoped and doped Poly(tetraphenylbenzidine) as Sensitive Material for an Impedimetric NO₂ Gas Dosimeter

Conductometric gas dosimeters are an alternative to conventional gas sensors to determine the dose or concentration of toxic and harmful gases. The difference to classical gas sensors is that the total amount of dose of the analyte can be detected directly. This is due to the accumulation of gas molecules which leads to an added change of the electrical properties of the active material. Most important is a selective accumulation of the analyte molecules and a measurable dependence of the change of electrical properties. It is desirable to use organic semiconducting polymers for the application in gas dosimeters because of their advantageous properties of excellent film formation, low temperature operation, and low cost fabrication. But the main challenge is to achieve sensitivities < 10 ppm. We show that PTPDs are suitable materials for the use as active layers in gas dosimeters. The sensing mechanism arises from the good oxidizability of the PTPD with NO₂. In more detail, the interaction with NO₂ leads to the oxidation of PTPD which is similar to a doping effect. Thus, the conductivity increases and the resistivity decreases upon exposure to NO₂. This was measured with impedance spectroscopy. When the PTPD is used in its undoped state, the sensor signal increases during exposure to NO₂. However, in absence of the analyte a certain recovery occurs and the accumulated dose of the analyte cannot be detected and it works as a classical sensor (Figure 6a). To improve the dosimeter behavior of PTPD, we doped the polymer with a Co(III)-complex and added a Li-salt as conducting salt, leading to a drastic improvement of the dosimeter behavior. As depicted in Figure 6b the active

material is now able to accumulate the analyte. Moreover, analyte concentrations < 10 ppm could be detected.

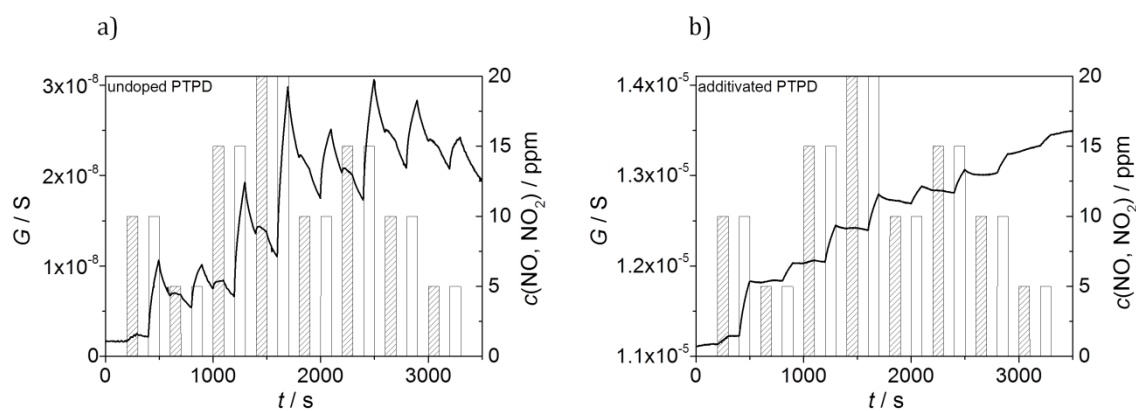


Figure 6. Conductance G (lines) of a) an undoped PTPD film and b) additivated PTPD film during NO and NO₂ dosing over time t . The concentration of NO is represented by the hatched areas, the concentration of NO₂ by the white areas.

Influence of the Excited State Charge-Transfer Character on the Exciton Dissociation in Donor-Acceptor Copolymers

Alternating donor-acceptor copolymers (D-A copolymers) are widely used in the field of bulk heterojunction solar cells in order to lower the optical gap and achieve better light harvesting. Commonly, two strategies are used in the literature to synthesize D-A copolymers. The first strategy is the incorporation of an acceptor unit as a side chain on the donor backbone. For the second strategy donor and acceptor units are linked in an alternating way in the main chain. Here, we correlate the charge transfer (CT) character and the delocalization in these D-A copolymers with the charge carrier mobility and study the charge separation in bilayer solar cells with C₆₀. For this, we compared two novel D-A copolymers to identify the fundamental differences of both strategies. Our D-A systems are based on triphenylamine (TPA) as donor unit. The acceptor moiety in the first D-A copolymer is a dicyanovinyl group attached to the side chain (**P2**). For the second D-A copolymer **P3**, a thieno[3,4-*b*]thiophene carboxylate unit was incorporated in the main chain. The two D-A copolymers were compared with a reference homopolymer (**P1**) without any acceptor unit. Detailed UV-vis absorption studies showed that new bands in the long wavelength region appear by introduction of both acceptor units. Furthermore, **P2** has a limited delocalization and a strong CT-character, whereas in **P3** the new absorption band can be mainly attributed to a π - π^* -transition with considerable delocalization

(Figure 7). These observations are furthermore supported by photoluminescence measurements.

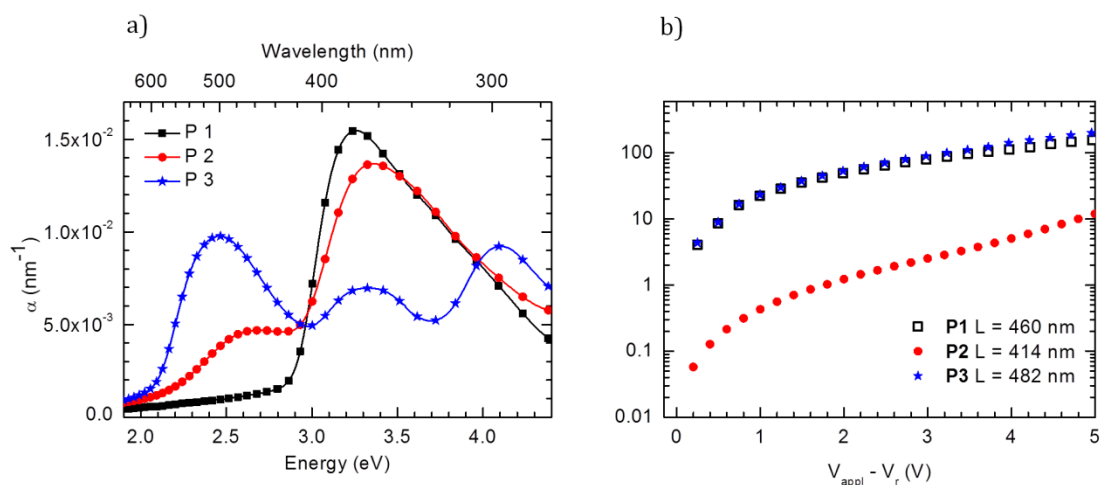


Figure 7. a) Molar extinction coefficient per repeat unit UV-vis absorption spectra of **P1**, **P2**, and **P3** in film obtained from 10 mg mL⁻¹ solutions in chlorobenzene. b) Half-log plot of current density J vs. voltage V of **P1**, **P2**, and **P3** for comparable layer thicknesses.

Cyclic voltammetry measurements revealed that the introduction of the strong electron withdrawing dicyanovinyl acceptor reduces the electron richness and delocalization of the TPA main chain for **P2**. On the other hand, the thieno[3,4-*b*]thiophene carboxylate acceptor incorporated in the main chain (**P3**) does not affect the oxidation potential. The resulting oxidizability is similar to the homopolymer **P1**, which means that the conjugation of the TPA backbone is maintained. This result could be supported by hole transport mobility measurements. Here, it was found that the hole transport mobility of **P2** with dicyanovinyl acceptor in the side chain is strongly reduced in comparison to **P1** and **P3**, which can be attributed to the reduced delocalization in **P2** (Figure 7b).

In order to evaluate the nature of excited states in the two D-A copolymers, field-dependent charge extraction studies in bilayer solar cells with C₆₀ as acceptor were performed. A higher photodissociation at low internal field strength was found for **P3**. In contrast, **P2** shows a poor photodissociation. Thus, the stronger CT-character and more localized hole in **P2** is not beneficial for the charge separation process (Figure 8). Consequently, charge separation occurs more readily when the acceptor is incorporated in the main chain of the D-A copolymer guaranteeing delocalization along the main chain.

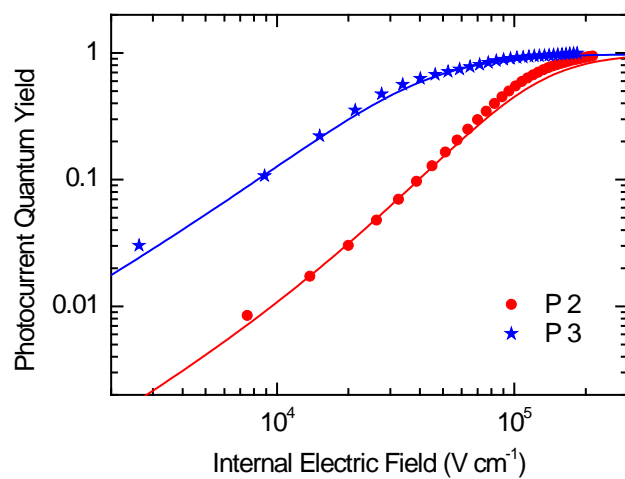


Figure 8. Normalized field-dependent photocurrent quantum yields of copolymer/ C_{60} bilayer devices calculated from the photocurrent under AM 1.5 conditions. The lines indicate fits based on an effective mass model including interfacial dipole effects.

Individual contributions to joint publications

The following section specifies the individual contributions of the authors.

Chapter 5

This work is prepared for submission to *Advanced Materials* under the title:

“In situ crystallization-driven phase separation towards one pot fabrication of Perovskite/Polymer solar cells “

by Katharina Neumann and Mukundan Thelakkat.

I synthesized and characterized the polymer, developed the fabrication method, built the solar cells and performed the full characterization thereof. Furthermore, I wrote the manuscript.

Mukundan Thelakkat supervised the project and corrected the manuscript

Chapter 6

This work is accepted to be published in *RSC Advances*, 2014, DOI: 10.1039/C4RA05564K under the title:

“Perovskite Solar Cells Involving Poly(tetraphenylbenzidine)s: Investigation of Hole Carrier Mobility, Doping effects and Photovoltaic Properties“

by Katharina Neumann and Mukundan Thelakkat.

I synthesized and characterized all polymers, built the solar cells and performed the full characterization thereof. Furthermore, I wrote the manuscript.

Mukundan Thelakkat supervised the project and corrected the manuscript

Chapter 7

This work is submitted to *Applied Physics Letters* under the title:

“Undoped and doped Poly(tetraphenylbenzidine) as Sensitive Material for an Impedimetric NO₂ Gas Dosimeter”

by Isabella Marr, Katharina Neumann, Mukundan Thelakkat, and Ralf Moos.

I synthesized and characterized the polymer, prepared the substrates for the dosimeter measurements, and corrected the manuscript.

Isabella Marr performed all dosimeter measurements and wrote the manuscript.

Ralf Moos and Mukundan Thelakkat supervised the project and corrected the manuscript.

Chapter 8

This work is published in *Journal of Physical Chemistry: C* 2014, 118, 27-36, DOI: 10.1021/jp407014q under the title:

“Influence of the Excited-State Charge-Transfer Character on the Exciton Dissociation in Donor–Acceptor Copolymers“

by Katharina Neumann, Christian Schwarz, Anna Köhler, and Mukundan Thelakkat.

I designed and synthesized all polymers, characterized them in respect of polymer properties and charge transport, and wrote the corresponding part of the manuscript. I corrected the whole manuscript.

Christian Schwarz did the optical measurements and built the bilayer solar cells. He interpreted his experiments, wrote the corresponding part, and corrected the manuscript.

Mukundan Thelakkat and Anna Köhler supervised the project and corrected the manuscript.

Appendix: Chapter 9

This work is published in *Proceedings of SPIE 8477, Organic Photovoltaics XIII*, 2012, 84771H, doi: 10.1117/12.929842 under the title:

„Synthesis and characterization of donor-acceptor copolymers carrying triphenylamine units for photovoltaic applications“

I synthesized and characterized the polymers and wrote the manuscript.

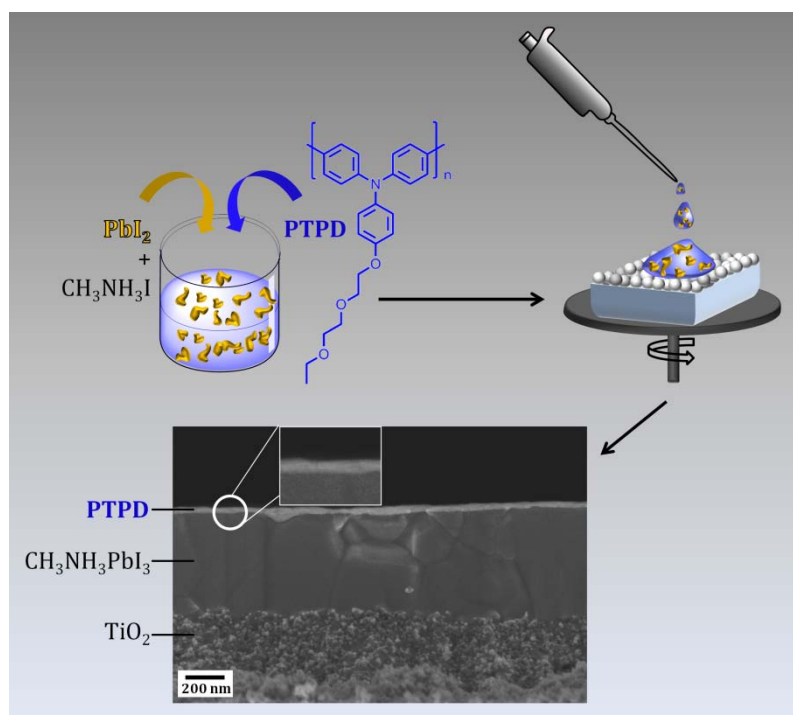
Mukundan Thelakkat supervised the project and corrected the manuscript.

Crystallization-driven phase separation towards one pot fabrication of bilayer perovskite/polymer solar cells

Katharina Neumann, Mukundan Thelakkat*

Department of Macromolecular Chemistry I, Applied Functional Polymers, University of Bayreuth, Universitätsstraße 30, 95440 Bayreuth, Germany

*Email corresponding author: mukundan.thelakkat@uni-bayreuth.de



Prepared for submission to *Advanced Materials*

Abstract

Perovskite solar cells are an emerging research field which underwent an outstanding development towards very high efficiencies. Here we show an elegant and novel approach to create a bilayer of perovskite and polymeric hole conductor from a blend of the precursors for perovskite and the polymer in a one-pot fabrication method. The strategy involves a crystallization driven macrophase separation leading to a desired vertical layered structure. This is realized by using a poly(tetraphenylbenzidine) (PTPD) polymer which is soluble in polar solvents such as γ -butyrolactone and *N*-methylpyrrolidone, in which both PbI_2 and $\text{CH}_3\text{NH}_3\text{I}$ also dissolve. Thus, a homogeneous solution of all the three components could be prepared at elevated temperatures. After solution casting from the precursor solution the crystallization of the perovskite is carried out. During the crystallization process, the blend system phase separates leading to a layered structure of the crystallized perovskite at the bottom and the hole transporting polymer layer on top. The annealing protocol as well as the solar cell preparation and characterization are given. This method is used here for the first time and it is an elegant tool to reduce the processing steps for perovskite solar cells making them even more interesting for the use in large area applications. We obtain large crystals of perovskite with well-defined interfaces as observed in scanning electron microscopy.

Introduction

Finding innovative ways to solve the energy and environmental problems is the main challenge of the 21st century. Currently, the energy supply is achieved by using fossil fuels causing detrimental effects on the environment. In order to use CO_2 neutral processes, the photovoltaic energy conversion contributes in a considerable manner as a renewable energy source. In this regard, very promising hybrid organic-inorganic devices using lead halide perovskite materials as direct band gap semiconductors have been reported recently.^[1-5] High power conversion efficiencies (PCEs) > 15 % were reached. On an average PCE values above 10 % is reproduced in bilayer devices both by sequential solution processing and vapour deposition methods.^[3,6-10] The hybrid perovskite widely used in these studies has the general chemical composition of $\text{CH}_3\text{NH}_3\text{PbX}_3$ ($X = \text{Cl}, \text{Br}, \text{I}$) where the most studied compound is the triiodide or the mixed halide of iodide and chloride. Many device architectures and morphologies have been shown. For instance, mesoporous layers or nanorods of metal oxides such as TiO_2 , ZnO or Al_2O_3 as scaffold were already used at the electron collecting electrode.^[11-13] However, it is also possible to prepare highly efficient perovskite cells in a planar structure. Here, only a hole blocking/electron extracting layer (TiO_2 , ZnO , PCBM) and an electron blocking/hole extracting layer is necessary.^[7,14,15] For hole collection, usually a doped organic hole conductor involving 2,2',7,7'-tetrakis(*N,N*-di-*p*-methoxyphenylamine)-9,9'-spirobifluorene (spiro-MeOTAD) or

poly(triphenylamines) were utilized.^[16] Furthermore, it was shown that perovskites can be produced on flexible substrates indicating a possible use in large area applications.^[10] Since these perovskites are direct band gap semiconductor materials capable of charge dissociation, the real role of both scaffolds as well as hole conductor layers are yet to be elucidated. Moreover, the lead perovskites exhibit very high carrier diffusion length in the range of 500 to 1000 nm (mixed halides favoring high diffusion length) enabling the fabrication of p-i-n solar cells containing thick absorbant layers of perovskite sandwiched between p-type and n-type charge collecting electrodes.^[13,17]

One of the major challenges in the fabrication of hybrid perovskite solar cells is how to decrease the strong scattering of the performance, which involves large variations. Not only the processing conditions are crucial, but also the above mentioned device architectures can influence the performance resulting in a broad range of efficiencies reached in different research groups and laboratories. Thus, highly reproducible and simple preparation methods are very desirable having in mind a possible application in large area roll-to-roll fabrication processes. To fulfill this target, several challenges have to be overcome. The main issue is the creation of well-defined, big perovskite crystals with less grain boundaries and a smooth surface on a large area scale.^[18] At present, most of the processing techniques result in rough surface area which in turn demands very thick hole transporting upper layers which limits the performance. To improve the performance of these devices a very thin hole collecting upper layer is necessary. Another issue is the insufficient surface coverage limiting large area fabrication. Therefore, innovative fabrication methods are necessary to overcome both the above mentioned issues.

We developed an elegant approach based on a controlled crystallization of the perovskite within a polymer matrix as shown in Figure 1. Our idea was that if it is possible that this matrix is a hole conductor having suitable thermal and electronic properties, there will be a good chance to realize the deposition of the active perovskite and the hole blocking layer in one single step. In this paper, we address exactly this question and report an in situ one pot fabrication of a well-defined bilayer device structure starting from a blend of poly(tetraphenylbenzidine) (PTPD) carrying polar substituents and the precursors PbI_2 and $\text{CH}_3\text{NH}_3\text{I}$. Our strategy toward the one-pot fabrication is based on the crystallization driven vertical phase separation of the perovskite and PTPD.

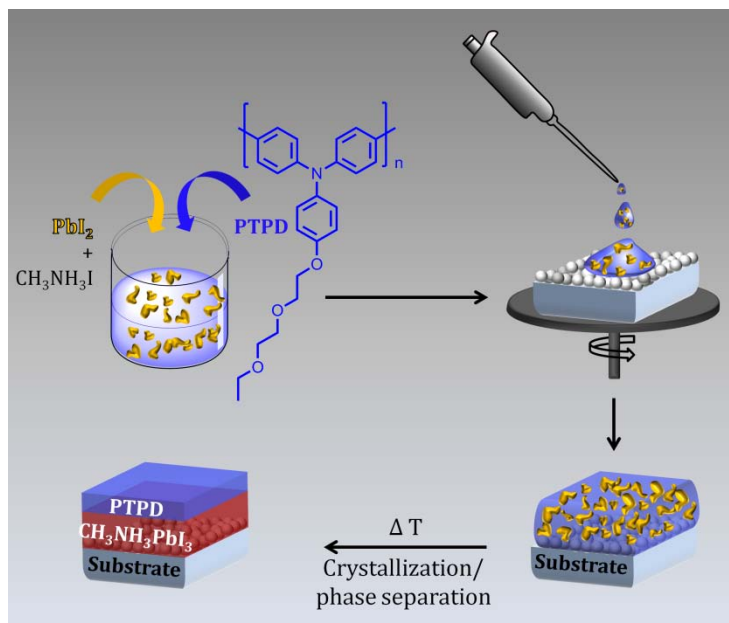


Figure 1. Schematic illustration of the crystallization driven phase separation towards the bilayer structure of perovskite and hole transport layer in a one-pot fabrication. The blend solution containing PTPD, PbI_2 and $\text{CH}_3\text{NH}_3\text{I}$ was spin-coated and thermally annealed during which the crystallization of the perovskite occurs and the desired bilayer (perovskite/PTPD) structure is formed.

The most important task to reach this goal is to develop a suitable hole conducting polymer. Since perovskites are prepared from the precursors PbI_2 and $\text{CH}_3\text{NH}_3\text{I}$, both these precursors and the hole conductor matrix should be highly soluble and miscible in a single solvent system. This is a prerequisite for such an in situ approach of multi-component fabrication. We achieved this by designing a PTPD with polar ethylene glycol side chains. The polar substituents guarantee sufficient solubility and miscibility with the perovskite precursors in suitable solvents such as γ -butyrolactone. Furthermore, the good hole transport and electron blocking behavior of PTPDs, their low ionization potential and the amorphous character makes them optimal candidates for the application in solar cells.^[10,19] Another advantage is the amorphous nature of PTPD leading to excellent film forming behavior together with a heterogeneous mixture of the precursor solution. Additionally, the non-polar nature of the polymer backbone can lead to phase separation of the mixture and accumulation of the polymer to the perovskite/air interface. The glass transition temperature (T_g) of the PTPD is 124 °C. This is highly suitable for low-temperature processing (< 150 °C) and it is high enough to guarantee good thermal and long-term morphological stability of the devices.

In detail, for the fabrication of the devices both the perovskite precursors PbI_2 and $\text{CH}_3\text{NH}_3\text{I}$ (equimolar amounts) as well as PTPD are dissolved in γ -butyrolactone. The composition of precursors to polymers is 1:1 wt.%. After preparation of the wet film by spin-coating, the

perovskite crystallizes at 130 °C. The smartness of this concept is the simultaneous controlled crystallization of perovskite in a polymer matrix leading to very big perovskite crystals (50-100 μm) and an intimate interface with the overstanding polymeric hole conductor. The thickness of this polymer layer can be optimized by varying the composition of the blend and very thin overstanding layers were thus obtained. The relative high speed of crystallization of perovskite and its infiltration into the mesoporous layer squeezes the polymer towards the air interface resulting in the desired bilayer structure. In the following, we present the preparation and characterization of devices in detail.

Experimental part

Materials: The synthesis of PTPD ($M_n = 11000 \text{ g mol}^{-1}$, PDI = 1.99) via Yamamoto polycondensation was published elsewhere. A detailed investigation on charge transport and the use of this PTPD as hole transport layer for conventional perovskite solar cells is also reported.^[20]

Device preparation: Structured fluorine-doped tin oxide (FTO, stripes with width of 3 mm and 4 mm) was coated with a compact TiO_2 layer (500 nm) by spray-pyrolysis at 450 °C. The mesoporous TiO_2 layer was deposited by doctor-blading and subsequent annealing at 500 °C. All following preparation steps were carried out in a glovebox under nitrogen atmosphere. PbI_2 was purchased from Aldrich, $\text{CH}_3\text{NH}_3\text{PbI}_3$ was synthesized according to the literature.^[13] 578.5 mg PbI_2 and 199.5 mg $\text{CH}_3\text{NH}_3\text{PbI}_3$ were dissolved in γ -butyrolactone (GBL) at 75 °C and 1 wt.% PTPD was dissolved in GBL at 135 °C. The solutions were mixed together (PTPD to precursors 1:1 for mesoporous devices and 2:1 for planar devices) prior to spin-coating at 800 rpm for 30 s. The devices were annealed at 135 °C for 10 min on a hot plate. Gold was thermally evaporated in a vacuum deposition chamber to obtain devices having 9 or 16 mm^2 areas. No salt or other additives were used for the hole conductor to avoid inclusion of salt in the perovskite film.

Characterization: The devices were measured under nitrogen by a Keithley 6517 Source-Measure unit under AM 1.5 G conditions (Solar simulator-A grade from Newport). The intensity of the light was calibrated with a standard Si-reference cell from the Fraunhofer Institute for Solar Energy Systems (ISE), Freiburg, as 100 mW cm^2 . The EQE values were measured under nitrogen using a Bentham PVE300 under short-circuit conditions after illuminating the devices with monochromatic light from a Xenon lamp passing through a Bentham TMc300 monochromator. UV-vis measurements of the devices were carried out on a Hitachi U-3000 two-beam-photometer. For the SEM images all samples were sputtered with platinum (2.0 nm) in a

Cressington sputter coater 208HR. The SEM micrographs were recorded on a Zeiss ULTRA plus FESEM (Zeiss, Jena, Germany).

Results and discussion

It is known in the literature that perovskites easily crystallize in the pores of mesoporous TiO_2 .^[13] In order to benefit from this property for the crystallization driven phase separation of our perovskite/PTPD solution, we used the electron conducting mesoporous TiO_2 layer as scaffold. In a control experiment, the in situ fabrication was also tested on a planar device without TiO_2 scaffold. Figure 2 illustrates the two different setups.

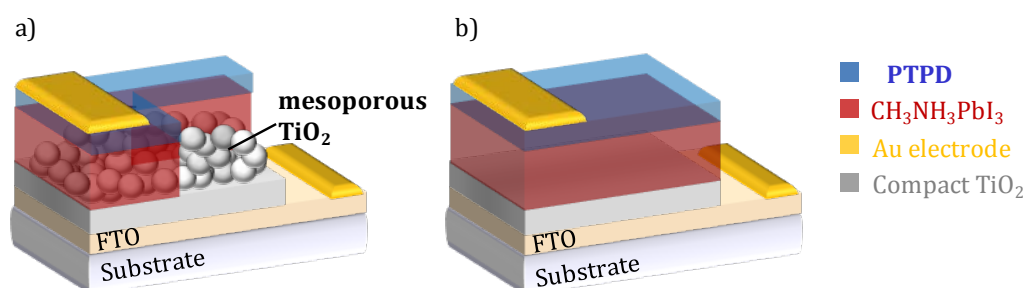


Figure 2. Schematic setup of the two devices resulting from the in situ phase separation of perovskite and PTPD. a) Device with additional mesoporous TiO_2 as electron conductor and scaffold. b) Planar device with $\text{CH}_3\text{NH}_3\text{PbI}_3$ perovskite layer directly on top of compact TiO_2 . PTPD acts as hole conductor.

First, we will address the device preparation on substrates with mesoporous TiO_2 as scaffold. For this, the $\text{CH}_3\text{NH}_3\text{I}/\text{PbI}_2/\text{PTPD}$ solution was spin-coated on top of the scaffold and annealed at $135\text{ }^\circ\text{C}$ for 10 min in an optimized annealing program to form the desired device morphology. In order to investigate the structure of the cell in detail, scanning electron microscopy (SEM) measurements were carried out (see Figure 3a)). The SEM image reveals the layered device structure (perovskite/PTPD) formed in one preparation step. A uniform and monolithic $\text{CH}_3\text{NH}_3\text{PbI}_3$ active layer on top of the mesoporous TiO_2 which is infiltrated with $\text{CH}_3\text{NH}_3\text{PbI}_3$ crystals is clearly visible. Due to the crystallization driven phase separation, the PTPD forms a thin top layer, as desired for an efficient device. Thus, the PTPD was successfully expelled by crystallization of the perovskite. The corresponding top-view in Figure 3b) shows large perovskite crystals ($\sim 75\text{ }\mu\text{m}$ in diameter) over a broad range in addition to areas with smaller crystals on top of the mesoporous TiO_2 (see also supporting information Figure S1 and S2). A long range smooth perovskite/PTPD interface is also clearly visible.

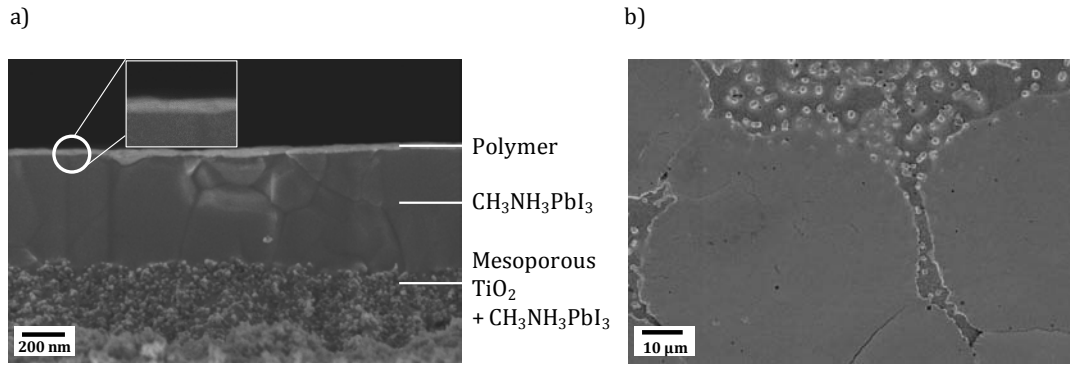


Figure 3. a) Cross-sectional SEM image of a device with perovskite/PTPD layer prepared from precursor solution (PTPD + PbI₂ + CH₃NH₃I) by spin-coating on mesoporous TiO₂. Annealing was done at 135 °C for 10 min. b) Corresponding top-view.

The J - V -characteristic of the above shown device with the best performance under illumination and in dark is given in Figure 4. A photovoltaic performance of $\sim 5\%$ PCE was achieved with a short circuit current density (J_{sc}) of 12.04 mA cm⁻², a open circuit voltage (V_{oc}) of 667 mV, and a fill factor (FF) of 0.59. The average value for four cells was 3.80 %. The limiting factor of the device performance is the perovskite coverage of the surface (see supporting information Figure S2) which can be further optimized by tuning the processing conditions (spin-coating speed, heating and cooling times). Compared to published data, these devices exhibit low V_{oc} . This can be due to the fact that we have not used highly conducting PTPD (e. g. no doping or use of conducting Li-salt), which is necessary for extracting out the low energy electrons at the interface. The corresponding external quantum efficiency (EQE) and UV-vis spectra of the devices will be discussed later.

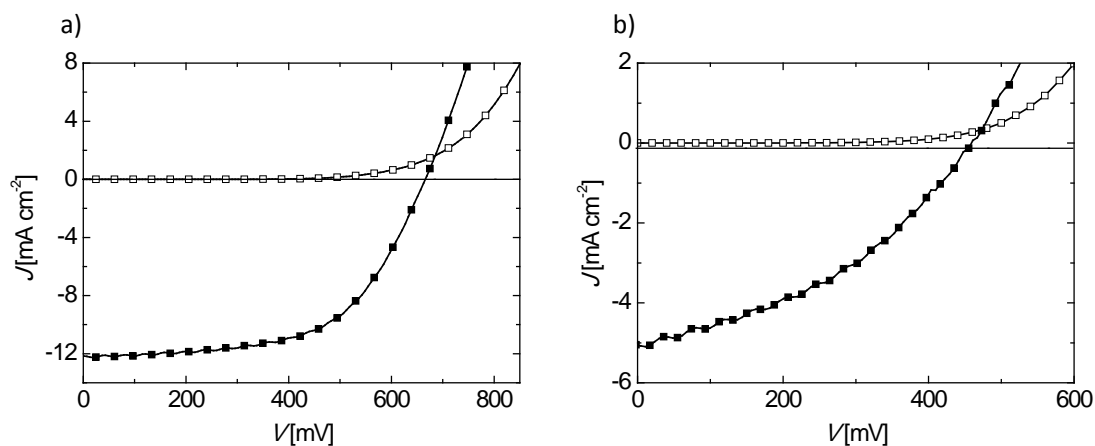


Figure 4. *J-V*-characteristics of the best devices with perovskite/PTPD layer prepared from precursor solution (PTPD + PbI_2 + $\text{CH}_3\text{NH}_3\text{I}$) by spin-coating on a substrate a) with and b) without mesoporous TiO_2 . Annealing was carried out at 135°C for 10 min. The measurement was carried out in dark (empty squares) and at a simulated AM1.5G solar irradiation of 100 mW cm^{-2} (filled squares) under nitrogen.

Now that the proof of principle was shown for devices with a TiO_2 scaffold, we also prepared planar devices as control experiment. Here, only a hole blocking, compact TiO_2 layer is used which further simplifies the processing due to the reduction of the preparation steps. The perovskite/PTPD precursor solution was spin-coated on top of the compact TiO_2 layer and annealed at 135°C to induce the crystallization and phase separation. Figure 5 shows the corresponding SEM images (see supporting information Figure S3 for an image with broader area). Similar to the system with TiO_2 scaffold, the two layers consisting of perovskite and PTPD are formed spontaneously due to phase separation.

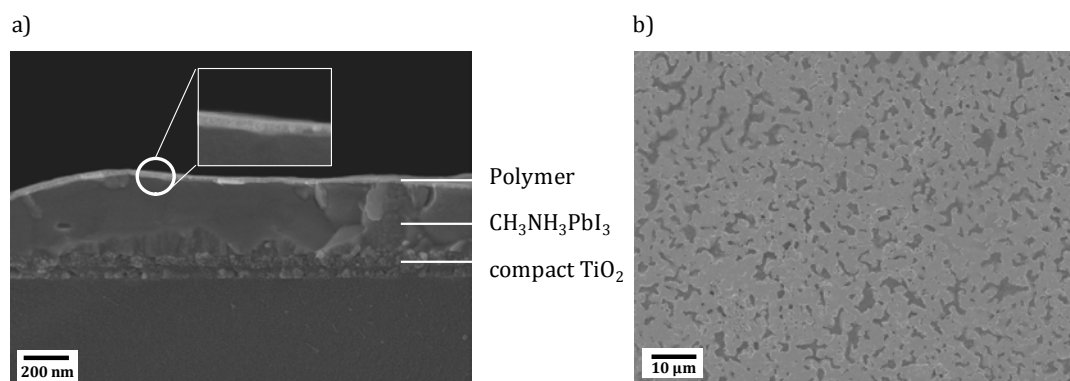


Figure 5. a) Cross-sectional SEM image of a device with with perovskite/PTPD layer prepared from the precursor solution (PTPD + PbI_2 + $\text{CH}_3\text{NH}_3\text{I}$) by spin-coating on compact TiO_2 . Annealing was done at 130°C for 15 min. b) Corresponding top-view SEM image.

On comparison of the top-view of the devices with and without the mesoporous TiO₂ (Figure 3b)), the structure formed on planar TiO₂ is much different as depicted in Figure 5 b). Here, small perovskite crystals with lot of spacing or less coverage is observed. Evidently, this causes a lower FF and even lower V_{OC} resulting in a decreased performance for the planar device.

Table 1 gives a comparison of the devices (best and average values) with and without mesoporous TiO₂ scaffold. Obviously, the device with mesoporous TiO₂ gives a much better photovoltaic performance resulting from higher J_{SC} , V_{OC} , FF, and PCE. Additionally, the series (R_S) and shunt resistances (R_{SH}) of the cells were determined by evaluating the slope of the J - V curve at V_{OC} and J_{SC} , where the inverse of the slopes give the specific resistances in $\Omega \text{ cm}^{-2}$.^[21] The series resistance R_S increases drastically for the planar devices accompanied by a decrease of the R_{SH} , which is in accordance with the low FF.

Table 1. Comparison of photovoltaic parameters of devices with and without mesoporous TiO₂. The parameters for the best devices and the average values for four cells are given. For the best cells the series and shunt resistances were calculated. The integrated photocurrent density was calculated from EQE .

	J_{SC} (mA cm ⁻²)	V_{OC} (mV)	FF	PCE (%)	R_S ($\Omega \text{ cm}^2$)	R_{SH} ($\Omega \text{ cm}^2$)	Integrated J_{SC} (EQE) (mA cm ⁻²)
Mesoporous TiO₂							
Best value	12.04	669	0.59	4.78	12	791	13.84
Average value	10.29	648	0.57	3.80			
RMS Deviation	2.83	17	0.03	1.01			
Planar							
Best value	5.05	461	0.39	0.91	41	227	9.02
Average value	4.19	461	0.37	0.72			
RMS Deviation	0.61	31	0.03	0.13			

Figure 6a) shows the *EQE* measurements for both devices. The *EQE*-value for the device with mesoporous TiO_2 is about 55 to 62 % for the whole absorption range from 400 to 750 nm. For the same wavelength range the planar device exhibits an *EQE*-value of about 38 % which is resembled by the lower J_{SC} in the *J-V*-measurement. The integrated photocurrent calculated from the *EQE* are 13.84 mA cm^{-2} and 9.02 mA cm^{-2} for devices with and without mesoporous TiO_2 , respectively. Additionally, the UV-vis spectra in Figure 6b) confirm this, since a very strong difference in the optical density of the devices with and without mesoporous TiO_2 is found. Thus, for a better solar cell performance, a higher surface coverage and a higher V_{OC} are needed, which can be obtained by further optimization of the fabrication process or improvement of the conductivity of the hole transport layer by adding Li-salt to the precursor solution. It has to be mentioned that the thickness of the $\text{CH}_3\text{NH}_3\text{PbI}_3$ layers were around 540 nm and 300 nm for devices with and without mesoporous TiO_2 , respectively.

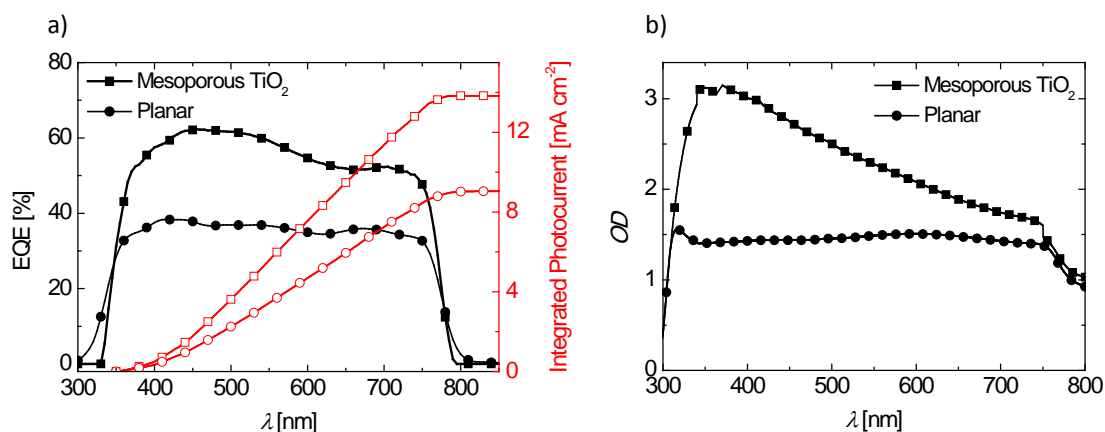


Figure 6. Comparison of the devices with mesoporous TiO_2 (squares) and planar devices (cycles). a) *EQE*-spectra of the devices measured under nitrogen and corresponding integrated photocurrent. b) Corresponding UV-vis spectra.

Conclusion

In conclusion, we demonstrated an elegant one-pot fabrication of $\text{CH}_3\text{NH}_3\text{PbI}_3$ perovskite solar cells resulting in layered structures of polymeric hole conductor and perovskite. In order to achieve this, we synthesized a hole conducting polymer which combines good hole transport properties, solubility in polar solvents such as γ -butyrolactone and *N*-methylpyrrolidone and miscibility with the perovskite precursors. The driving-force towards the desired layered structure is a crystallization driven phase separation of the perovskite and the polymer. We showed that our strategy works well when a mesoporous TiO_2 scaffold is used as underlying layer. The one-pot strategy was also tested in planar devices to understand the role of the

scaffold, which clearly demonstrates the importance of the scaffold layer for this approach. This strategy is very promising and with further optimization using additives it can be extended to large area fabrication.

Acknowledgement

Financial support from the Deutsche Forschungsgemeinschaft (Graduate School GRK 1640) and “Solar Technologies Go Hybrid“, an initiative of the Free State of Bavaria (Bayerisches Staatsministerium für Wissenschaft, Forschung und Kunst) is kindly acknowledged and KN thanks the Universität Bayern e.V. for the financial support in form of a scholarship of the Bayerische Graduiertenförderung and the Elitenetzwerk Bayern (ENB). We thank Martina Heider for the SEM measurements.

References

- [1] A. Kojima, K. Teshima, Y. Shirai, T. Miyasaka, *J. Am. Chem. Soc.* 2009, *131*, 6050.
- [2] H. J. Snaith, *J. Phys. Chem. Lett.* 2013, *4*, 3623.
- [3] H.-S. Kim, C.-R. Lee, J.-H. Im, K.-B. Lee, T. Moehl, A. Marchioro, S.-J. Moon, R. Humphry-Baker, J.-H. Yum, J. E. Moser, M. Grätzel, N.-G. Park, *Sci. Rep.* 2012, *2*.
- [4] S. Kazim, M. K. Nazeeruddin, M. Grätzel, S. Ahmad, *Angew. Chem. Int. Ed.* 2014, *53*, 2812.
- [5] National Renewable Energy Laboratory 2014,
http://www.nrel.gov/ncpv/images/efficiency_chart.jpg.
- [6] J. Burschka, N. Pellet, S.-J. Moon, R. Humphry-Baker, P. Gao, M. K. Nazeeruddin, M. Grätzel, *Nature* 2013, *499*, 316.
- [7] M. Liu, M. B. Johnston, H. J. Snaith, *Nature* 2013, *501*, 395.
- [8] Q. Chen, H. Zhou, Z. Hong, S. Luo, H.-S. Duan, H.-H. Wang, Y. Liu, G. Li, Y. Yang, *J. Am. Chem. Soc.* 2014, *136*, 622.
- [9] D. Liu, T. L. Kelly, *Nature Photon* 2013, *8*, 133.
- [10] C. Roldán-Carmona, O. Malinkiewicz, A. Soriano, G. Mínguez Espallargas, A. Garcia, P. Reinecke, T. Kroyer, M. I. Dar, M. K. Nazeeruddin, H. J. Bolink, *Energy Environ. Sci.* 2014, *7*, 994.

- [11] H.-S. Kim, J.-W. Lee, N. Yantara, P. P. Boix, S. A. Kulkarni, S. Mhaisalkar, M. Grätzel, N.-G. Park, *Nano Lett.* 2013, *13*, 2412.
- [12] D. Bi, G. Boschloo, S. Schwarzmüller, L. Yang, E. M. J. Johansson, A. Hagfeldt, *Nanoscale* 2013, *5*, 11686.
- [13] M. M. Lee, J. Teuscher, T. Miyasaka, T. N. Murakami, H. J. Snaith, *Science* 2012, *338*, 643.
- [14] G. E. Eperon, V. M. Burlakov, P. Docampo, A. Goriely, H. J. Snaith, *Adv. Funct. Mater.* 2013, *24*, 154.
- [15] S. Sun, T. Salim, N. Mathews, M. Duchamp, C. Boothroyd, G. Xing, T. C. Sum, Y. M. Lam, *Energy Environ. Sci.* 2013, *7*, 399.
- [16] J. H. Noh, S. H. Im, J. H. Heo, T. N. Mandal, S. I. Seok, *Nano Lett.* 2013, *13*, 1769.
- [17] E. Edri, S. Kirmayer, A. Henning, S. Mukhopadhyay, K. Gartsman, Y. Rosenwaks, G. Hodes, D. Cahen, *Nano Lett.* 2014, *14*, 1004.
- [18] M. Saliba, K. W. Tan, H. Sai, D. T. Moore, T. Scott, W. Zhang, L. A. Estroff, U. Wiesner, H. J. Snaith, *J. Phys. Chem. C* 2014, Article ASAP.
- [19] M. Thelakkat, *Macromolecular Materials and Engineering* 2002, *287*, 442.
- [20] Katharina Neumann, Mukundan Thelakkat, submitted to *RSC Advance* 2014.
- [21] J. D. Servaites, M. A. Ratner, T. J. Marks, *Energy Environ. Sci.* 2011, *4*, 4410.

Supporting Information to

Crystallization-driven phase separation towards one pot fabrication of bilayer perovskite/polymer solar cells

Katharina Neumann, Mukundan Thelakkat*

Additional SEM images

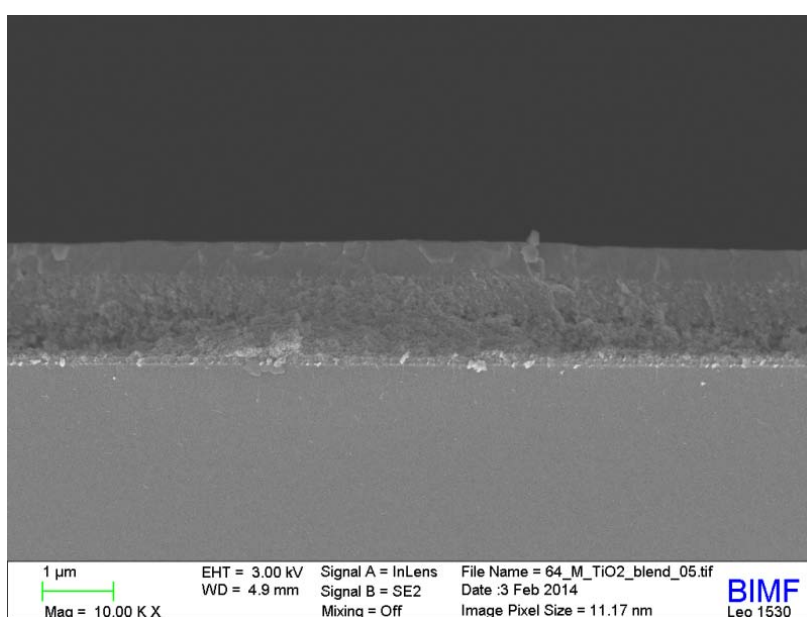


Figure S1. Overview cross sectional SEM image of a device with perovskite/PTPD layer prepared from precursor solution (PTPD + PbI_2 + $\text{CH}_3\text{NH}_3\text{I}$) by spin-coating on mesoporous TiO_2 . A uniform perovskite layer is formed over a wide area.

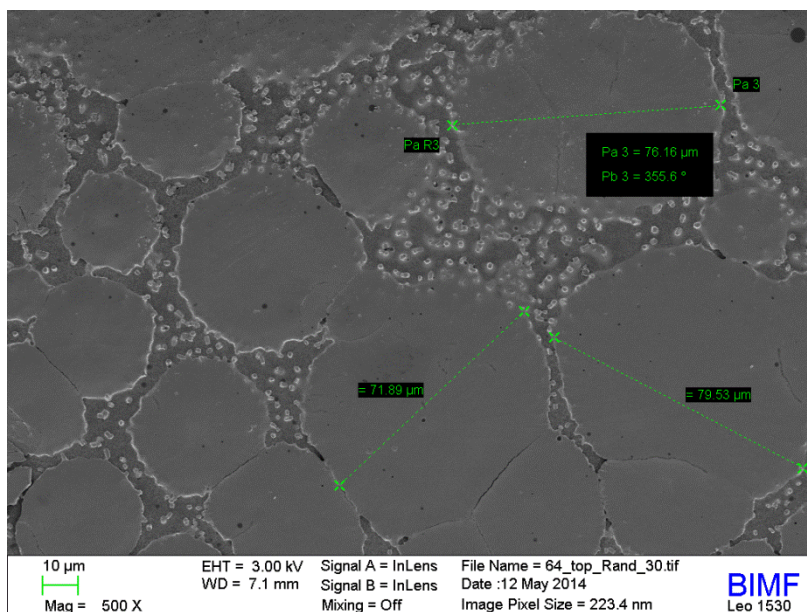


Figure S2. Top-view SEM image of a device with perovskite/PTPD layer prepared from precursor solution (PTPD + PbI_2 + $\text{CH}_3\text{NH}_3\text{I}$) by spin-coating on mesoporous TiO_2 . The surface is covered with large perovskite crystals (around 75 μm in diameter).

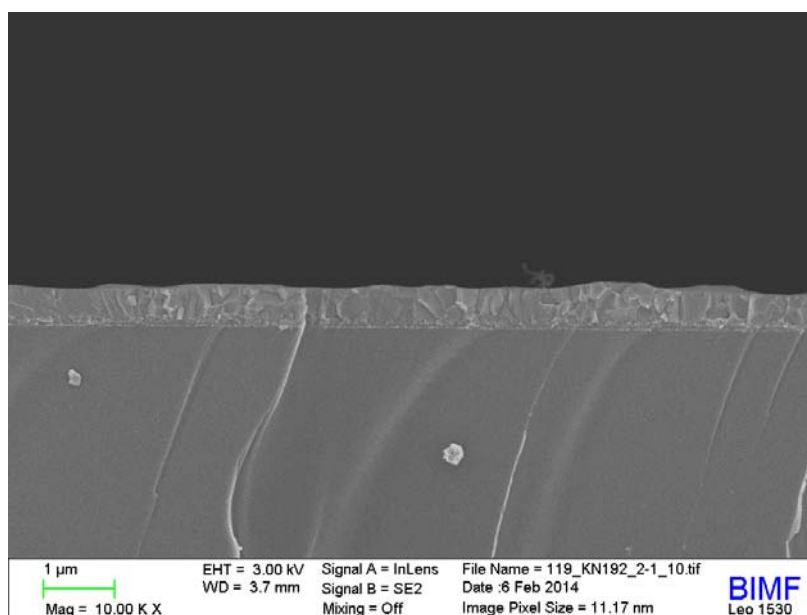


Figure S3. Overview cross sectional SEM image of a device with perovskite/PTPD layer prepared from precursor solution (PTPD + PbI_2 + $\text{CH}_3\text{NH}_3\text{I}$) by spin-coating on a planar substrate.

ABSTRACT

Perovskite solar cells in combination with organic hole transport materials have attracted attention due to their high power conversion efficiencies. Now that these high efficiencies were reached, it is important to address fundamental questions regarding the requirements of the material properties. Here, we present a detailed study on important properties of the hole transport material such as the influence of the molecular weight, the doping effects on charge carrier mobility and the polarity of the material. A series of poly(tetraphenylbenzidines) (PTPDs) differing in their properties was synthesized via Yamamoto polycondensation. Using space charge limited current (SCLC) measurements, we find that the hole transport mobility is independent of the investigated molecular weight and polarity of the side chains. Doping of the PTPDs with a Co(III)-complex reveals that the charge carrier density increases through an oxidation process. Further, the solar cell performance improves upon doping. After storing the devices, the power conversion efficiencies of the solar cells drastically increase due to improved absorption leading to improved EQE. For example, the best performing cell exhibited a power conversion efficiency of 7.69 %. Additionally, the PTPD carrying polar substituents leads to a less pronounced hysteresis effect and a higher stability under illumination compared to the polymer carrying hydrophobic side chains.

1. Introduction

Considerable effort has been made in the field of perovskite solar cells in the last year. Record power conversion efficiencies (PCE) up to 15 % were already reached, for example by a solution based two-step method.¹ The perovskite used as light harvesting material is an inorganic-organic hybrid with the structure $\text{CH}_3\text{NH}_3\text{PbX}_3$ (X = I, Cl, Br). Since the first report of an electrolyte-based perovskite sensitized solar cell in 2009, where 3.8 % PCE was reached, impressive improvements of the processing and the design of solid-state perovskite solar cells have been achieved.² In the previously mentioned reports mesostructured composites, involving titanium dioxide (TiO_2) as electron conductor, were used. Moreover, vertically aligned zinc oxide (ZnO) nanorod arrays were also applied.³ However, it is also possible to prepare the perovskite devices only with the perovskite layer sandwiched between a hole blocking and a hole transport layer. This was shown to be highly efficient (PCE = 15.4 %) for devices prepared by vapour deposition and very recently for fully solution processed devices with TiO_2 blocking layers.⁴ Further on, a ZnO blocking layer was shown to be a promising alternative for low-temperature preparation of perovskite solar cells.⁵ Most of the achievements were realized by optimizing the crystallinity of the perovskite layer itself and by a suitable selection of respective hole blocking and hole transport materials.

In the majority of the cases, 2,2',7,7'-tetrakis(*N,N*-di-*p*-methoxyphenylamine)-9,9'-spirobifluorene (spiro-MeOTAD) is used as the hole transport layer (HTL) due to its good performance in solid-state dye-sensitized devices based on its processability from solution and suitable HOMO (highest occupied molecular orbital) level. Since spiro-MeOTAD suffers from low conductivity in its pristine form, commonly chemical doping is used to generate additional charge carriers. This is a well-known method to enhance the conductivity of organic semiconductors.⁶ Burschka et al. reported a Co(III)-complex as a chemical p-dopant which was successfully used for spiro-MeOTAD in perovskite solar cells.^{1,7} Other suitable organic HTLs for the use in perovskite solar cells are e. g. 2,5-bis(4,4'-bis(methoxyphenyl)aminophen-4''-yl)-3,4-ethylenedioxy-thiophene, poly(3-hexylthiophene) (P3HT) or low band gap polymers such as poly[*N*-9-hepta-decanyl-2,7-carbazole-*alt*-3,6-bis-(thiophen-5-yl)-2,5-dioctyl-2,5-dihydropyrrolo[3,4-]pyrrole-1,4-dione].⁸ In a recent study, Heo *et al.* compared P3HT, poly-[2,1,3-benzothiadiazole-4,7-diyl[4,4-bis(2-ethylhexyl)-4*H*-cyclopenta[2,1-b:3,4-b]dithiophene-2,6-diyl]] (PCPDTBT), (poly-[[9-(1-octylnonyl)-9*H*-carbazole-2,7-diyl]-2,5-thiophenediyl-2,1,3-benzothiadiazole-4,7-diyl-2,5-thiophenediyl]) (PCDTBT) and poly(triarylamine) (PTAA) as HTLs in devices with a nanocomposite of mesoporous (mp)-TiO₂ and with CH₃NH₃PbI₃ perovskite as active layer.⁹ They found that PTAA was the most promising hole conductor polymer due to a high fill factor (FF) and a high open circuit voltage (V_{oc}) with a maximum PCE of 12 %. In the so far reported studies of PTAA as HTL, the commercially available PTAA with pendant methyl groups was used.¹⁰ In this work, the fundamental study concerns with the basic requirements to be fulfilled by such a polymer. For main-chain semicrystalline semiconductor polymers such as P3HT, the charge carrier mobility is dependent on the molecular weight. Initially it increases with molecular weight and after reaching a maximum, decreases for higher molecular weights.¹¹ On the other hand, side-chain triphenylamines (TPAs) did not show a dependence of the mobility on the molecular weight due to their amorphous character.¹² In our case, we are dealing with a material which is a main-chain poly(tetraphenylbenzidine) (PTPD) polymer with amorphous character. Therefore, we address the following questions: 1) Is there a molecular weight dependence and an optimum molecular weight for charge carrier transport? 2) What is the nature and mechanism of the doping of the PTPD with a Co(III)-complex and what is its effect on charge carrier mobility and the photovoltaic properties? 3) What is the influence of the polarity of the polymer on charge transport and on solar cell performance in CH₃NH₃PbI₃ devices? In this respect, it is important to note that the charge carrier mobility of side-chain poly(perylene bisimide)s changes with the polarity of the substituent considerably.¹³ Another question of relevance is the effect of storage on solar cell parameters or the life-time in general. In this report, we address these questions using a series of PTPD as hole transport material. The hole transport properties in view of the varied molecular weight distributions, the mechanism of

Table 1 gives the number average molecular weights (M_n), the weight average molecular weights (M_w) and the polydispersity indices (PDI) obtained from size exclusion chromatography (SEC) measurements in THF calibrated with polystyrene standards. For the hydrophobic polymers, the M_n increases from 10330 g mol⁻¹ to 37060 g mol⁻¹ for **PTPD1** to **PTPD3**. The hydrophilic **PTPD4** has a M_n of 11000 g mol⁻¹. In differential scanning calorimetry (DSC) measurements the glass transition temperature (T_g) values for **PTPD1**, **PTPD2**, and **PTPD3** were determined to be 147, 152 and, 157 °C, respectively. **PTPD4** shows a lower T_g of 124 °C due to the higher flexibility of the oligo ethylene glycol side chains. In cyclic voltammetry measurements in dichloromethane (DCM) a similar HOMO level of -5.30 eV for all the polymers were found. The HOMO values were calculated from their first oxidation potentials by taking the absolute value of the ferrocene/ferrocenium couple to be -5.16 eV.¹⁵ The details of redox potentials, calculation of HOMO levels, SEC and DSC curves are given in the supporting information (**Table S1, Figures S1, S2**).

Table 1. Molecular weights M_n , M_w and PDI of **PTPD1-4**. Glass transition temperatures T_g were measured using DSC and hole transport mobilities μ_h were calculated from SCLC measurements.

Polymer	Side chain	M_n ^{a)} [g/mol]	M_w ^{a)} [g/mol]	PDI ^{a)}	T_g ^{b)} [°C]	μ_h [cm ² V ⁻¹ s ⁻¹]
PTPD1 ^{c)}	alkyl	10330	15770	1.52	147	$1.6 \cdot 10^{-4}$
PTPD2	alkyl	12920	29500	2.28	152	$4.7 \cdot 10^{-4}$
PTPD3	alkyl	37060	147540	3.98	157	$1.1 \cdot 10^{-4}$
PTPD4	OEG	11000	21900	1.99	124	$1.9 \cdot 10^{-4}$

^{a)}Measured by SEC in THF at room temperature; ^{b)} T_g measured from 20-280 °C, 40 K min⁻¹ under nitrogen;

^{c)}Detailed characterization can be found in Ref.¹⁴; OEG: oligo ethylene glycol

2.2. Investigation of the hole transport mobility

In the following, we investigate in detail the hole transport mobility of the polymers by SCLC measurements. This method allows us to compare the bulk charge transport behavior of the polymers with respect to different molecular weights and PDIs. For the SCLC hole-only diode

devices, a poly(3,4-ethylenedioxythiophene):poly(styrenesulfonate) (PEDOT:PSS) coated indium tin oxide (ITO) substrate was used to enable hole-injection. The polymer films with different layer thicknesses were prepared by doctor blading. Afterwards, gold was evaporated as the top electrode which preferentially allows for hole collection and hinders electron injection. Due to this setup and the suitable energy levels of the selected electrodes, the hole current in the SCLC regime should be limited only by the charge carrier mobility (μ_h) of the polymer and it varies with V^2 and L^{-3} , where V is the applied voltage and L is the layer thickness according to equation (1). In the current density J vs. V plots, one can differentiate between two regimes, the ohmic regime at very low voltages and the SCLC regime at higher voltages. In the ohmic regime, the current increases linearly with the voltage. Further increase of the voltage leads to the trap-limited SCLC regime where the current shows a quadratic dependence. Thus, the Mott-Gurney equation (1) was used to calculate μ_h only in the SCLC regime.¹⁶

$$J = \frac{9}{8} \varepsilon \varepsilon_0 \mu_h \frac{V^2}{L^3} \quad \text{Equation (1)}$$

The SCLC behavior was further verified by measuring three layer thicknesses. The fits according to the relation $J \sim V^2 L^{-3}$ are given in the supporting information (**Figure S4**). All the plots exhibit the inverse cubic dependence on the layer thickness. Since we calculated the μ_h values at $V > 1$ V, we also verified the dependence of the μ_h on voltage by taking into account the field dependence factor using the Murgatroyd equation.¹⁷ Calculating the mobility with this equation leads to similar μ_h values. The voltage drop V_r originating from the contact and series resistance was measured in a reference device without a polymer layer and was subtracted from the applied voltage. The built-in potential V_{bi} for PEDOT:PSS and gold is estimated to be 0.1 V. The $\log J$ vs. V plots of **PTPD2**, **PTPD3**, and **PTPD4** and the corresponding fits according to equation (1) are illustrated in **Figure 1** (see **Figure S3** for additional log-log plots of J vs. V). The results of the SCLC measurements for **PTPD1** are published elsewhere.¹⁴ All the hole transport mobility values are given in **Table 1**, showing a μ_h in the range of $10^{-4} \text{ cm}^2 \text{ V}^{-1} \text{ s}^{-1}$. The values for the individual layer thicknesses can be found in **Table S2**, **S3**, and **S4** (supporting information). Thus, our measurements reveal that there is no dependence of the hole transport mobility either on the molecular weight or on the polydispersity of the PTPD polymers. This result can be explained by the amorphous character of the polymers which leads to an isotropic charge transport without any aggregation/crystallization effects. On comparing the polymers having hydrophilic and hydrophobic substituents, we find a similar μ_h for the polymers with ethylhexyloxy side chains (**PTPD1-3**) as well as for the polymer with oligo ethylene glycol side chains (**PTPD4**). These values are in the same range of those reported for spiro-MeOTAD by Nelson et al.¹⁸

2.3. Effect of doping PTPDs on absorption and charge carrier density

Next, we study the mechanism as well as the effect of doping on **PTPDs** using the Co(III)-complex, tris(2-(1H-pyrazol-1-yl)pyridine)cobalt(III).⁷ The **PTPDs** have a suitable oxidation potential for the use of this dopant. Since there is no difference in the hole transport mobilities or in their HOMO values of the polymers, we use one polymer (**PTPD2**) as a typical example for our doping experiments.

First, the influence of doping on charge carrier density in hole only devices was investigated. As known from the literature, doping of semiconducting polymers leads to a higher charge carrier density. Thus, the calculated mobility in doped devices increases due to this increased charge carrier concentration.¹⁹ The sample preparation for the *J-V*-measurements was adapted from section 2.2, except that the active layer was doped with 10 wt.% Co(III)-complex prior to spin-coating. If we consider the SCLC regime in the *J-V*-plots (1 to 5 V), the current density is six times higher for the doped device in comparison to the undoped one. Calculating the μ_h from the doped devices leads to $2.8 \cdot 10^{-3} \text{ cm}^2 \text{ V}^{-1} \text{ s}^{-1}$, which is one order of magnitude higher compared to the undoped devices. The $\log J$ vs. V plots for an undoped and a doped device are depicted in **Figure S5**.

As next step, the doping mechanism was investigated by UV-vis-NIR measurements in THF solution, as illustrated in **Figure 2**. **PTPD2** was mixed with different amounts (4, 6, 8, and 10 wt%) of the dopant and the absorption was measured. Addition of the Co(III)-complex, leads to three new absorption bands at 490, 694, and 860 nm as well as an absorption band in the near IR region at 1403 nm.

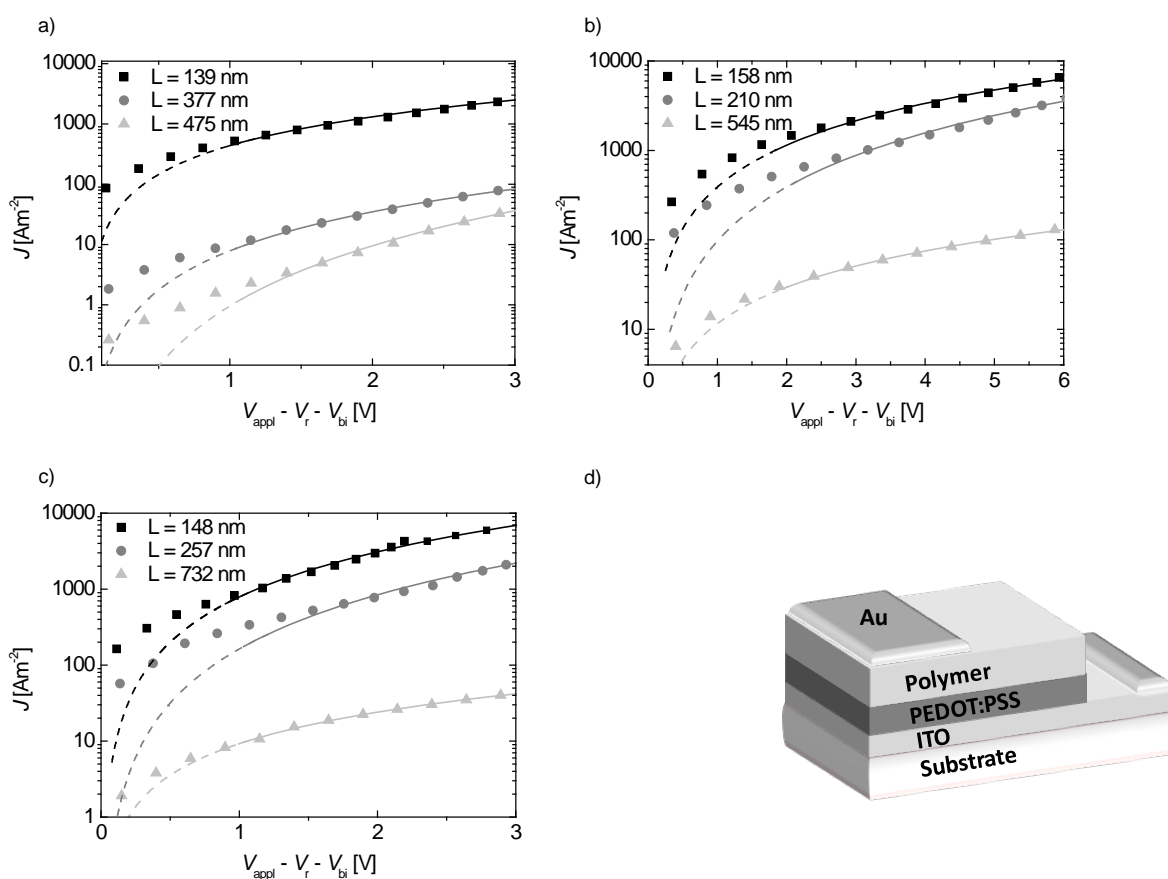


Figure 1. Log-linear plots of current density J vs. voltage V (data points) and fits according to equation 1 (straight lines) at room temperature for the hydrophobic polymers a) PTPD2 and b) PTPD3 as well as for the hydrophilic polymer c) PTPD4 for different layer thicknesses; d) Scheme of a hole only device with gold as top electrode and PEDOT:PSS as bottom electrode.

Increasing amount of dopant increases the intensity of these absorption bands. Simultaneously, the absorption peak of the **PTPD2** at 380 nm decreases. We verified the origin of these peaks by spectroelectrochemical measurements (see **Figure 2b**). For that purpose, **PTPD2** was dissolved in a 0.1 M tetrabutylammonium hexafluorophosphate solution in THF. In a cuvette with a counter electrode (Pt) and a Pt-net as working electrode, a potential was applied. As depicted in **Figure 2b** similar peaks as shown for the chemical doping in **Figure 2a** arise during the spectroelectrochemical measurement. The new absorption bands in the long wavelength region correspond to the radical cation species of triphenylamine, which is known in the literature.²⁰ Consequently, the Co(III)-complex oxidizes the **PTPD2** which leads to cationic polarons resulting in a higher charge carrier density.²¹

2.3. Photovoltaic Properties

In order to understand the influence of side chain polarity and the suitability of these polymers as HTL in perovskite ($\text{CH}_3\text{NH}_3\text{PbI}_3$) cells, we selected the polymers **PTPD2** and **PTPD4** having comparable molecular weights, but different side groups. All photovoltaic devices were prepared by a modified literature procedure as described in the experimental part.¹ A structured fluorine-doped tin oxide (FTO) substrate was coated with a thin TiO_2 blocking layer. After deposition of mesoporous titania (mp- TiO_2), the perovskite was coated by a sequential dipping technique. After drying, the HTL was spin coated and gold was evaporated. First, we address the effect of doping and additives in the HTL followed by the difference in polarity of the two polymers and finally the storage effects on solar cell parameters.

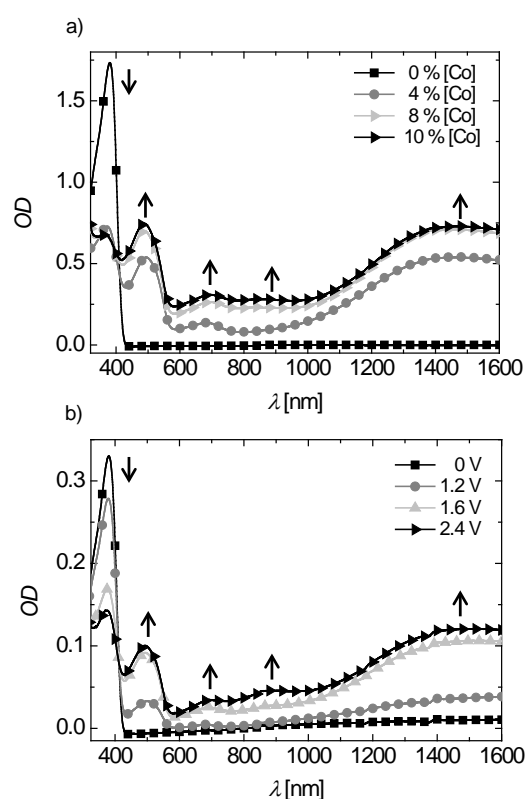


Figure 2. a) UV-vis-NIR absorption spectra of **PTPD2** in THF solution (0.025 mg ml^{-1}). Stepwise addition of the Co(III)-complex leads to four new bands at 490, 694, 860 nm, and 1403 nm. b) Spectroelectrochemical measurements in THF with 0.1 M tetrabutylammonium hexafluorophosphate as conducting salt resemble the oxidative doping.

2.3.1 Effect of doping and additives

In order to learn about the influence of the doping, photovoltaic cells with Co(III)-doped **PTPD2** was exemplarily selected and compared with undoped cells. The dopant concentration was varied from 4 to 10 wt.%. But here only the 10 wt.% doped cells are discussed, since they show the best improvement in devices. Furthermore, the influence of conducting salt lithium bis(trifluoromethanesulfonyl)imide (LiTFSI) and 4-*tert*-butylpyridine (TBP) as additives for the HTL are studied. The J - V -characteristics were measured and for a better understanding of the results, the series (R_S) and shunt resistances (R_{SH}) of the cells were determined by evaluating the slope of the J - V curve at V_{OC} and J_{SC} .²² The inverse of the slopes give the specific resistances in $\Omega \text{ cm}^2$. In the first experiment, the photovoltaic devices were measured immediately after preparation under ambient conditions. **Figure 3** shows the J - V -characteristics and the corresponding external quantum efficiencies (EQE) curves of the photovoltaic devices. The photovoltaic parameters with corresponding average values obtained under air are summarized in **Table 2**.

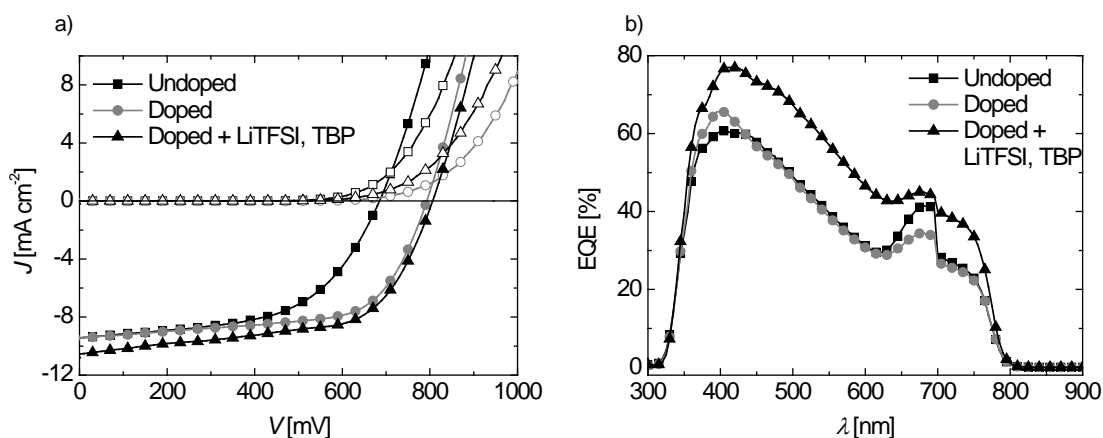


Figure 3. Photovoltaic characterization of devices using **PTPD2** undoped (squares), doped (circles), and doped containing the additives LiTFSI and TBP (triangles) measured immediately after preparation. a) J - V -characteristics of the three photovoltaic devices (best cells) measured at a simulated AM1.5G solar irradiation of 100 mW cm^{-2} in forward bias under ambient conditions. b) EQE-spectra of the devices measured under ambient conditions. The artifact at about 700 nm is due to the switching of the lamps from one wavelength range to the other.

For the undoped devices, we find an average open circuit voltage (V_{OC}), short-circuit current density (J_{SC}), and fill factor (FF) of 715 mV, 8.05 mA cm^{-2} , and 0.59, respectively. This leads to an average power conversion efficiency (PCE) of 3.37 %. The corresponding R_S and R_{SH} are 14 and $891 \Omega \text{ cm}^2$. Upon the addition of dopant, the PCE increases to 4.22 %, mainly due to the higher

V_{oc} of 775 mV and J_{sc} of 9.7205 mA cm⁻². The mean R_s does not change, whereas the R_{sh} is decreased considerably. As a result of the addition of LiTFSI and TBP, the J_{sc} increases significantly to 11.23 mA cm⁻² in average. The V_{oc} slightly improves to 815 mV and the PCE increases to 4.39 % in average. The record cell showed a PCE of 5.10 %. Moreover, the average R_s increases only slightly and the R_{sh} decreases drastically to 149 Ω cm² resulting in lowering of FF. Thus, the overall performance of the cells can be improved by doping and addition of LiTFSI and TBP, mainly due to the improvement in V_{oc} and J_{sc} . The corresponding EQE measured under ambient atmosphere are given in **Figure 3b**.

Table 2. Photovoltaic parameters using **PTPD2** undoped, doped and doped containing LiTFSI and TBP as additives. The devices were measured directly after preparation and under ambient conditions. The parameters for the best devices and the average values for seven cells are given.

	J_{sc}	V_{oc}	FF	PCE	R_s	R_{sh}
	[mA cm ⁻²]	[mV]		[%]	[Ω cm ²]	[Ω cm ²]
A) Undoped (best)	9.25	685	0.57	3.59	15	408
Average value	8.05	715	0.59	3.37	14	891
RMS deviation	± 0.8	± 50	± 0.04	± 0.39	± 2	± 580
B) doped (best)	9.58	795	0.63	4.78	12	608
Average value	9.72	775	0.57	4.22	13	340
RMS deviation	± 1.4	± 52	± 0.05	± 0.58	± 2	± 120
C) doped +						
LiTFSI, TBP (best)	10.54	805	0.60	5.10	12	272
Average value	11.24	815	0.48	4.39	15	149
RMS deviation	± 0.9	± 10	± 0.08	± 0.50	± 3	± 66

We find a significant improvement of the EQE for the whole range of absorption for the doped device with additives LiTFSI and TBP compared to the undoped one. The EQE of the doped device reaches 77 % at maximum absorption of 413 nm, while in the long wavelength region of

600 to 750 nm, around 40 % EQE are maintained. These results confirm the effect of the additives which lead to a higher photocurrent in the solar cell devices.

2.3.2 Nature of side chains: hydrophobic vs. hydrophilic

In the following section, the device results for the **PTPD4** carrying hydrophilic substituents are compared with those for **PTPD2** containing alkyl substituents. Due to the difference in polarity of the side chains in these polymers, the polymer / perovskite interface can be expected to be influenced differently. For all devices, **PTPD2** and **PTPD4** were doped with 10 wt.% Co(III)-complex and the additives LiTFSI and TBP were used. The J - V -measurements were carried out immediately after the preparation under ambient conditions. In **Figure 4** a comparison of the J - V -characteristics of the best devices are shown. The photovoltaic parameters for the highest-performing devices as well as average values for **PTPD4** are given in **Table S6**.

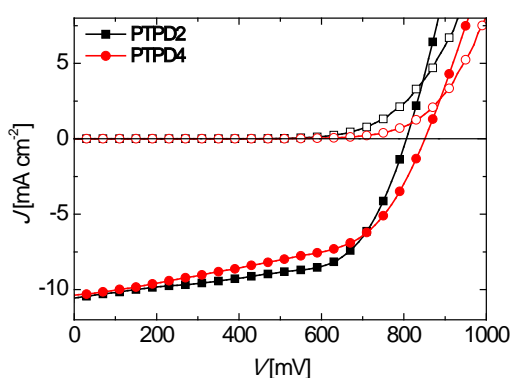


Figure 4. J - V -characteristics in light (filled symbols) and in dark (empty symbols) for the best devices with **PTPD2** (squares) and **PTPD4** (circles) both doped and containing the additives LiTFSI and TBP. The devices were measured in air immediately after preparation at a simulated AM1.5G solar irradiation of 100 mW cm⁻² in forward bias.

For the devices with **PTPD4** measured directly after the preparation, a mean V_{OC} , J_{SC} , and FF of 804 mV, 9.62 mA cm⁻², and 0.58, respectively are achieved. This leads to a PCE of 4.44 % in average and 4.62 % for the best performing device. On comparison the **PTPD2** device delivered an average PCE of 4.39 %. Thus, the obtained results are comparable for both type of polymers. However, the R_S for the best device with **PTPD4** is 20 Ω cm², compared to 12 Ω cm² for **PTPD2**. The R_{SH} slightly increases from 272 Ω cm² to 378 Ω cm² for **PTPD2** to **PTPD4**.

In the following, we address the question of hysteresis in the J - V -measurements for both type of devices. It was shown in the literature that a strong hysteresis effect exists in J - V -curves in perovskite devices which is attributed to interface effects, trap filling, ion migration etc.²³ Devices with spiro-OMeTAD as HTL showed a better performance when measured in a backward bias compared to the forward bias. The hysteresis effect in J - V -curves is only detectable under illumination, but not in dark measurements. In order to investigate the hysteresis effect in our systems, we measured the devices with doped HTL containing LiTFSI and TBP in forward (from low to high forward bias) and in backward scan (from high to low forward bias) for both polymer systems. The corresponding J - V -curves for **PTPD2** and **PTPD4** are illustrated in **Figure 5** and the photovoltaic parameters can be found in **Table S7**.

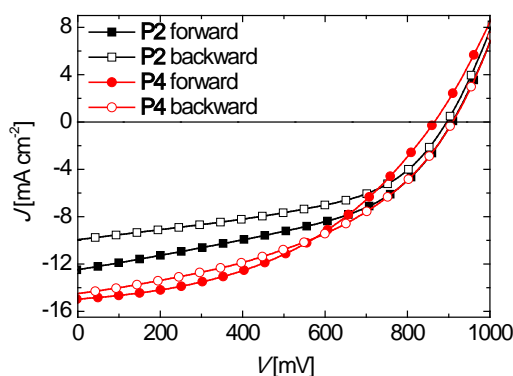


Figure 5. J - V -characteristics for devices using **PTPD2** (squares) and **PTPD4** (circles) as HTL, both doped and with LiTFSI and TBP as additives. The forward scan (filled symbols) and backward scans (empty symbols) were measured at a simulated AM1.5G solar irradiation of 100 mW cm^{-2} under ambient conditions.

An obvious hysteresis occurs for both devices. The measurements in forward bias result in higher PCEs. This is in contrast to the results for spiro-OMeTAD, where the PCE improved due to a higher FF in backward scans. Clearly, **PTPD4** shows a less pronounced hysteresis compared to **PTPD2**. In the case of **PTPD2** the backward scan improves the FF along with a decrease in J_{sc} resulting in low PCE. On the other hand for **PTPD4** no considerable change is observed in any of the parameters. In the case of spiro-OMeTAD devices it was reported that the PCE could be improved due to a higher FF in backward scans.²³

Another positive effect of the hydrophilic polymer **PTPD4** is evident in the following experiment. Devices with **PTPD2** and **PTPD4** (both doped and containing additives) were measured after five minutes under illumination in air. The PCE of the devices with **PTPD2** decreases drastically from 5.08 % to 2.35 %. This is mainly due to the reduced J_{sc} . In contrast to

that, the devices with **PTPD4** are highly stable. Here, the PCE is 6.50 % compared to 6.59 % after five minutes under illumination. The corresponding J - V -characteristics are shown in **Figure 6**.

In summary, **PTPD2** with ethylhexyloxy and **PTPD4** with oligo ethylene glycol side chains deliver similar PCEs directly after preparation in forward bias and under ambient conditions. However, **PTPD4** shows a less hysteresis effect and it has a higher stability under illumination. This could be attributed to interfacial effects due to the oligo ethylene glycol side chains. Due to the hydrophilic character, the wetting behavior of this polymer on perovskite is expected to be more suitable for the polar surface of the mp-TiO₂ covered with the perovskite layer. Accordingly, a better coverage of the perovskite crystals can be observed for **PTPD4** in SEM measurements compared to that of **PTPD2** (see supporting information **Figure S6**).

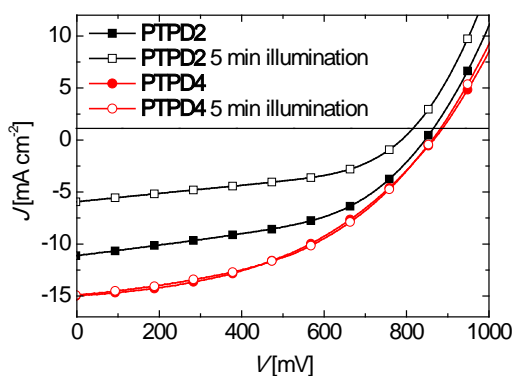


Figure 6. J - V -characteristics for devices using **PTPD2** (squares) and **PTPD4** (circles) as HTL. Both HTLs are doped and contain the additives LiTFSI and TBP. The filled symbols represent the first measurement, the unfilled symbols the measurement after five minutes illumination under light. All devices were measured at a simulated AM1.5G solar irradiation of 100 mW cm⁻² under ambient conditions.

2.3.3. Influence of storage on photovoltaic parameters

To investigate whether storage has an influence on the solar cell parameters, we stored the devices which were doped and having additives (best performing) for both types of polymers (**PTPD2** and **PTPD4**) for five months under dry nitrogen atmosphere in a glovebox (rest oxygen content: 30 ppm). We selected the conditions such that the perovskite will not be damaged due to moisture. It is reported, that the incorporation of water of crystallization leads to the formation of yellow CH₃NH₃PbI₆ · 2 H₂O which decreases the performance of perovskite solar cells.²⁴ As an example, **Figure 7** illustrates a comparison of the PCE, J_{sc} , V_{oc} and FF of the doped devices with additives for **PTPD2** and **PTPD4** as HTL measured under air immediately after preparation (0 months) and after five months storage under nitrogen. The photovoltaic parameters after storage and average values can be found in **Table S5** and **S6**. All the

photovoltaic parameters except FF improve considerably on storage under nitrogen. This was very surprising since organic or hybrid solar cells usually degrade on storage.

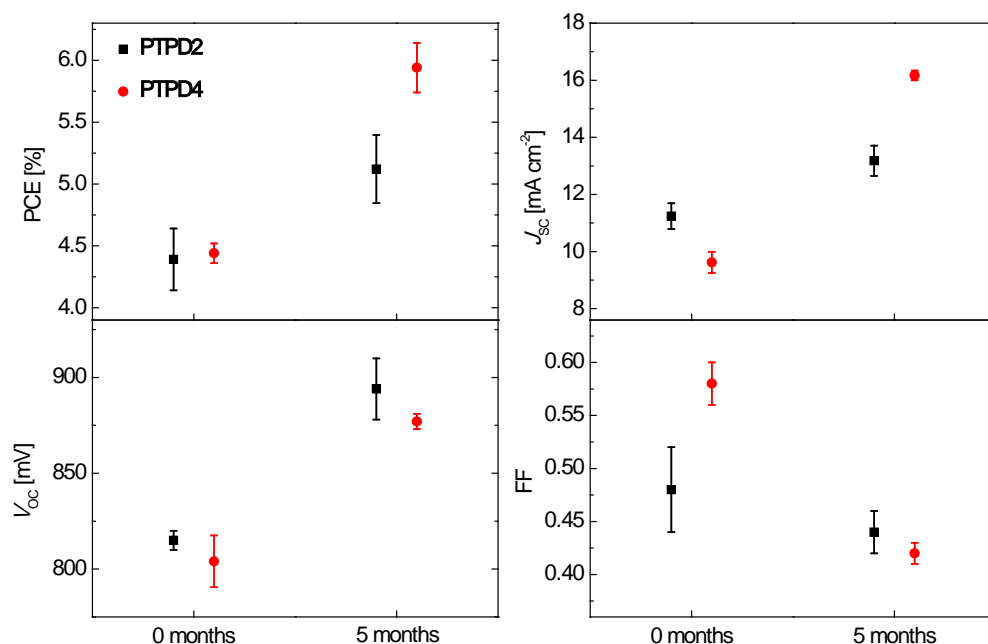


Figure 7. Dependence of the mean power conversion efficiency, short circuit current density, open circuit voltage, and fill factor values on storage for **PTPD2** (filled squares) and **PTPD4** (empty squares), both doped and containing the additives LiTFSI and TBP and measured under air.

After 5 months storage, the average PCE for **PTPD2** device improves from 4.39 % to 5.12 %. The best device exhibited an efficiency of 5.87 %. This is mainly due to the enhanced J_{sc} and V_{oc} (see **Table S5**). The R_s decreases slightly, whereas the R_{sh} increases on storage, causing an overall decrease in FF from 0.58 to 0.45.

In the case of **PTPD4**, the V_{oc} reaches 877 mV, J_{sc} 16.17 mA cm⁻², and FF 0.42, leading to a mean PCE of 5.94 % on storage. The highest performing device improves its efficiency from 4.62 % to 6.50 %. Here also storing the devices for five months under nitrogen improves the V_{oc} as well as the J_{sc} significantly. Also for **PTPD4**, the FF is reduced in accordance with the observed resistance values. To sum up, storage improves the overall performance of both types of devices (**PTPD2** and **PTPD4**) mainly due to higher V_{oc} and J_{sc} .

In order to understand the unexpected improvement of the solar cell performance on storage, we compare the EQE and UV-vis absorption in **Figure 8** for **PTPD2** device. Directly after preparation, the EQE reaches 65 % at its maximum of 400 nm. In the long wavelength region (500 to 800 nm), the EQE is only 30 %. Upon storage, the EQE significantly changes its shape. A

considerably high EQE over the 500 to 800 nm region is observed. In this region, **PTPD2** does not absorb and the contribution to EQE comes only from the perovskite layer. The UV-vis measurements show a comparative increase of optical density in the long wavelength region from 500 to 800 nm on storage. If the change in EQE (Δ EQE) is compared with the change in optical density (Δ OD), it is obvious that the increased EQE contribution arises from additional absorption in the perovskite layer. It is known in the literature that defects within $\text{CH}_3\text{NH}_3\text{PbI}_3$ in mp- TiO_2 cause an optical blue shift resulting in less light harvesting and low EQE.²⁵ Owen et al. have reported a detailed analysis of the blue shift in absorption spectra using pair distribution function analysis of X-ray scattering on perovskites. These authors clearly point out the fact that the disordered and amorphous phases, which are not visible in conventional XRD measurements, are important for device efficiency due to changes in absorption depending on medium or long range structural coherence. Probably, the improvements observed here can be of a similar nature. But this has to be studied in a systematic way to draw final conclusions. A very same trend occurs for the devices with **PTPD4** on storage (see supporting information, **Figure S7**).

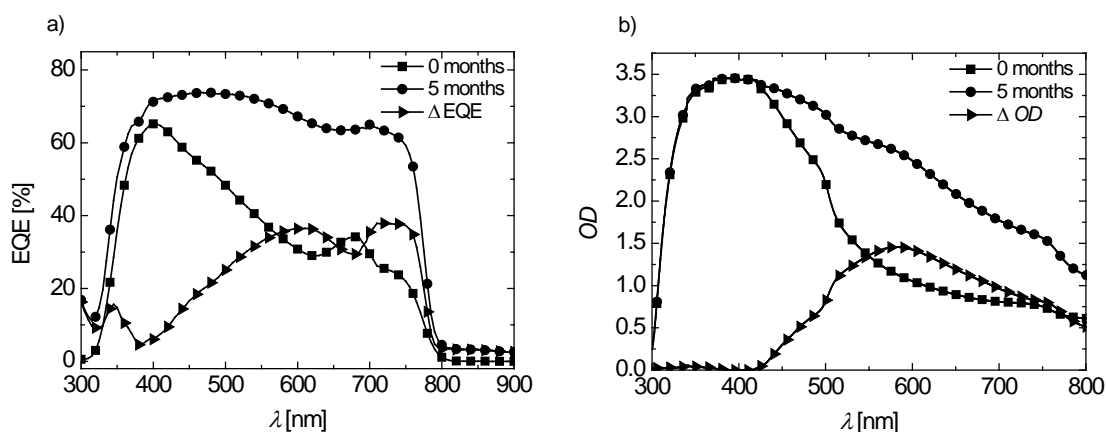


Figure 8. Comparison of devices with **PTPD2** doped and containing LiTFSI and TBP as additives: freshly prepared (squares), stored devices, and difference of both (triangles). a) EQE-spectra; The artifact between 650-700 nm is due to the switching of the lamps from one wavelength range to the other. b) UV-vis absorption. All measurements were carried out under ambient conditions.

Since the devices are not encapsulated and there is a considerable improvement on the photovoltaic performance of the devices with **PTPD2** and **PTPD4** on storage under nitrogen, we measured the stored devices also under nitrogen atmosphere. This was done in order to keep the adverse effects of moisture as low as possible during the measurements. The photovoltaic parameters for these measurements under nitrogen can be found in **Table S5** and **S6**.

For **PTPD2** the average PCE increases when measured under nitrogen ($\eta = 5.12$ to 5.84 %), for **PTPD4** no improvement is observed ($\eta = 5.94$ to 5.43 %). For the champion cells, it is more pronounced and the efficiency values reach 7.69 % for **PTPD2** and 6.44 % for **PTPD4**. In the case of **PTPD2** the big improvement under nitrogen is seen in FF (0.46 to 0.68), whereas for **PTPD4** the decrease in FF is compensated by the increase in V_{oc} and thus the solar cell performance remains the same. The decrease in J_{sc} for the best performing cell is only very marginal (14.0 to 13.4 mA cm⁻² for **PTPD2** and 16.65 to 16.43 mA cm⁻² for **PTPD4**) and are within the errors of reproducibility and measurement. However, the average J_{sc} values for both types decrease. It has been reported that the conductivity of the hole transport material can be improved by oxygen doping in the case of easily oxidizable hole conductors such as spiro-OMeTAD.²⁶ Accordingly, device performances have been shown to decrease during storage under argon or vacuum.²⁷ A similar effect may be expected in the case of PTPDs as well.

3. Conclusion

In conclusion, we investigated the material properties of **PTPD** main-chain polymers and the influence of chemical structure and properties on the solar cell performance in combination with CH₃NH₃PbI₃. Appreciably good hole transport mobility with no dependence on the molecular weight and polydispersity was observed for these polymers. Furthermore, Co(III)-complex causes an oxidative doping of these polymers leading to higher charge carrier density and high conductivity. The mechanism of doping was also supported by spectroelectrochemical studies. The combination of dopant and use of the additives (LiTFSI and TBP) gave the best results for perovskite solar cells involving these polymers. On comparison of **PTPD2** carrying ethylhexyloxy side chains with **PTPD4** containing hydrophilic oligo ethylene glycol side chains, we observed less hysteresis and higher photostability for the latter. Both types of devices exhibit unexpected significant improvements on storage under nitrogen. The improvements in photovoltaic parameters can be clearly attributed to increased absorption resulting in very high EQE values for a broad range of absorption. Since the two polymers differ only in the nature of their side chains, the positive effects of **PTPD4** devices can be attributed to the hydrophilic nature of its side chains, which is highly compatible at the interface with CH₃NH₃PbI₃ material.

4. Experimental Section

4.1 Synthesis

The monomer synthesis and the synthesis of **PTPD1** is described elsewhere.¹⁴

General procedure for Yamamoto polymerization: 2,2'-Bipyridine (3.64 mmol, 2.2 eq) and 1,5-cyclooctadiene (3.64 mmol, 2.2 eq) were dissolved in 2.3 ml dimethylformamide (DMF). The solution was degassed for 30 min. bis(1,5-cyclooctadien)nickel (3.64 mmol, 2.2 eq) was added and the solution was heated to 80 °C for 30 min under stirring. The monomer (1.65 mmol, 1 eq) was dissolved in 2.5 ml toluene in a separate flask and degassed for 30 min. Subsequently the monomer solution was added to the catalyst solution by a syringe. The reaction mixture was stirred for 7 days at 80 °C under argon. Degassed bromobenzene was added for endcapping. After 24 h the reaction mixture was poured into methanol/HCl (1:1) and the precipitate was filtered off. For further purification soxhlet extraction in methanol and acetone were performed. Yield: 81 %.

¹H NMR (300 MHz, CDCl₃, δ): 7.44 (d, 2H, Ar H), 7.09 (d, 2H, Ar H), 6.87(m, 6H, Ar H), 3.83 (d, *J* = 5.2, 2H, OCH₂), 1.73 (m, 1H, CH), 1.50 (m, 8H, CH₂), 1.34 (s, 12 H, CH₃), 0.92 (m, 6H, CH₃).

4.2 Characterization

Dry solvents were purchased from Aldrich and Acros, other solvents were distilled once before use.

M_n and *M_w* values were determined by SEC in THF using a guard column (Varian, 50 × 0.75 cm, ResiPore, particle size 3 μm) and two separation columns (Varian, 300.75 cm, ResiPore, particle size 3 μm) and a Waters 515-HPLC pump with stabilized THF. The flow rate was 0.5 mL min⁻¹. The compounds were monitored with a Waters UV detector at 254 nm. The SEC systems was calibrated against polystyrene. DSC analysis was performed on a Perkin Elmer Diamond DSC, calibrated with indium. *T_g* were determined using a scanning rate of 20 °C min⁻¹ under a nitrogen flow.

SCLC devices were fabricated on structured ITO-coated glass substrates using AZ 1518 photo paint from Microchemicals to define the active area and to prevent edge effects. The devices were then plasma edged and a 50 nm PEDOT:PSS (Clevios) layer was spin coated into the active area. The PEDOT:PSS layer was heated up to 120 °C for 30 min, followed by doctor blading from chlorobenzene solutions of the polymer layer on top of it. Then a 40 nm gold layer was

evaporated at 5×10^{-7} mbar. The device measurements were performed under active vacuum at room temperature with a Keithley source measure unit.

UV-vis measurements in THF solutions (0.025 mg ml^{-1}) were carried out on a Hitachi U-3000 two-beam-photometer. For the spectroelectrical measurements a voltammetry cell from ALS Co., Ltd with 1 mm path length, a platin-net as electrode and tetrabutylammonium hexafluorophosphate as conducting salt was used.

For the perovskite solar cells a TiO_2 blocking layer was deposited by spray pyrolyses of titanium(IV)bis(acetoacetonato)-di(isopropanoxylate diluted in ethanol at $450 \text{ }^\circ\text{C}$ on FTO coated glass substrates and annealed at $450 \text{ }^\circ\text{C}$. Next, the mp- TiO_2 layer was prepared by doctor blading using a commercial TiO_2 paste (Solaronix T/SP) diluted with Terpeneol. The films were gradually heated to $450 \text{ }^\circ\text{C}$ and baked for 15 min at this temperature. After cooling, the substrates were handled in a glovebox under nitrogen atmosphere. The active layer was prepared by a sequential deposition method. First, PbI_2 was spin-coated on top of the mp- TiO_2 . Second, the perovskite pigment was formed by dipping the substrate into a solution of $\text{CH}_3\text{NH}_3\text{I}$ in isopropanol (10 mg ml^{-1}). Before dipping the substrate in the $\text{CH}_3\text{NH}_3\text{I}$ solution it was prewetted in isopropanol. After drying at $70 \text{ }^\circ\text{C}$, a thin layer of the PTPD polymer was spin-coated. In a last step gold electrodes with a thickness of 60 nm were thermally evaporated.

The photovoltaic current-voltage measurements were carried out by a Keithley 6517 Source-Measure unit under AM 1.5 G conditions (Solar simulator-A grade from Newport). The intensity of the light was calibrated with a standard Si-reference cell from the Fraunhofer Institute for Solar Energy Systems (ISE), Freiburg, as 100 mW cm^{-2} . The EQE values were measured using a Bentham PVE300 under short-circuit conditions after illuminating the devices with monochromatic light from a Xenon lamp passing through a Bentham TMc300 monochromator.

Supporting Information

Supporting Information is available from the Wiley Online Library or from the author.

Acknowledgements

We acknowledge the Deutsche Forschungsgemeinschaft (Graduate School GRK 1640) for financial support and KN thanks the Universität Bayern e.V. for the financial support in form of a scholarship of the Bayerische Graduiertenförderung and the Elitenetzwerk Bayern (ENB). We also like to thank Frank Schirmer for ITO patterning and Katja Gräf for the synthesis of the Co(II)-complex and fruitful discussions.

5. References

- 1 J. Burschka, N. Pellet, S.-J. Moon, R. Humphry-Baker, P. Gao, M. K. Nazeeruddin and M. Grätzel, *Nature*, 2013, **499**, 316–319.
- 2 a) A. Kojima, K. Teshima, Y. Shirai and T. Miyasaka, *J. Am. Chem. Soc.*, 2009, **131**, 6050–6051; b) M. M. Lee, J. Teuscher, T. Miyasaka, T. N. Murakami and H. J. Snaith, *Science*, 2012, **338**, 643–647; c) H.-S. Kim, C.-R. Lee, J.-H. Im, K.-B. Lee, T. Moehl, A. Marchioro, S.-J. Moon, R. Humphry-Baker, J.-H. Yum, J. E. Moser, M. Grätzel and N.-G. Park, *Sci. Rep.*, 2012, **2**, 1–7.
- 3 a) D. Bi, G. Boschloo, S. Schwarzmüller, L. Yang, E. M. J. Johansson and A. Hagfeldt, *Nanoscale*, 2013, **5**, 11686–11691; b) M. H. Kumar, N. Yantara, S. Dharani, M. Graetzel, S. Mhaisalkar, P. P. Boix and N. Mathews, *Chem. Commun.*, 2013, **49**, 11089–11091;
- 4 a) M. Liu, M. B. Johnston and H. J. Snaith, *Nature*, 2013, **501**, 395–398; b) G. E. Eperon, V. M. Burlakov, P. Docampo, A. Goriely and H. J. Snaith, *Adv. Funct. Mater.*, 2013, 151–157.
- 5 D. Liu and T. L. Kelly, *Nature Photon*, 2013, **8**, 133–138.
- 6 K. Walzer, B. Maennig, M. Pfeiffer and K. Leo, *Chem. Rev.*, 2007, **107**, 1233–1271.
- 7 J. Burschka, A. Dualeh, F. Kessler, E. Baranoff, N.-L. Cevey-Ha, C. Yi, M. K. Nazeeruddin and M. Grätzel, *J. Am. Chem. Soc.*, 2011, **133**, 18042–18045.
- 8 a) H. Li, K. Fu, A. Hagfeldt, M. Grätzel, S. G. Mhaisalkar and A. C. Grimsdale, *Angew. Chem. Int. Ed.*, 2014, 4085–4088; b) D. Bi, L. Yang, G. Boschloo, A. Hagfeldt and E. M. J. Johansson, *J. Phys. Chem. Lett.*, 2013, **4**, 1532–1536; c) B. Cai, Y. Xing, Z. Yang, W.-H. Zhang and J. Qiu, *Energy Environ. Sci.*, 2013, **6**, 1480–1485.
- 9 J. H. Heo, S. H. Im, J. H. Noh, T. N. Mandal, C.-S. Lim, J. A. Chang, Y. H. Lee, H.-j. Kim, A. Sarkar, M. K. Nazeeruddin, M. Grätzel and S. I. Seok, *Nature Photonics*, 2013, 486–491.
- 10 J. H. Noh, S. H. Im, J. H. Heo, T. N. Mandal and S. I. Seok, *Nano Lett.*, 2013, 1764–1769.
- 11 C. R. Singh, G. Gupta, R. Lohwasser, S. Engmann, J. Balko, M. Thelakkat, T. Thurn-Albrecht and H. Hoppe, *J. Polym. Sci. Part B: Polym. Phys.*, 2013, **51**, 943–951.
- 12 E. M. Barea, G. Garcia-Belmonte, M. Sommer, S. Hüttner, H. J. Bolink and M. Thelakkat, *Thin Solid Films*, 2010, **518**, 3351–3354.

- 13 A. S. Lang, M.-A. Muth, C. D. Heinrich, M. Carassco-Orozco and M. Thelakkat, *J. Polym. Sci. Part B: Polym. Phys.*, 2013, **51**, 1480–1486.
- 14 K. Neumann, C. Schwarz, A. Köhler and M. Thelakkat, *J. Phys. Chem. C*, 2013, **18**, 27–36.
- 15 K. Gräf, M. A. Rahim, S. Das and M. Thelakkat, *Dyes and Pigments*, 2013, **99**, 1101–1106.
- 16 C. Goh, R. J. Kline, M. D. McGehee, E. N. Kadnikova and J. M. J. Fréchet, *Applied Physics Letters*, 2005, 122110.
- 17 P. N. Murgatroyd, *J. Phys. D: Appl. Phys.*, 1970, **3**, 151–156.
- 18 D. Poplavskyy, J. Nelson, *Appl. Phys. Lett.*, 2003, **93**, 341–346.
- 19 a) V. I. Arkhipov, P. Heremans, E. V. Emelianova, G. J. Adriaenssens and H. Bässler, *Applied Physics Letters*, 2003, **82**, 3245–3247; b) Y. Zhang, B. de Boer and P. W. M. Blom, *Adv. Funct. Mater.*, 2009, **19**, 1901–1905;
- 20 J. Bonvoisin, J.-P. Launay, M. van der Auweraer and F. C. de Schryver, *J. Phys. Chem.*, 1994, **98**, 5052–5057.
- 21 M. Lehnhardt, S. Hamwi, M. Hopping, J. Reinker, T. Riedl and W. Kowalsky, *Appl. Phys. Lett.*, 2010, **96**, 193301.
- 22 J. D. Servaites, M. A. Ratner and T. J. Marks, *Energy Environ. Sci.*, 2011, **4**, 4410–4422.
- 23 a) A. Dualeh, T. Moehl, N. Tétreault, J. Teuscher, P. Gao, M. K. Nazeeruddin and M. Grätzel, *ACS Nano*, 2014, **8**, 362–373; b) H. J. Snaith, A. Abate, J. M. Ball, G. E. Eperon, T. Leijtens, N. K. Noel, S. D. Stranks, J. T.-W. Wang, K. Wojciechowski and W. Zhang, *J. Phys. Chem. Lett.*, 2014, 1511–1515;
- 24 a) B. R. Vincent, K. N. Robertson, T. S. Cameron and O. Knop, *Can. J. Chem.*, 1987, **65**, 1042–1046; b) G. Niu, W. Li, F. Meng, L. Wang, H. Dong and Y. Qiu, *J. Mater. Chem. A*, 2013, **2**, 705–710.
- 25 J. J. Choi, X. Yang, Z. M. Norman, S. J. L. Billinge and J. S. Owen, *Nano Lett.*, 2014, **14**, 127–133.
- 26 U. B. Cappel, T. Daeneke, U. Bach, *Nano Lett.* 2012, **12**, 4925–4931.
- 27 M. Karlsson, Ph.D. Thesis, Uppsala University, 2012.

Supporting Information to
**Perovskite Solar Cells Involving Poly(tetraphenylbenzidine)s: Investigation of Hole
Carrier Mobility, Doping effects and Photovoltaic Properties**

*Katharina Neumann and Mukundan Thelakkat**

K. Neumann, M. Thelakkat

Applied Functional Polymers, Macromolecular Chemistry I

University of Bayreuth
95440 Bayreuth, Germany

*E-mail: mukundan.thelakkat@uni-bayreuth.de

Table of contents

- 1 Methods
- 2 Size exclusion chromatography
- 3 Differential scanning calorimetry
- 4 Space charge limited current measurements
 - 4.1 Log-log plots
 - 4.2 Verification of the relation $J \sim V^2 L^{-3}$
 - 4.3 SCLC results for different layer thicknesses
 - 4.4 Effect of doping in SCLC devices
- 5 Solar cell characterization
 - 5.1 Summary of photovoltaic parameters
 - 5.2 Comparison of EQE and UV-vis upon storage for PTPD4

1 Methods

Cyclic voltammograms (CV) were recorded under moisture- and oxygen-free conditions using a standard three-electrode assembly connected to a potentiostat (model 263A, EG&G Princeton Applied Research) and at a scanning rate of 50 mV sec⁻¹. The working electrode was a glassy carbon disk electrode (area $\frac{1}{4}$ 0.0314 cm²), a platinum wire was used as auxiliary electrode and the quasi-reference electrode was Ag/Ag⁺ composed of a Ag wire and AgNO₃ in acetonitrile. Tetrabutylammonium hexafluorophosphate (Bu₄NPF₆, 0.1 M) was used as the conducting salt. Each measurement was calibrated with an internal standard (ferrocene/ferrocenium). The HOMO values were determined from the value of -5.16 eV for ferrocene with respect to vacuum level and correcting for the solvent effects.

Table S1. Oxidation potentials E_{ox} vs. ferrocene in cyclic voltammetry measurements at 50 mV s⁻¹ in DCM with 0.1 M tetrabutylammonium hexafluorophosphate and calculated HOMO values for **PTPD2-4**.

Polymer	E_{ox1} vs. Fc [eV]	HOMO [eV]
PTPD2	0.10	-5.26
PTPD3	0.10	-5.26
PTPD4	0.11	-5.27

2 Size exclusion chromatography

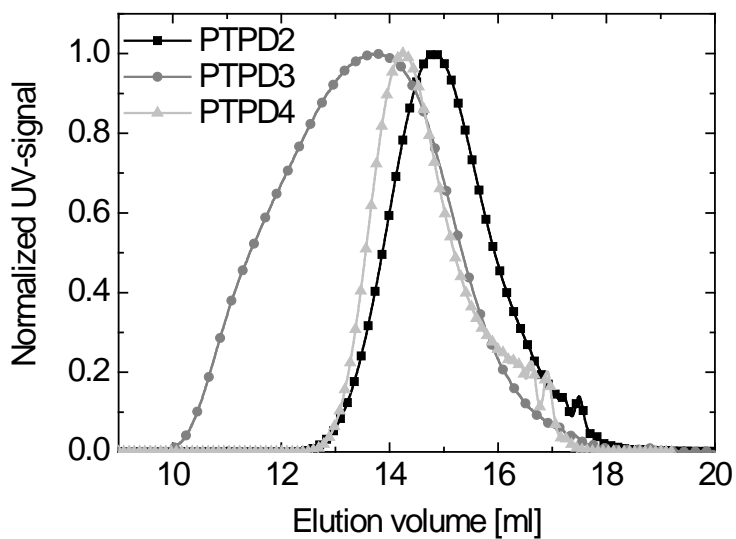


Figure S1. SEC-curves of the polymers **PTPD2**, **PTPD3**, and **PTPD4** measured in THF at room temperature (flow rate: 0.5 ml/min).

3 Differential scanning calorimetry

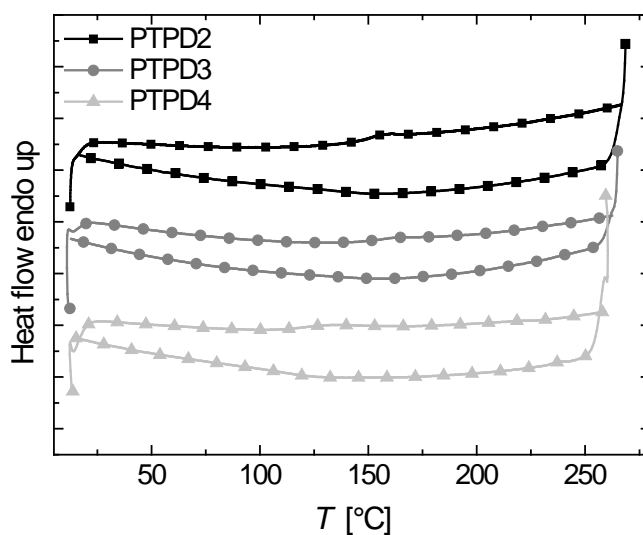


Figure S2. DSC-curves of the polymers **PTPD2**, **PTPD3**, and **PTPD4**. All three polymers show a glass transition.

4 Space charge limited current measurements

4.1 Log-log plots

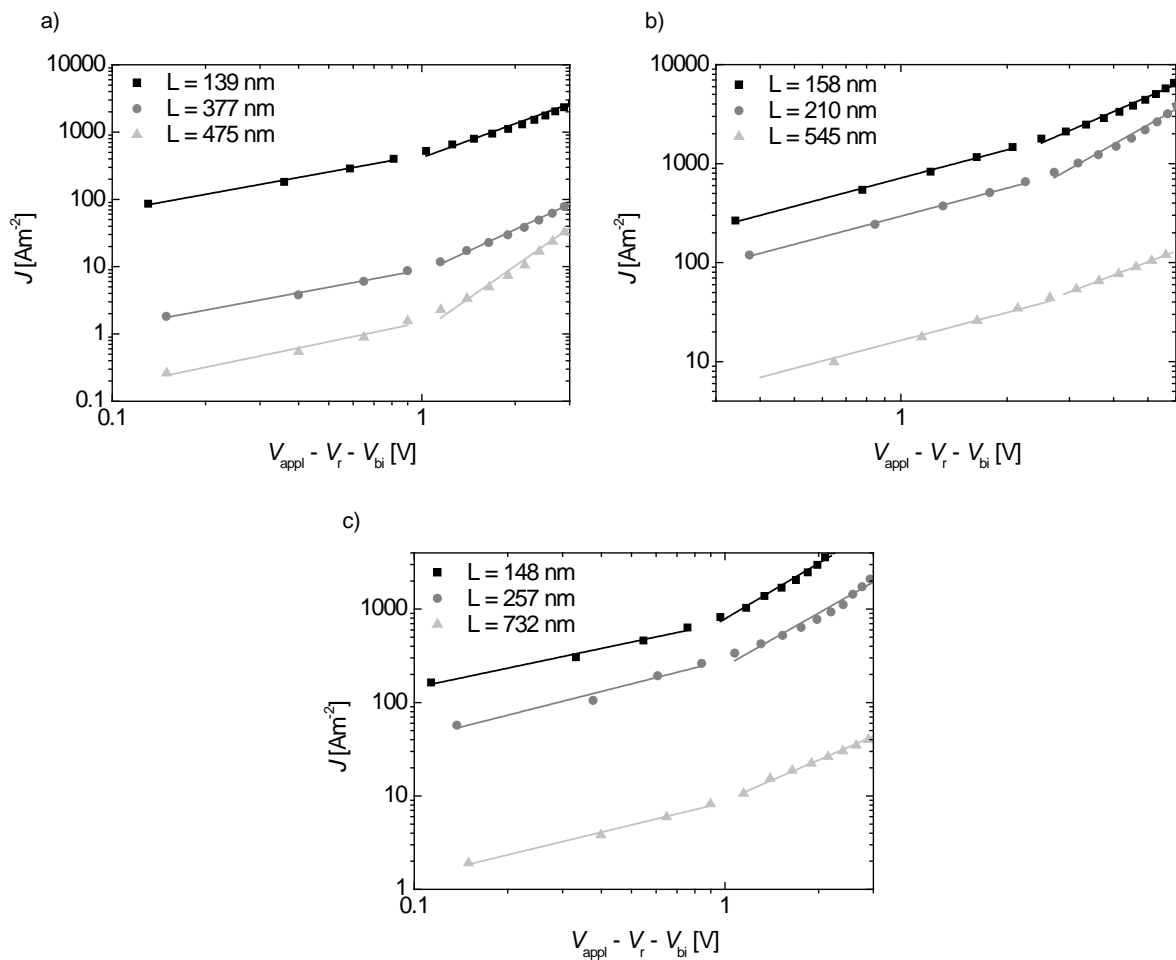


Figure S3. Log-log plots of current density J vs. voltage V (data points) and fits according to equation 1 (straight lines) at room temperature for the polymers a) **PTPD2**, b) **PTPD3** and c) **PTPD4** for different layer thicknesses.

4.2 Verification of the relation $J \sim V^2 L^{-3}$

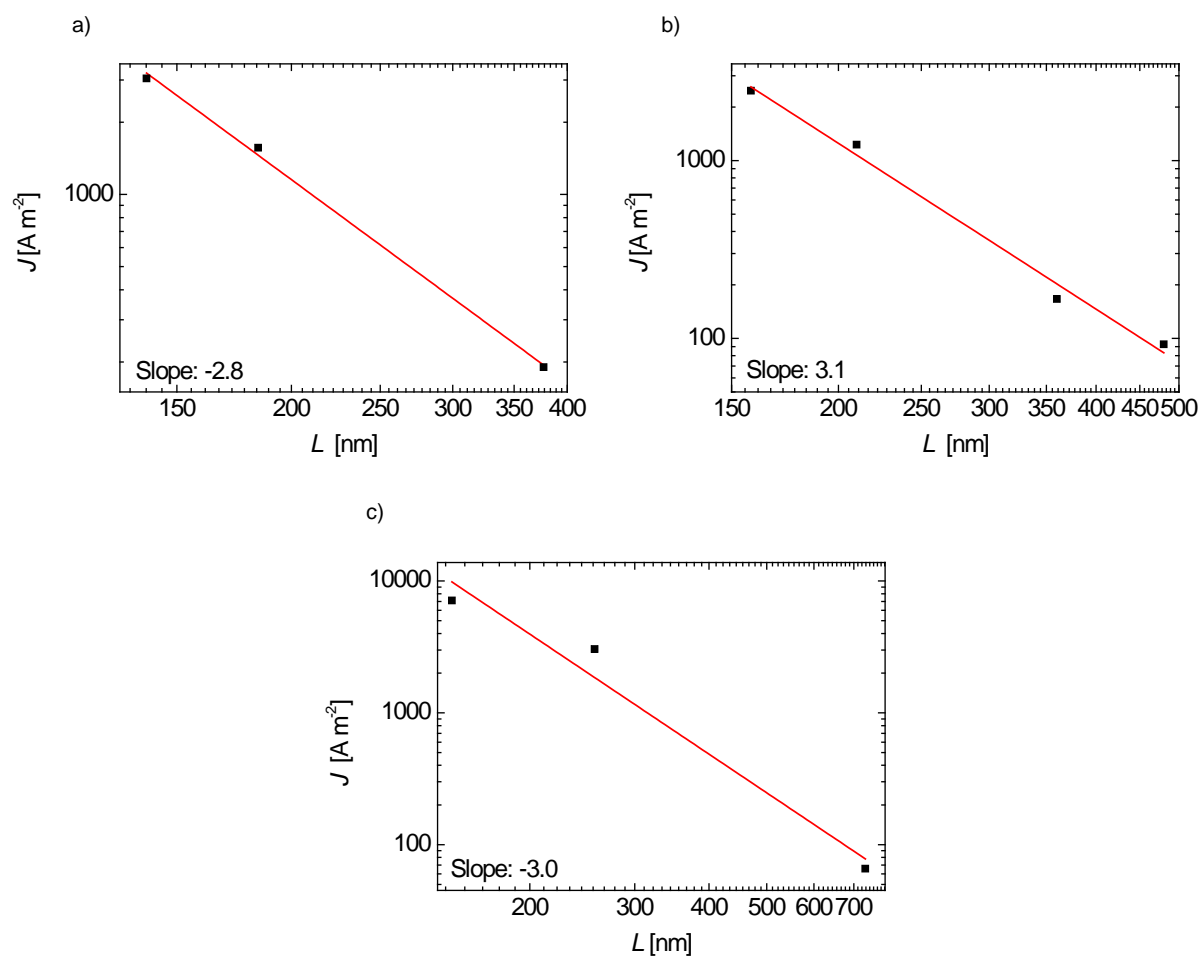


Figure S4. Log-log plot of the thickness dependence of the current density at a fixed bias of 4 V for a) PTPD2, b) PTPD3 and c) PTPD4. The squares are experimental data and the solid line is the fit according to relation $J \sim V^2 L^{-3}$, where L is the thickness of the sample.

4.3 SCLC results for different layer thicknesses

Table S2. Calculated hole transport mobilities μ_h for three layer thicknesses and average value for μ_h for **PTPD2**.

PTPD2	Device	L [nm]	μ_h [$\text{cm}^2\text{V}^{-1}\text{s}^{-1}$]
	1	139	$1.9 \cdot 10^{-4}$
	2	377	$2.0 \cdot 10^{-4}$
	3	475	$5.6 \cdot 10^{-4}$
	<i>Average</i>		$3.2 \cdot 10^{-4}$

Table S3. Calculated hole transport mobilities μ_h for three layer thicknesses and average value for μ_h for **PTPD3**.

Device	L [nm]	μ_h [$\text{cm}^2\text{V}^{-1}\text{s}^{-1}$]
1	158	$1.5 \cdot 10^{-4}$
2	210	$4.1 \cdot 10^{-4}$
3	545	$1.2 \cdot 10^{-4}$
	<i>Average</i>	$2.3 \cdot 10^{-4}$

Table S4. Calculated hole transport mobilities μ_h for three layer thicknesses and average value for μ_h for **PTPD2**.

Device	L [nm]	μ_h [$\text{cm}^2\text{V}^{-1}\text{s}^{-1}$]
1	148	$4.9 \cdot 10^{-4}$
2	257	$8.4 \cdot 10^{-4}$
3	732	$5.4 \cdot 10^{-4}$
	<i>Average</i>	$6.2 \cdot 10^{-4}$

4.4 Effect of doping in SCLC devices

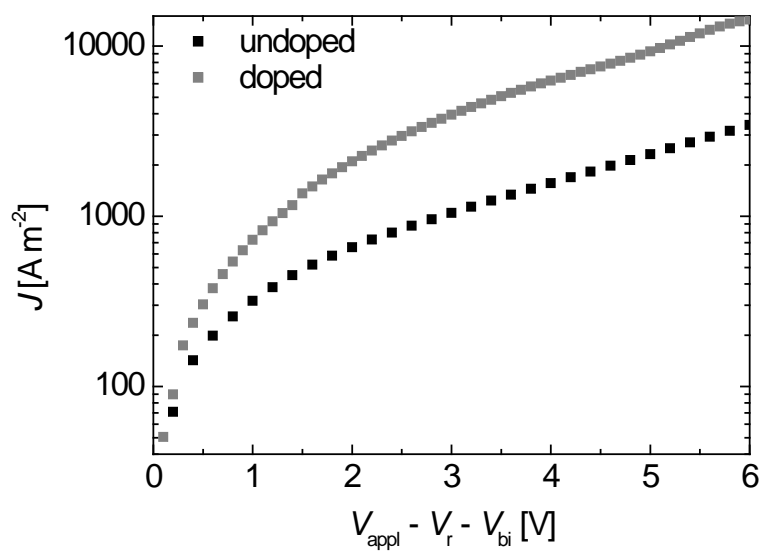


Figure S5. Log-linear-plots of J vs. V for the undoped **PTPD2** and doped SCLC devices with 10 % Co(III)-complex at similar active layer thicknesses of 184 nm.

5 Solar cell characterization

5.1 Summary of photovoltaic parameters

Table S5. Photovoltaic parameters of the devices stored for 5 month under nitrogen using **PTPD2** doped containing LiTFSI and TBP as additives. The devices were measured under ambient conditions and under nitrogen conditions. The parameters for the best devices and the average values for seven cells are given.

PTPD2	J_{sc}	V_{oc}	FF	PCE	R_s	R_{SH}
doped + LiTFSI, TBP	[mA cm ⁻²]	[mV]		[%]	[Ω cm ²]	[Ω cm ²]
<i>Stored 5 month measured under air</i>						
Best value	14.00	910	0.46	5.87	16	179
Average value	13.18	894	0.44	5.12	19	167
RMS deviation	± 1.06	± 32	± 0.04	± 0.55	± 2	± 28
<i>Stored 5 month measured under N₂</i>						
Best value	13.40	918	0.68	7.69	15	8803
Average value	11.62	921	0.54	5.84	19	1665
RMS deviation	± 1.8	± 34	± 0.11	± 1.73	± 3	± 1192

Table S6. Photovoltaic parameters for **PTPD4** doped containing the additives LiTFSI and TBP directly after preparation and stored for 5 months measured under ambient conditions. Stored devices measured under nitrogen atmosphere. Average values for four cells and standard deviation.

PTPD4	J_{sc}	V_{oc}	FF	PCE	R_s	R_{SH}
doped	[mA cm ⁻²]	[mV]		[%]	[Ω cm ²]	[Ω cm ²]
+LiTFSI, TBP						
<i>After preparation measured under air</i>						
Best value	9.81	815	0.58	4.62	20	378
Average value	9.62	804	0.58	4.44	15	3010
	± 0.75	± 27	± 0.04	± 0.16	± 1.5	± 1594
<i>Stored 5 month measured under air</i>						
Best	16.65	866	0.45	6.50	15	427
Average	16.17	877	0.42	5.94	25	352
	± 0.34	± 8	± 0.02	± 0.40	± 4	± 41
<i>Stored 5 month measured under N₂</i>						
Best	16.43	955	0.41	6.44	18	223
Average	14.26	931	0.41	5.43	24	222
	± 0.18	± 39	± 0.04	± 0.7	± 7	± 14

Table S7. Comparison of the photovoltaic parameters for devices with **PTPD2** and **PTPD4** both doped and containing the additives LiTFSI and TBP; measured in air under forward bias (f) and backward bias (b).

	V_{oc}	J_{sc}	FF	PCE	R_s	R_{sh}
	[mV]	[mA cm ⁻²]		[%]	[Ω cm ²]	[Ω cm ²]
Under air						
PTPD2 f	910	14.00	0.46	5.87	16	179
PTPD2 b	898	11.41	0.50	5.11	18	219
PTPD4 f	866	16.60	0.45	6.50	20	378
PTPD4 b	910	16.65	0.43	6.47	18	237

5.2 Comparison of the interfaces of PTPD2 and PTPD4

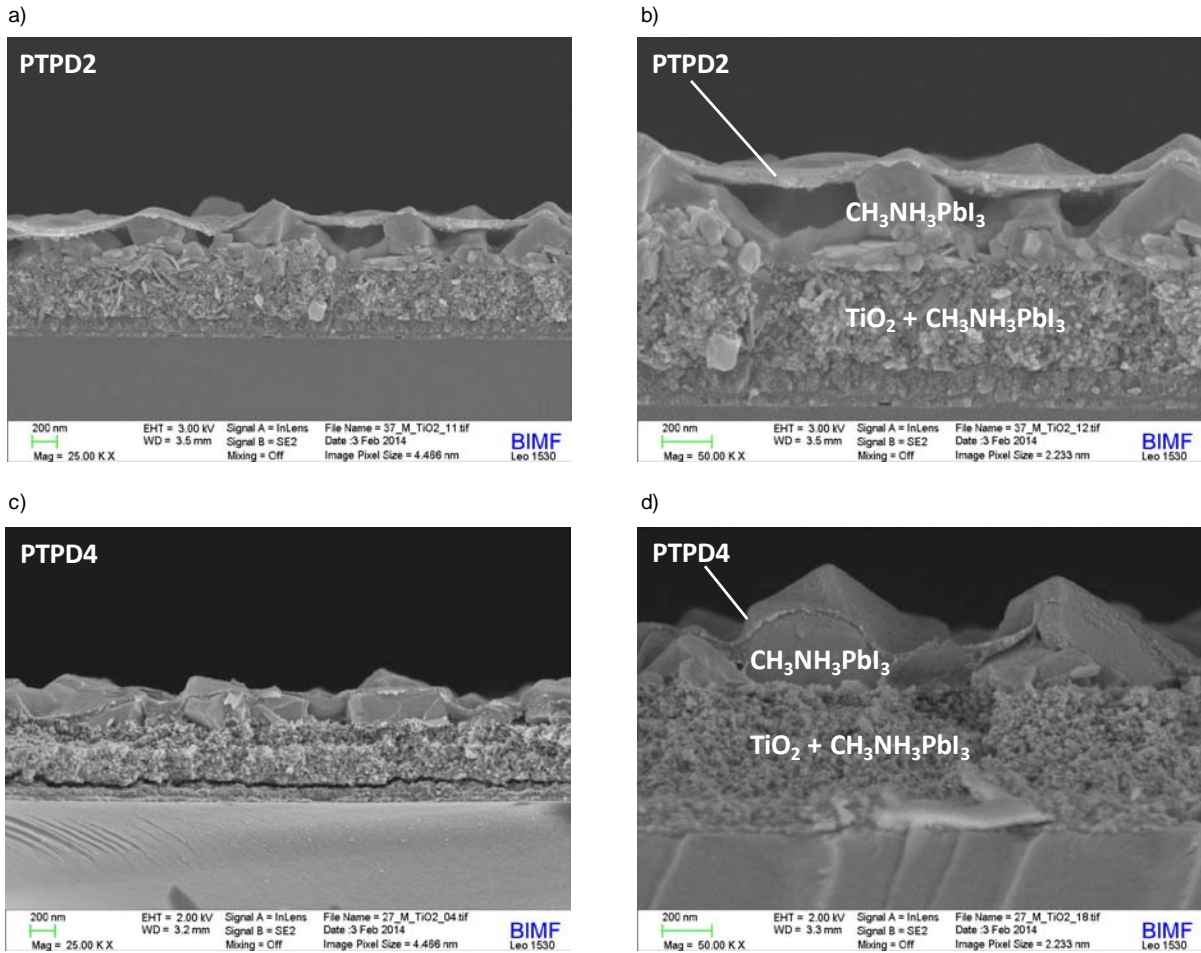


Figure S1. SEM images of devices with **PTPD2** (a) and b)) and **PTPD4** (c) and d)) showing the better compatibility of **PTPD4** with the perovskite crystals.

5.3 Comparison of EQE and UV-vis upon storage for PTPD4

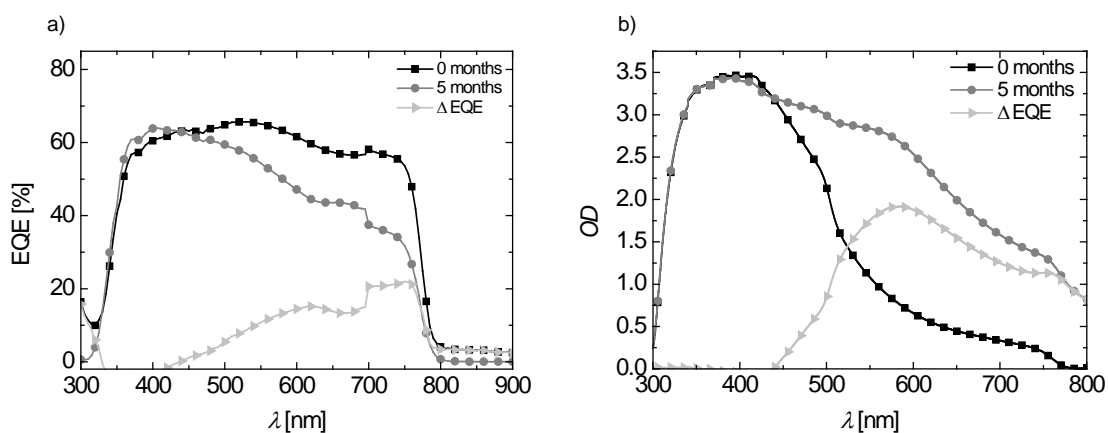


Figure S6. Comparison of freshly prepared devices (squares) and devices stored for 5 months under nitrogen atmosphere (circles) with undoped **PTPD4** and difference between the two devices (triangles) a) EQE-spectra; The artifact between 650-700 nm is due to the switching of the lamps from one wavelength range to the other. b) UV-vis absorption. All measurements were carried out under ambient conditions.

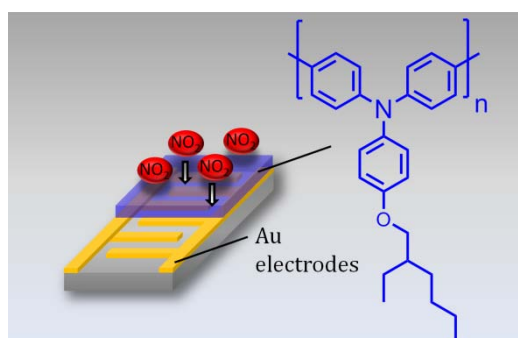
Undoped and doped Poly(tetraphenylbenzidine) as Sensitive Material for an Impedimetric NO₂ Gas Dosimeter

I. Marr,¹ K. Neumann,² M. Thelakkat,² and R. Moos^{1,a)}

¹Department of Functional Materials, University of Bayreuth, Bayreuth, 95440, Germany

²Department of Macromolecular Chemistry I, Applied Functional Polymers, University of Bayreuth, Bayreuth, 95440, Germany

a) Email of corresponding author: ralf.moos@uni-bayreuth.de



Submitted to *Applied Physics Letters*

ABSTRACT

This article presents an NO₂ detecting gas dosimeter based on poly(tetraphenylbenzidine) poly(TPD) as NO_x sensitive layer. Gas dosimeters are suitable devices to determine reliably low levels of analytes over a long period of time. During NO_x exposure, the analyte molecules are accumulated irreversibly in the sensing layer of the dosimeter enhancing the conductivity of the hole conducting poly(TPD) which can be measured by impedance spectroscopy. Due to their possibility for low cost production by simple printing techniques and very good physical, photochemical, and electrochemical properties, poly(TPD)s are suitable for application in gas dosimeters operated at room temperature. We studied the effect of doping with a Co(III)-complex in combination with a conducting salt on the dosimeter behavior. Compared to the undoped material, a strong influence of the doping can be observed: the conductivity of the sensing material increases significantly, the noise of the signal decreases and an unwanted recovery of the sensor signal can be prevented leading to NO_x detection < 10 ppm.

I. INTRODUCTION

In times of strict environmental requirements and a growing demand for energy and mobility, reliable and low analyte concentration-detecting gas sensing devices are required to determine the dose or concentration of toxic and harmful gases, e.g. SO₂, CO, H₂S, NH₃, and NO_x (NO and NO₂). For that purpose, conductometric gas dosimeters are an interesting alternative to conventional gas sensors. Compared to classical gas sensors, gas dosimeters enable to detect the total amount or dose of the analyte directly by accumulation of gas molecules, which can be read out electrically. Even the actual analyte concentration can be - additionally - obtained by the derivative of the time-dependent sensor signal.^{1,2}

The sensing principle of gas dosimeters is based on the selective accumulation of analyte gas molecules in the sensor layer, causing a concomitant analyte level-dependent change of the electrical properties of the sensing material. Gas dosimeters are suitable for a reliable long-term detection of lowest analyte concentrations below 10 ppm.³ The operation of a gas dosimeter consists of two phases: the sensing period and the regeneration period. During the sensing period, under sorption conditions, analyte molecules accumulate irreversibly in the sensitive layer, yielding a change of the sensor signal (conductance or resistance change) with a concentration-dependent slope. In case of saturation effects of the signal, the sensitive material has to be regenerated either by chemical reactions^{2,4}, elevated temperatures^{5,6}, or optical methods^{4,7}. If the dosimeter is applied as single-use device it has to be replaced. The dosimeter principle enables a direct detection of the analyte amount, which is in accordance with international and national environmental immission or emission regulation limits, which are

often given as mean time values. Factors influencing the sensing behavior and the sensor signal of gas dosimeters are, e.g., temperature^{6,8}, thickness of the sensitive layer⁹ and sensor set up.¹⁰

Suitable materials for the application as sensitive layer are, for example, metal oxides, carbon nanotubes and (semi)conducting polymers, changing their electrical properties during exposure to the analyte gas.¹ Polymer-based gas sensing devices are a low-cost alternative to classical gas sensors and, moreover, they can be operated at room temperature. Therefore, with the combination of the dosimeter principle and an organic semiconducting polymer as sensitive layer a highly sensitive and reliable detection of lowest analyte concentrations can be achieved.

Organic semiconducting polymers are well known for application as active sensor materials. Advantageous is their unique film forming behavior in combination with the possibility for low mass cost production by simple printing techniques. Furthermore, the variety of chemical and structural compositions enables to tailor materials with accurately adjusted properties.^{11,12} Thus, organic semiconducting polymers were applied in organic field effect transistor (OFET) sensors.¹³ Especially, p-type semiconductors, e. g. poly(3-hexylthiophene) or poly(pyrrole), are suitable for the detection of NO₂. This is due to the oxidizing ability of NO₂ leading to acceptor doping of the polymer semiconductor, which causes a change of the electrical properties.^{14,15} Also, poly(tetraphenylbenzidine)s (PTPDs) were successfully applied for NO₂ sensing in OFETs.¹⁶ It was shown in the literature that in an OFET setup the sensing mechanism is based on trapped charge carriers that are located at the gate dielectric.^{17,18} PTPDs are well known hole conductors for the use in organic light emitting diodes, organic photovoltaics or OFETs. Their excellent physical, photochemical, and electrochemical properties are advantageous for these applications.¹⁹

In this letter, we show the poly(TPD) derivative, poly[*N,N'*-bis(4-(2-ethylhexyloxy)phenyl)-*N,N'*-di-*para*-tolylbiphenyl-4,4'-diamine] (PTPD), as a promising material for the application in an impedimetric NO_x gas dosimeter. Furthermore, PTPD was doped with the Co(III)-complex, tris(1-(pyridin-2-yl)-1*H*-pyrazol)cobalt(III) tris(hexafluorophosphate), and the conducting salt lithium bis(trifluoromethanesulfonyl)imide was used. PTPD in combination with doping with a Co(III)-complex and the addition of a conducting lithium salt acts as active material in a NO₂ dosimeter, whereas without doping and the Li-salt the PTPD shows a classical sensor behavior for NO₂. This composition, Co(III)-doping and conducting salt, was shown to be efficient to increase the conductivity of PTPD.²⁰ In the following, this composition is abbreviated "additivated PTPD".

II. Experimental

The synthesis of poly[*N,N'*-bis(4-(2-ethylhexyloxy)phenyl)-*N,N'*-di-*para*-tolylbiphenyl-4,4'-diamine] PTPD and a detailed investigation of the charge transport properties is described elsewhere.²¹ The polymer used in this study has a number average molecular weight of 7820 g mol⁻¹, a weight average molecular weight of 13550 g mol⁻¹, and a polydispersity index (PDI) of 1.70. Tris(1-(pyridin-2-yl)-1*H*-pyrazol)cobalt(III) tris(hexafluorophosphate) was synthesized according to the literature.²² Lithium bis(trifluoromethanesulfonyl)imide was purchased from Aldrich.

The experimental set up of the PTPD based gas dosimeters consists of planar Al₂O₃ substrates with screen printed interdigitated gold electrodes (line-to-space ratio = 100 μm) with a thin polymer layer that was coated by doctor blading from 3 wt.% chlorobenzene solutions at 70 °C. For the additivated PTPD, 12 wt.% Co(III)-complex, 8 wt.% Li-salt both dissolved in acetonitrile, and *tert*-butylpyridine as co-solvent were added to the PTPD solution. The thicknesses of all films were around 80 nm. The sensing device was placed into a gas test bench and connected to an impedance analyzer (Alpha-A High Performance Frequency Analyzer, Novocontrol). The measurements were carried out at room temperature and at a fixed frequency $f = 10$ Hz and a voltage amplitude $U_{\text{rms}} = 100$ mV in nitrogen gas flow with a constant flow rate of 200 ml min⁻¹. NO and NO₂ was dosed in concentration from 5 to 20 ppm and in alternating pulses and a subsequent N₂ purging of 100 s each.

III. Results and Discussion

The complex impedance of an undoped and additivated PTPD film was measured as mentioned above. From the absolute value of the impedance $|Z|$ and the phase angle φ , the resistance R can be calculated by Eq. (1).

$$R = |Z| \times (1/\cos \varphi) \quad (1)$$

The conductance $G = R^{-1}$ was chosen as the sensor signal. It is plotted in Fig. 1 over the time t .

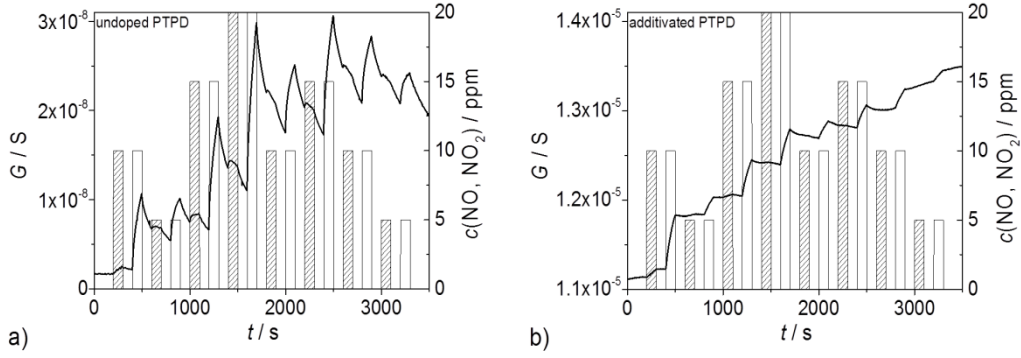


FIG. 1. Conductance G of a) the undoped PTPD film and b) additivated PTPD film during NO and NO_2 dosing over time t . The concentration of NO is represented by the hatched areas, the concentration of NO_2 by the blank areas.

In the case of the undoped PTPD, the sensor signal increases during exposure to NO_x . This sensor response is due to the interaction of the analyte with the undoped PTPD. Evidently, the conductance is increased, which is caused by the higher conductivity of the PTPD after exposure to NO_x . The mechanism behind the enhanced conductivity is based on the oxidation of the polymer by NO_2 involving radical cations of the polymer and NO_2^- anions (see also supporting information).¹⁵ In absence of the analyte NO_x , the sensor signal of the undoped sample shows a certain recovery (Fig. 1a). For the additivated PTPD, a similar response to NO_x is visible (Fig. 1b). However, the conductance G is orders of magnitudes higher compared to the undoped PTPD, making electric measurement circuitry easier. Except for the first NO pulse, the reaction of the additivated PTPD film toward NO is negligible and the device is only sensitive to NO_x exposure. Surprisingly, the additivated PTPD device shows only a weak recovery, resulting in the desired dosimeter behavior. This might be explained by the Co(III) -doping which is used for the additivated PTPD. The doping leads to the formation of radical cations. Evidently, this has a strong influence on the adsorption and desorption of NO_x during the interaction with PTPD.

The slope of the conductance course does not depend linearly on the NO_2 concentration, resulting in a non-linear characteristic line for both dosimeter devices. This is caused by saturation effects of the sensor signal. The total NO_2 dose A_{NO_2} can be calculated by integration of the NO_2 concentration c_{NO_2} over time (Eq. 2).^{1,2} In Fig. 2a) the sensor signal G vs. A_{NO_2} is depicted.

$$A_{\text{NO}_2}(t) = \int_0^t c_{\text{NO}_2}(\tilde{t}) d\tilde{t} \quad (2)$$

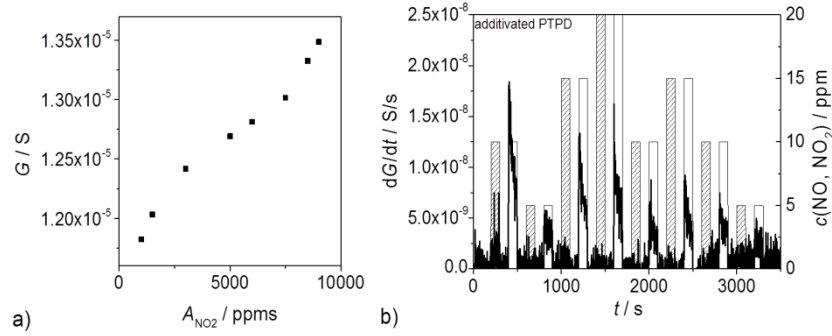


FIG. 2. a) Characteristic line given as the conductance G over the total NO_2 amount A_{NO_2} for the additivated PTPD device. b) Time derivative of the conductance dG/dt of the additivated PTPD device during NO and NO_2 dosing over time t . The concentration of NO dosing is represented by the hatched areas, the concentration of NO_2 dosing by the blank areas.

One can observe a linear course up to a total NO_2 dose of only 1500 ppms, for higher doses, no linear correlation with the conductance is given anymore. In order to investigate this behavior in more detail, Fig. 2 b) gives the time derivative of the conductance dG/dt of the additivated PTPD device. Obviously, the sensor can clearly distinguish between NO and NO_2 . The time derivative dG/dt follows the actual NO_2 concentration. The sharp peak at the beginning is a drawback. However, it needs to be excluded that an erroneous gas dosing is responsible for this unwanted behavior. The determination of the characteristic line of undoped PTPD was not possible due to the strong recovery of the sensor signal.

IV. Conclusion and Outlook

In conclusion, we have shown that PTPD is a promising material for application as NO_2 sensitive layers in gas dosimeters. In combination with additives, Co(III)-complex and Li-salt, which increase the conductivity of the sensing layer, it was possible to improve the recovery of the signal strongly. In further measurements, the investigation of the sensor signal towards lower NO_x concentrations has to be conducted, due to saturation effects in the above shown results. It is also required to test the suitability of this material for air quality monitoring. The determination of the actual NO_2 concentration was only partly possible since the sensor characteristic is not completely linear and probably also because of imperfections of the gas dosing unit.

Acknowledgement

R. M. and I. M. thank the German Research Foundation (DFG) for supporting this work under grant number MO 1060/15-1. M.T. and K.N. acknowledge the Deutsche Forschungsgemeinschaft (Graduate School GRK 1640) for financial support and K. N. thanks the Universität Bayern e.V. for the financial support in form of a scholarship of the Bayerische Graduiertenförderung and the Elitenetzwerk Bayern (ENB).

REFERENCES

- ¹I. Marr, A. Groß, R. Moos, *J. Sens. Sens. Syst.* 3, 29 (2014), <http://dx.doi.org/10.5194/jsss-3-29-2014>
- ²A. Groß, G. Beulertz, I. Marr, D.J. Kubinski, J.H. Visser, R. Moos, *Sensors* 12, 2831 (2012), <http://dx.doi.org/10.3390/s120302831>
- ³A. Groß, M. Kremling, I. Marr, D.J. Kubinski, J.H. Visser, H.L. Tuller, R. Moos, *Sensors* 13, 4428 (2013), <http://dx.doi.org/10.3390/s130404428>
- ⁴A. Helwig, G. Müller, J. A. Garrido, M. Eickhoff, *Sensors and Actuators B* 133, 156 (2008), <http://dx.doi.org/10.1016/j.snb.2008.02.007>
- ⁵D. J. Kubinski, J. H. Visser, *Sensor. Actuator. B: Chemical*, 130, 425 (2008), <http://dx.doi.org/10.1016/j.snb.2007.09.007>
- ⁶A. Brandenburg, J. Kita, A. Groß, R. Moos, *Sensors and Actuators B* 189, 80 (2013), <http://dx.doi.org/10.1016/j.snb.2012.12.119>
- ⁷J. Li, Y. Lu, Q. Ye, M. Cinke, J. Han, M. Meyyappan, *Nano Letters* 3, 929 (2003), <http://dx.doi.org/10.1021/nl034220x>
- ⁸A.-M. Andringa, N. Vlietstra, E. C. P. Smits, M.-J. Spijkman, H. L. Gomes, J. H. Klootwijk, P. W. M. Blom, D. M. de Leeuw, *Sensors and Actuators B* 171-172, 1172 (2012), <http://dx.doi.org/10.1016/j.snb.2012.06.062>
- ⁹A. Groß, M. Richter, D. J. Kubinski, J. H. Visser, R. Moos, *Sensors* 12, 12329 (2012), <http://dx.doi.org/10.3390/s120912329>
- ¹⁰G. Beulertz, A. Groß, R. Moos, D. J. Kubinski, J. H. Visser, *Sensors and Actuators B* 175, 157 (2012), <http://dx.doi.org/10.1016/j.snb.2012.02.017>

- ¹¹M. Thelakkat, *Macromol. Mater. Eng.* 287, 442 (2002), [http://dx.doi.org/10.1002/1439-2054\(20020701\)287:7<442::AID-MAME442>3.0.CO;2-H](http://dx.doi.org/10.1002/1439-2054(20020701)287:7<442::AID-MAME442>3.0.CO;2-H)
- ¹² M. E. Roberts, A. N. Sokolov, Z. Bao, *J. Mater. Chem.* 19, 3351 (2009), <http://dx.doi.org/10.1039/b816386c>
- ¹³A.-M. Andringa, C. Piliago, I. Katsouras, P. W. M. Blom, D. M. de Leeuw, *Chem. Mater.* 26, 773 (2014), <http://dx.doi.org/10.1021/cm4020628>
- ¹⁴A. Assadi, A. Spetz, M. Willander, C. Svensson, I. Lundström, O. Inganäs, *Sensors and Actuators B* 20, 71 (1994), [http://dx.doi.org/10.1016/0925-4005\(93\)01171-Y](http://dx.doi.org/10.1016/0925-4005(93)01171-Y)
- ¹⁵T. Hanawa, S. Kuwabata, H. Yoneyama, *J. Chem. Soc., Faraday Trans. 1* 84, 1587 (1988), <http://dx.doi.org/10.1039/F19888401587>
- ¹⁶A. Das, R. Dost, T. Richardson, M. Grell, J. J. Morrison, M. L. Turner, *Adv. Mater.* 19, 4018 (2007), <http://dx.doi.org/10.1002/adma.200701504>
- ¹⁷F. Gholamrezaie, A.-M. Andringa, W. S. C. Roelofs, A. Neuhold, M. Kemerink, P. W. M. Blom, D. M. de Leeuw, *Small* 8, 241 (2012), <http://dx.doi.org/10.1002/sml.201101467>
- ¹⁸A.-M. Andringa, W. S. C. Roelofs, M. Sommer, M. Thelakkat, M. Kemerink, D. M. de Leeuw, *Appl. Phys. Lett.* 101, 153302 (2012); <http://dx.doi.org/10.1063/1.4758697>
- ¹⁹A. Iwan, D. Sek, *Progress in Polymer Science* 36, 1277 (2011), <http://dx.doi.org/10.1016/j.progpolymsci.2011.05.001>
- ²⁰K. Neumann, M. Thelakkat, submitted to *RSC Advances* (2014)
- ²¹K. Neumann, C. Schwarz, A. Köhler, M. Thelakkat, *J. Phys. Chem. C* 118, 27 (2014), <http://dx.doi.org/10.1021/jp407014q>
- ²²J. Burschka, A. Dualeh, F. Kessler, E. Baranoff, N.-L. Cevey-Ha, C. Yi, M. K. Nazeeruddin, M. Grätzel, *J. Am. Chem. Soc.* 133, 18042 (2011), <http://dx.doi.org/10.1021/ja207367t>

Supporting Information to

Undoped and doped Poly(tetraphenylbenzidine) as Sensitive Material for an Impedimetric NO₂ Gas Dosimeter

I. Marr,¹ K. Neumann,² M. Thelakkat,² and R. Moos^{1,a)}

¹Department of Functional Materials, University of Bayreuth, Bayreuth, 95440, Germany

²Department of Macromolecular Chemistry I, Applied Functional Polymers, University of Bayreuth, Bayreuth, 95440, Germany

UV-vis spectroscopy showing the oxidative behavior of the analyte NO₂

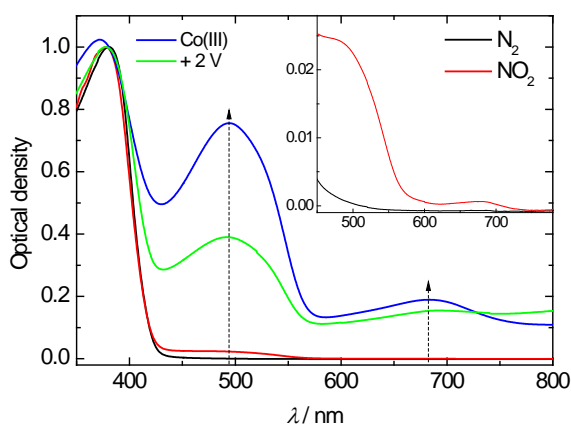


Figure 1. Uv-vis absorption spectra of undoped PTPD in THF solution (0.02 mg mL⁻¹) under nitrogen (black curve) and under exposure to NO₂ (500 ppm for 10 min, red curve). The inset shows the wavelength range from 450 to 800 nm. New absorption bands arise after exposure to NO₂ which are consistent with the absorption bands arising from oxidation with Co(III)-complex (blue curve) or electrochemical oxidation (applied potential + 2 V, green curve).

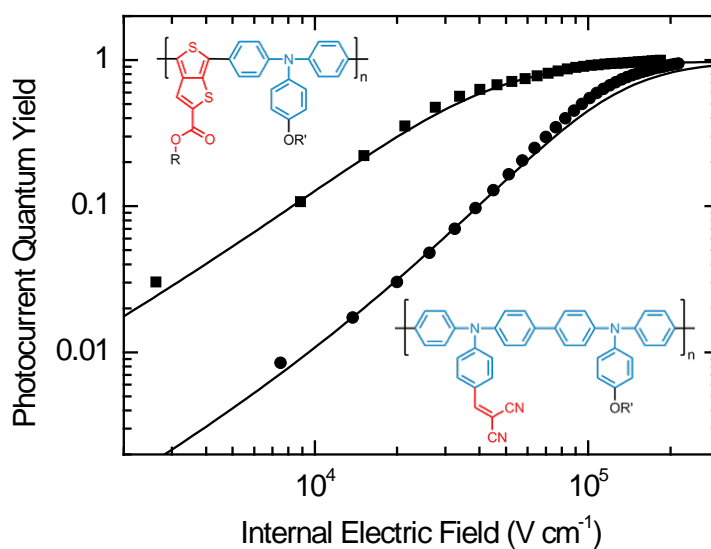
Influence of the Excited-State Charge-Transfer Character on the Exciton Dissociation in Donor–Acceptor Copolymers

Katharina Neumann,[†] Christian Schwarz,[‡] Anna Köhler,[‡] and Mukundan Thelakkat^{*,†}

[†]Applied Functional Polymers, Macromolecular Chemistry I, University of Bayreuth, 95440 Bayreuth, Germany

[‡]Experimental Physics II and Bayreuth Institute of Macromolecular Research (BIMF), University of Bayreuth, 95440 Bayreuth, Germany

*E-mail of corresponding author: mukundan.thelakkat@uni-bayreuth.de



Published in Journal of Physical Chemistry C

Reproduced with permission from *J. Phys. Chem. C*, 2014, 118 (1), pp 27–36.

Copyright 2014 American Chemical Society

ABSTRACT

We synthesize a polytriphenylamine homopolymer and two donor-acceptor copolymers (D-A - copolymers) based on triphenylamine (TPA) as donor in combination with two different acceptor moieties to study the effect of the acceptor unit on the excited-state charge-transfer characteristics (CT-characteristics) and charge separation. The two acceptor moieties are a dicyanovinyl group in the side chain and a thieno[3,4-*b*]thiophene carboxylate in the main chain. Absorption and photoluminescence studies show new CT bands for both of the D-A-copolymers. Field-dependent charge extraction studies in bilayer solar cells indicate a stronger CT-character for the copolymer in which the acceptor group is less conjugated with the copolymer backbone. The D-A-copolymer carrying the acceptor unit in the main chain exhibits smaller excitonic CT-character and good conjugation leading to less-bound electron-hole pairs and a better charge separation. This fundamental study gives insight into the interdependence of conjugation, charge carrier mobility, and solar cell performance for two different D-A-copolymers.

INTRODUCTION

There is intensive research in the field of bulk Heterojunction solar cells comprising alternating donor-acceptor copolymers (D-A-copolymers) and fullerene derivatives with the aim to design novel D-A-copolymers and thus to increase the power conversion efficiency.¹⁻³ In general, two strategies are widely used as the design principle for these D-A -copolymers: (a) introduction of the A unit as a side chain on the donor backbone and (b) incorporation of D and A in the main chain to get alternating D-A -copolymers.⁴⁻¹⁰ The diverse elementary processes and dynamics of charge transfer (CT) and charge separation in such a bulk heterojunction solar cell have been intensively studied.^{11,12} After light absorption a bound metastable intermolecular CT-state is formed by electron transfer to a neighboring molecule. This state can separate into free charge carriers or recombine. Since the charge separation is a key step, it is very important to understand the influence of conjugation and excited-state CT-character on this process. Commonly, the CT-character of the excited state between D-A-copolymer and fullerene acceptor has been investigated.¹³ It is equally important to understand and correlate the degree of excited-state CT-character of the D-A-copolymer itself with its charge carrier mobility as well as the charge separation with fullerenes. It was shown by Tautz et al. that the polaron pair yield in D-A-copolymers is dependent on the electron affinity of the acceptor moiety.¹⁴ A correlation of this observation with charge separation and device characteristics was not reported there. Furthermore, Carsten et al. showed that not only the energetics but also the internal dipole moment along the polymer chain may be critical for the CT-state, and these results were compared with charge separation in bulk Heterojunction devices.¹⁵ Here, we first correlate the

observed CT-character with the conjugation/delocalization as well as with the charge carrier mobility in the D–A-polymer itself. The observed CT-character is then compared with the charge separation in fullerene bilayer devices. We selected a well-defined bilayer device to avoid possible morphological differences in blend devices on using different polymers. Our material system consists of two novel D–A -copolymers based on triphenylamine (TPA). We chose a system containing TPA which is a widely examined and well-known donor material with excellent thermal and electrochemical stability.¹⁶ The CT-character of the excited state of DA -copolymers depends on the nature of attachment of the acceptor unit to the donor moiety. Here, we compare two different D–A -copolymers: (a) with a dicyanovinyl acceptor in the side chain (P2) and (b) with a thieno[3,4-*b*]thiophene acceptor in the main chain (P3) with the homopolymer (P1) without any acceptor unit. Since the resulting interaction between electron donating and the electron withdrawing molecules usually leads to the formation of an intramolecular CT-state,¹⁷ the two different strategies adopted here can result in different degrees of CT-character and conjugation or delocalization between the D and A moieties.

EXPERIMENTAL SECTION

Synthesis and Polymerization. P1: 4-Bromo-*N*-(4-bromophenyl)-*N*-(4-(2-ethylhexyloxy)phenyl)aniline (**1**; 516 mg, 0.97 mmol) and 4-(2-ethylhexyloxy)-*N,N*-bis(4-(4,4,5,5-tetramethyl-1,3,2-dioxaborolan-2-yl)phenyl)aniline (**2**; 607 mg, 0.972 mmol) were dissolved in 8 mL of tetrahydrofuran (THF). A 5.3 mL aliquot of 2 M K₂CO₃ in water and dimethylformamide (DMF; 1:1) were added, and the mixture was purged with argon for 30 min. Pd(PPh₃)₄ (45 mg, 0.04 mmol) and Pd(OAc)₂ (4 mg, 0.02 mmol) were added, and the reaction mixture was heated to 70 °C. After 72 h the polymerization was end-capped by the addition of phenylboronic acid pinacol ester and bromobenzene for 3 h. After cooling, the reaction mixture was extracted with dichloromethane (DCM) and water. The crude product poly[*N,N'*-bis(4-(2-ethylhexyloxy)phenyl)-*N,N'*-di-*p*-tolylbiphenyl-4,4'-diamine] (**P1**) was precipitated in MeOH and purified by sequential Soxhlet extraction in MeOH and EtOH. Yield: 66%.

¹H NMR (300 MHz, CDCl₃, 298 K; ppm): δ 7.51–7.36 (d, 2H, H_{ar}), 7.18–6.99 (d, 2H, H_{ar}), 6.93–6.81 (m, 6H, H_{ar}), 3.83 (d, 2H, O–CH₂), 1.80–1.66 (m, 1H, CH), 1.60–1.39 (m, 8H, CH₂), 1.34 (s, 12 H, CH₃), 0.97–0.84 (m, 6H, CH₃).

P2: First, an aldehyde functionalized copolymer was synthesized as precursor. For that, 4-(bis(4-bromophenyl)-amino)benzaldehyde (0.79 g, 1.83 mmol) and **2** (1.15 g, 1.83 mmol) were dissolved in 15 mL of THF. After addition of 2.33 mL of 2 M K₂CO₃ in water and DMF (1:1), the mixture was degassed. A 20 mg (0.017 mmol) amount of Pd(PPh₃)₄ and 2 mg (0.009 mmol) of Pd(OAc)₂ were added, and the reaction mixture was heated to 70 °C. After 5 days, phenylboronic

acid pinacol ester and bromobenzene were added for end-capping and the mixture was stirred for 3 h. The reaction mixture was cooled to room temperature and extracted with dichloromethane (DCM) and brine. The organic phase was dried over Na₂SO₄, and the solvent was evaporated under reduced pressure. The dark brown residue was dissolved in THF, and a small amount of the scavenger *N,N*-diethylphenylazothioformamide was added. After 3 h at room temperature the polymer was precipitated in MeOH followed by a Soxhlet extraction in EtOH for 12 h. Poly[4-((4'-((4-(2-ethylhexyloxy)phenyl)(p-tolyl)amino)biphenyl-4-yl)(p-tolyl)-amino)benzaldehyde] was obtained as beige powder. Yield: 70%.

¹H NMR (300 MHz, CDCl₃, 298 K; ppm): δ 9.83 (s, 1H, CHO), 7.84–7.64 (s, 2H, H_{ar}), 7.64–7.34 (m, 4H, H_{ar}), 7.23–6.95 (m, H_{ar}), 6.95–6.64 (s, H_{ar}), 3.93–3.67 (d, 2H, O–CH₂), 1.85–1.62 (m, 1H, CH), 1.59–1.37 (m, 8H, CH₂), 1.34 (s, 12H, CH₃), 0.91 (s, 6H, CH₃). IR (cm⁻¹): ν 2915 (s), 2842 (s), 1692 (m), 1588 (m), 1488 (m), 1469 (s), 1263 (m), 1161 (m), 1109 (m), 816 (m), 718 (s).

Second, the precursor copolymer poly[4-((4'-((4-(2-ethylhexyloxy)phenyl)(p-tolyl)amino)biphenyl-4-yl)(p-tolyl)-amino)benzaldehyde] (736 mg, 1.14 mmol) was dissolved in 9 mL of pyridine and 2 mL of acetic acid. After purging with argon for 30 min, malonodinitrile (2 mg, 0.24 mmol) and one crystal of NH₄OAc were added and the solution was stirred for 70 h at room temperature. The reaction mixture was extracted with DCM and water. The organic phase was washed with water and dried over Na₂SO₄. After evaporation of the solvent under reduced pressure, the polymer was precipitated from THF in MeOH. 2-(4-((4'-((4-(2-Ethylhexyloxy)phenyl)(ptolyl)amino)biphenyl-4-yl)(p-tolyl)amino)benzylidene)-malonodinitrile (**P2**) was obtained as dark red powder. Yield: 98%.

¹H NMR (300 MHz, CDCl₃, 298 K; ppm): δ 7.87–7.67 (m, 2H, H_{ar}), 7.56 (s, 1H, H_{vinyl}), 7.52–7.33 (m, 4H, H_{ar}), 7.20–6.92 (m, 10H, H_{ar}), 6.92–6.56 (m, 2H, H_{ar}), 3.93–3.67 (d, 2H, OCH₂), 1.81–1.58 (m, 1H, CH), 1.58–1.37 (m, 8H, CH₂), 0.95–0.73 (m, 6H, CH₃). IR [cm⁻¹]: ν 2927 (m), 2222 (m), 1567 (m), 1487 (s), 1237 (m), 1181 (m), 1112 (m), 817 (s), 696 (m). **P3**: Compound **2** (590 mg, 0.94 mmol) and 4-bromothiophene-3-carbaldehyde (**4**; 429 mg, 0.94 mmol) were dissolved in 8 mL of THF. A 5 mL aliquot of 2 M K₂CO₃ in water and DMF (1:1) were added, and the mixture was purged with argon for 30 min. Then Pd(PPh₃)₄ (22 mg, 0.02 mmol) and Pd(OAc)₂ (2 mg, 0.01 mmol) were added, and the reaction mixture was heated to 70 °C in a microwave. After 5 h the reaction mixture was extracted with DCM and water. The crude product poly[octyl-6-(4-((4-(2-ethylhexyloxy)-phenyl)(p-tolyl)amino)phenyl)-alt-4-octylthieno[3,4-b]-thiophene-2-carboxylate] (**P3**) was precipitated in MeOH and purified by Soxhlet extraction in EtOH and acetone. Yield: 40%.

¹H NMR (300 MHz, CDCl₃, 298 K; ppm): δ 8.07 (s, 1H, H_{ar}), 7.68–7.40 (m, 4H, H_{ar}), 7.25–7.02 (m, 6H, H_{ar}), 7.02–6.72 (m, 2H, H_{ar}), 4.47–4.19 (d, 2H, OCH₂), 4.02–3.72 (d, 2H, OCH₂), 1.88–1.68 (m, 1H, CH), 1.68–1.12 (m, 26H, CH₂), 1.10–0.72 (m, 9H, CH₃).

Physical Measurements. Number-average (M_n) and weight-average (M_w) molecular weights were determined by size exclusion chromatography (SEC) using a Waters 515-HPLC pump with stabilized THF as the eluent. The flow rate was 0.5 mL min^{-1} . The column setup consisted of a guard column (Varian; $50 \times 0.75 \text{ cm}$; ResiPore; particle size, $3 \mu\text{m}$) and two separation columns (Varian; $300 \times 0.75 \text{ cm}$; ResiPore; particle size, $3 \mu\text{m}$). The compounds were monitored with a Waters UV detector at 254 nm. SEC in chlorobenzene was carried out at $60 \text{ }^\circ\text{C}$ on an Agilent 1100 series SEC using two Polymer Laboratories mixed B columns. Both SEC systems were calibrated against polystyrene. Thermogravimetric analysis (TGA) measurements were carried out using a Mettler Toledo TGA/SDTA 851e with a heating rate of $40 \text{ }^\circ\text{C min}^{-1}$ under nitrogen flow, and the temperature of degradation (T_d) corresponds to a 5% weight loss. Differential scanning calorimetry (DSC) analysis was performed on a Perkin-Elmer Diamond differential scanning calorimeter, calibrated with indium. Glass transition temperature (T_g) was determined using a scanning rate of $20 \text{ }^\circ\text{C min}^{-1}$ under a nitrogen flow. Cyclic voltammograms (CVs) were recorded under moisture- and oxygen-free conditions using a standard three-electrode assembly connected to a potentiostat (model 263A, EG&G Princeton Applied Research) and at a scanning rate of 50 mV s^{-1} . The working electrode was a glassy carbon disk electrode (area, $1/4 \times 0.0314 \text{ cm}^2$), a platinum wire was used as auxiliary electrode, and the quasi-reference electrode was Ag/Ag⁺ composed of a Ag wire and AgNO₃ in acetonitrile. Tetrabutylammonium hexafluorophosphate (Bu₄NPF₆, 0.1 M) was used as the conducting salt. Each measurement was calibrated with an internal standard (ferrocene/ferrocenium). The HOMO values were determined from the value of -5.16 eV for ferrocene with respect to vacuum level and correcting for the solvent effects. For spectroscopic measurements polymer films were spincoated from filtered chlorobenzene solutions (10 mg mL^{-1}). Solution measurements were also performed in chlorobenzene with a concentration of the repetition units of 10^{-5} – $10^{-3} \text{ mol L}^{-1}$. Absorption was measured with a Cary 5000 (Varian) UV-vis spectrometer. The fluorescence quantum yields were measured in an integration sphere filled with nitrogen under illumination with an Ar⁺ laser (**P1**, UV-multiline 351 nm/364 nm; **P2** and **P3**, 488 nm) with a charge-coupled-device (CCD) camera as described elsewhere.¹⁸ The fluorescence spectra were recorded on a time-correlated single photon counting (TCSPC) setup at room temperature with the samples in vacuum under excitation from a laser diode (**P1**, 375 nm; **P2** and **P3**, 485 nm). Electric devices were fabricated on structured ITO-coated glass substrates using AZ 1518 photopaint from Microchemicals to define the active area and to prevent edge effects. The devices were then plasma-edged, and a 50 nm layer of poly(3,4-ethylenedioxythiophene):poly(styrene-sulfonate) (PEDOT:PSS; Clevios) was spin-coated into the active area. The PEDOT:PSS layer was heated to $180 \text{ }^\circ\text{C}$ for 30 min, followed by spin-coating a 40 nm polymer layer on top of it for the bilayer solar cells. Then a 40 nm C60 layer (99.9% purity, American Dye Source Inc.) and a 100 nm aluminum layer were evaporated at $5 \times 10^{-7} \text{ mbar}$. For the space-charge-limited current (SCLC)

devices, the polymers were blade-coated from chlorobenzene solutions and a 40 nm gold electrode was evaporated. All device measurements were performed under active vacuum at room temperature with a Keithley source measure unit. For performance and field-dependent measurements a Newport 1.5 AM solar simulator was used, and the solar spectrum measurements were recorded under monochromatic illumination of a 150 W xenon lamp. Light intensities were recorded with a Hamamatsu S1337-33BQ photodiode. The internal field F was calculated as $F = (V_{oc} - V)/d$ with applied external voltage V , the open-circuit voltage V_{oc} , and the active film thickness d .

RESULTS

Synthesis

Here, we present the synthesis and characterization of a main chain homopolymer (**P1**, poly-[*N,N'*-bis(4-(2-ethylhexyloxy)phenyl)-*N,N'*-di-*p*-tolylbiphenyl-4,4'-diamine]), an alternating D-A-copolymer with dicyanovinyl in the side chain (**P2**, poly[2-(4-((4'-((4-(2-ethylhexyloxy)phenyl)(*p*-tolyl)amino)biphenyl-4-yl)-alt-(*p*-tolyl)amino)benzylidene)malononitrile]) and the A D -copolymer carrying thieno[3,4-*b*]thiophene-2-carboxylate in the main chain (**P3**, poly[octyl-6-(4-((4-(2-ethylhexyloxy)phenyl)(*p*-tolyl)amino)phenyl)-alt-4-octylthieno[3,4-*b*]thiophene-2-carboxylate]). The dicyanovinyl group is strongly electron withdrawing. It has been shown that the introduction of this group as a side chain lowers the optical gap, by mainly lowering the LUMO value.¹⁰ On the other hand, the electron withdrawing comonomer thieno[3,4-*b*]thiophene carboxylate stabilizes the quinoidal form and therefore lowers the optical gap when coupled with a suitable donor comonomer.^{19,20} We used Suzuki AA/BB type polycondensation as a synthetic method to obtain the conjugated polymers²¹ because it enables the synthesis of well-defined alternating copolymers. The symmetrically difunctionalized monomers were synthesized according to the literature with good yields (see the Supporting Information).^{22,23} Homopolymer **P1** was obtained by polycondensation between a dibromo-TPA and a TPA bis-boronic acid ester (Figure 1). The synthesis of **P2** was realized by a precursor method. We used monomer **3**, a dibromo-TPA with an aldehyde group which is stable under Suzuki polycondensation conditions, and polymerized it with the common bis-boronic acid ester monomer **2**. After purifying the precursor copolymer by Soxhlet extraction, the dicyanovinyl group was introduced via a polymer analogous Knoevenagel condensation with malonodinitrile. ¹H NMR spectroscopy and FT-IR spectroscopy clearly proved the complete conversion of the aldehyde functionality to the dicyanovinyl group (see the Supporting Information). The alternating main chain D A -copolymer **P3** was synthesized by reacting directly the dibromo-

monomer thieno-[3,4-*b*]thiophene carboxylate **4** with monomer **2** under microwave irradiation. All polymers were soluble in THF, CHCl₃, and chlorobenzene, whereas **P3** was soluble only in CHCl₃ and chlorobenzene.

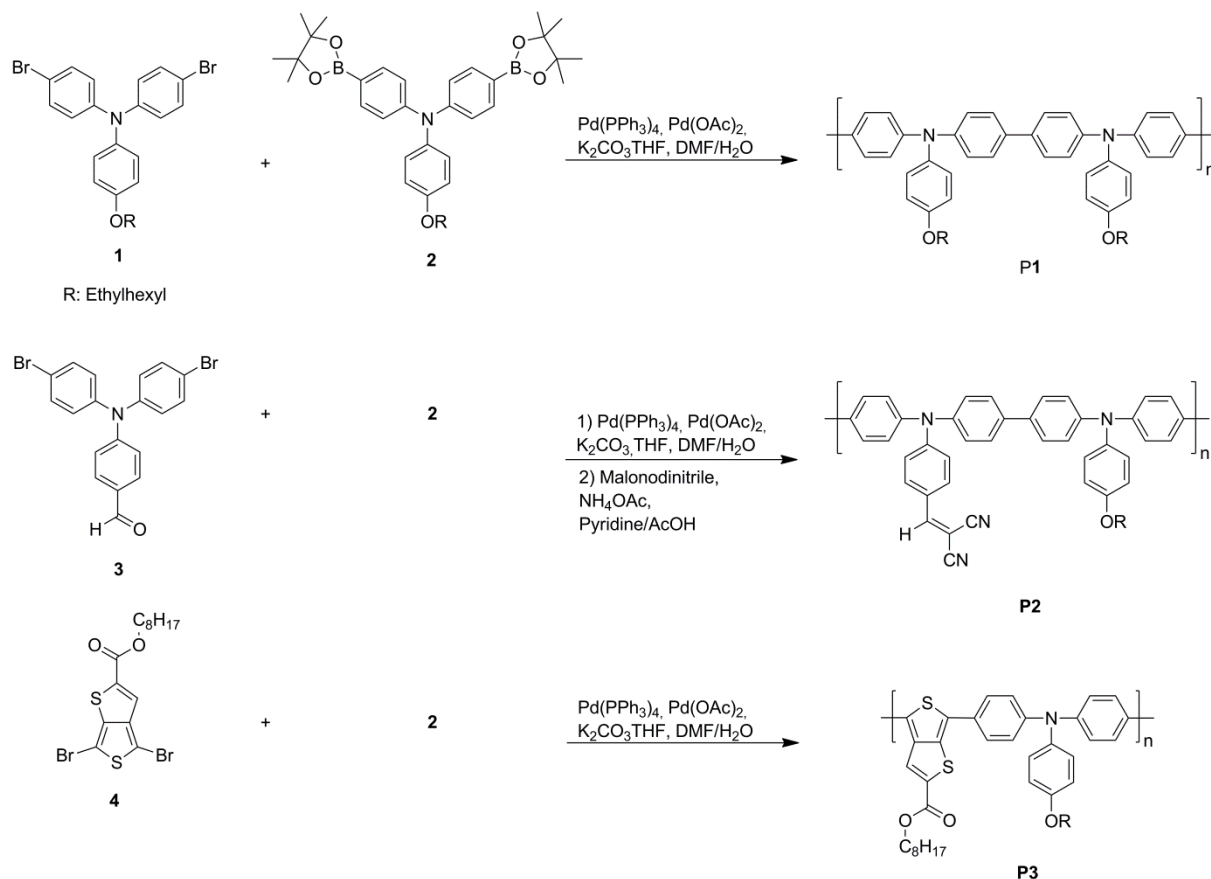


Figure 1. Scheme of the synthesis of the polymers **P1**, **P2** and **P3** *via* Suzuki polycondensation. The bis-boronic ester monomer **2** was reacted with the three different dibrominated monomers **1**, **3** and **4**. The polycondensation of **P3** was carried out under microwave irradiation.

Polymer Properties

M_w and M_n of polymers **P1**, **P2**, and **P3** were determined by SEC with THF as eluent. For calibration a polystyrene standard was used. Copolymer **P3** was analyzed in a chlorobenzene SEC at 60 °C due to the low solubility in THF. Homopolymer **P1** has a M_n of 10330 g mol⁻¹ and a M_w of 15770 g mol⁻¹. Both D-A-copolymers show a comparable M_n with 7400 and 7770 g mol⁻¹ for **P2** and **P3**, respectively. The corresponding M_w are 18760 g mol⁻¹ and 11610 g mol⁻¹, and all of the relevant SEC data are given in Table 1. The homopolymer and all copolymers showed high thermal stability in TGA with temperatures for 5% weight loss ranging from 402 to 410 °C. All of the polymers form optically clear and smooth films, which is advantageous for device

preparation. DSC analysis showed that all compounds were amorphous and had glass transition temperatures of 203, 212 and 118 °C for **P1**, **P2**, and **P3**, respectively.

Table 1. Molecular Weights and Thermal Properties of the Homopolymer P1 and the D-A-Copolymers P2 and P3.^a

Polymer	M_n (g mol ⁻¹)	M_w (g mol ⁻¹)	PDI	$T_{5\%}$ (°C)	T_g (°C)
P1	10330	15770	1.52	402	203
P2	7400	18760	2.54	410	212
P3	7770	11610	4.91	370	118

^aSEC analysis was carried out in THF as eluent and polystyrene standards at room temperature. **P3** was measured in chlorobenzene at 60 °C.

Cyclic voltammetry measurements were employed to investigate the redox behavior and the influence of the different electron withdrawing groups on the HOMO/LUMO levels. The HOMO values were calculated by calibrating with ferrocene and correcting for solvent effects.^{24,25} The polymers were measured in DCM vs AgNO₃. **P1** and **P3** have similar oxidation potential values (0.15 V vs Fc), whereas the oxidation potential of **P2** is slightly higher (0.3 V vs Fc). Thus, the calculated HOMO levels are -5.31, -5.45, and -5.30 eV for P1, P2, and P3, respectively. The values are summarized in Table 2. The LUMO levels were estimated from the optical gap (determined from the onset of absorption bands, vide infra) and the HOMO energy values. Due to the slightly lower optical gap of **P3** the LUMO levels of both D-A-copolymers are similar. Thus, the introduction of the strong electron withdrawing dicyanovinyl acceptor unit as substituent reduces the electron richness and delocalization of the TPA main chain, resulting in an increased oxidation potential by about 0.14 V. Additionally, the redox potential is drastically lowered, resulting in low LUMO values. However, the incorporation of the thieno[3,4-*b*]thiophene acceptor unit in the main chain does not affect the oxidation potential, indicating a similar oxidizability or delocalization of the main chain as in the homopolymer **P1**. This means that the thieno[3,4-*b*]thiophene carboxylate does not withdraw electrons from the TPA moiety but maintains the conjugation between two TPA units resulting in the same oxidation potential for both **P3** and **P1**. This conclusion can be derived from the fact that an individual TPA unit exhibits an oxidation potential of about 0.2 eV higher than that for a dimer in which the TPA units are in conjugation.¹⁶ A further relevant parameter for semiconductor materials is the charge carrier mobility. We investigated the hole transport mobilities (μ_h) of the three polymers

in hole-only diodes using the SCLC method. This method allows the determination of the bulk charge carrier mobility. A PEDOT:PSS-coated ITO electrode and a gold electrode were used to fabricate the devices. In this case, PEDOT:PSS serves as a hole-injecting electrode. Furthermore, the high work function of the gold electrode hinders the injection of electrons but allows for hole collection. Therefore, the transport of the holes is only limited by the charge carrier mobility of the polymer and can be described by the Mott–Gurney eq 1.²⁶

$$J = \frac{9}{8} \varepsilon \varepsilon_0 \mu_h \frac{V^2}{L^3} \quad (1)$$

According to this equation the current density J is dependent on the permittivity of free space ε_0 , the dielectric constant of the polymer ε (assumed to be 3), the charge carrier mobility μ_h , the thickness of the polymer layer L , and the voltage drop across the device V . Assuming ohmic contacts to the injecting electrode, the current is spacecharge -limited at high voltages. The measured I - V curves were fitted according to eq 1 to obtain the hole transport mobility μ_h . By recording different active layer thicknesses, the thickness scaling of the spacecharge -limited currents was verified. The log-log plots of J vs L and the fits according to the relation $J \sim V^2/L^3$ are illustrated in the Supporting Information. This clearly indicates that the measured current is space-charge-limited. The contact resistance and series resistance were measured in a reference device without a polymer layer, and the corresponding voltage drop V_r was subtracted from the applied voltage. The built-in potential V_{bi} for PEDOT:PSS and gold is estimated to be 0 V. Figure 2 gives the half-log plots of J vs V of the three polymers at similar layer thicknesses and the device geometry.

Table 2. a) HOMO Values of P1, P2, and P3 Obtained from Oxidation Potential E_{ox} vs Ferrocene in Cyclic Voltammetry Measurements at 50 mV s^{-1} in DCM with 0.1 M Tetrabutylammonium Hexafluorophosphate^a and b) Hole Transport Mobilities (μ_h) Determined by SCLC measurements in Hole-Only devices with PEDOT:PSS and Au as Electrodes.^b

Polymer	E_{ox} vs. Fc (V)	HOMO (eV)	E_g (eV)	LUMO (eV)	μ_h ($\text{cm}^2 \text{V}^{-1} \text{s}^{-1}$)
P1	0.15	-5.31	2.97	-2.34	1.4×10^{-4}
P2	0.29	-5.45	2.24	-3.21	7.6×10^{-5}
P3	0.14	-5.30	2.10	-3.20	3.1×10^{-4}

^aThe HOMO value for ferrocene/ferrocenium oxidation in DCM was taken as -5.16 eV.²⁵ LUMO values were estimated using the onset of absorption (E_g) from UV-VIS measurements and corresponding HOMO values. ^bGiven values are the average values of the three different measured thicknesses.

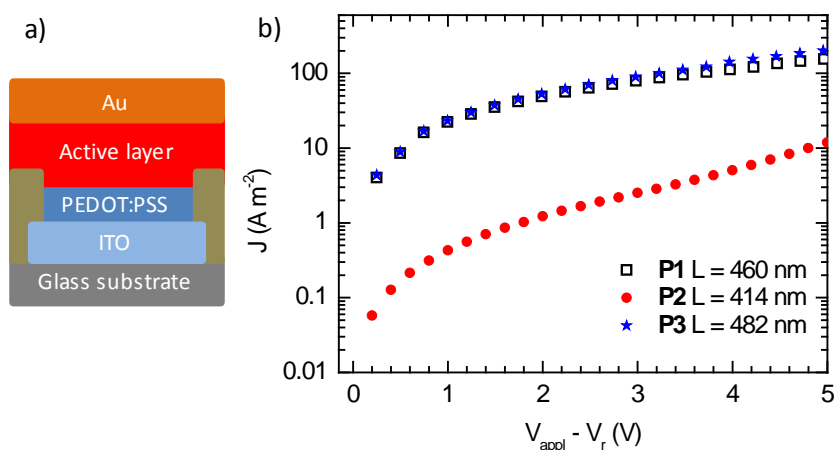


Figure 2. a) Schematic structure of a hole-only device with PEDOT:PSS and gold as electrodes. b) Half-log plot of current density J vs voltage V of **P1**, **P2** and **P3** for comparable layer thicknesses. Additional measurements for different layer thicknesses are given in the Supporting Information.

We found that the homopolymer **P1** shows a hole transport mobility of $1.4 \times 10^{-4} \text{ cm}^2 \text{ V}^{-1} \text{ s}^{-1}$. The introduction of the dicyanovinyl groups leads to a decrease of 1 order of magnitude, $7.6 \times 10^{-5} \text{ cm}^2 \text{ V}^{-1} \text{ s}^{-1}$, for **P2**. The low mobility of **P2** indicates that the side chain acceptor unit does affect the delocalization or conjugation of the TPA main chain. However, the incorporation of the thieno[3,4-*b*]thiophenecarboxylate does not change the hole transport mobility considerably for **P3** ($\mu_h = 3.1 \times 10^{-4} \text{ cm}^2 \text{ V}^{-1} \text{ s}^{-1}$). These hole transport mobility values are in full agreement with the influence of the acceptor units on the delocalization or the easiness of the oxidation as observed in cyclic voltammetry.

Absorption and Photoluminescence Spectroscopy

The absorption spectra of **P1**, **P2**, and **P3** in solution and film are shown in Figure 3. We first consider the solution spectra which were recorded at a concentration of the repetition units of $10^{-4} \text{ mol L}^{-1}$. Identical spectra were found at a concentration of $10^{-5} \text{ mol L}^{-1}$ with a reduced signal-to-noise ratio. For the homopolymer **P1** we observe an absorption band in the high-energy region centered at 3.22 eV that is characteristic for TPAs and that is assigned to a $\pi\pi^*$ -

transition. For copolymer **P2** containing the pendant dicyanovinyl group, we find a lower energy absorption peak centered at 2.66 eV with lower oscillator strength that appears in addition to the original TPA absorption band. The latter is blue-shifted by 100 meV to 3.32 eV and has a slightly decreased oscillator strength compared to the homopolymer **P1**. On the basis of the low oscillator strength and low energy, we attribute the 2.66 eV absorption peak present in dilute solution to an intramolecular CT-transition with low wave function overlap from the donor backbone to the dicyanovinyl in the side chain. A similar absorption behavior was also shown for other D-A copolymers.¹⁰ Overall, the copolymer **P2** is able to cover the whole low- and middle-wavelength region of the visible spectrum.

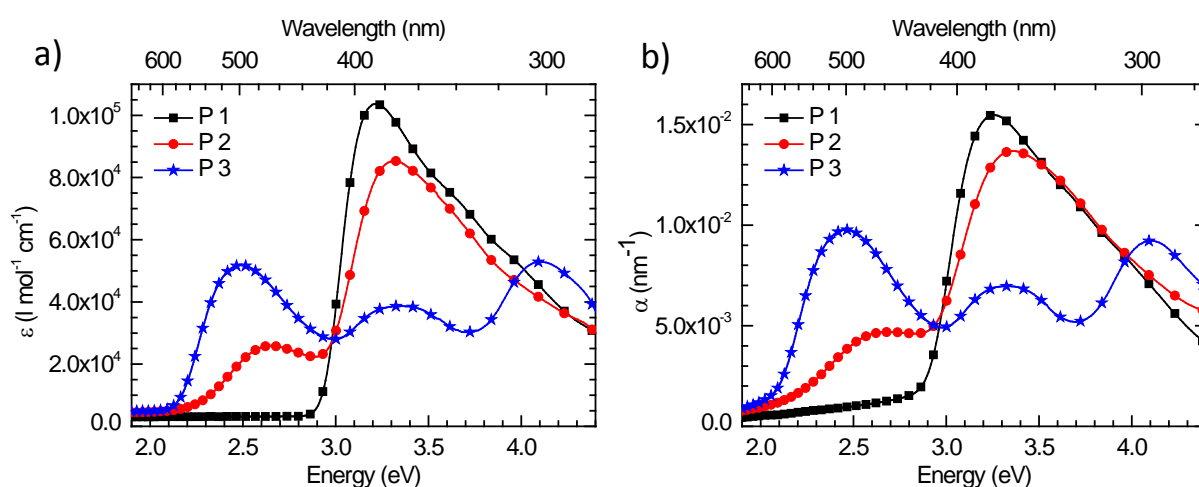


Figure 3. UV-vis absorption spectra of **P1**, **P2** and **P3**. a) in chlorobenzene, concentration of the repetition units 10⁻⁴ mol l⁻¹. b) in film from 10 mg ml⁻¹ solutions in chlorobenzene.

In **P3**, the thieno[3,4-*b*]thiophene carboxylate, acting as an electron pulling unit, is placed directly in the main chain of the copolymer, allowing for a good electronic interaction with the TPA unit. As for **P2**, we observe a low-energy absorption band centered at 2.49 eV in addition to the original TPA absorption at 3.26 eV. Compared to **P2**, this low-energy band is shifted further to the red by 0.17 eV and carries a higher oscillator strength. Concomitantly, the oscillator strength of the high energy 3.26 eV band is strongly reduced. We consider the high oscillator strength of the additional, red-shifted absorption peak of **P3** and the reduction of the 3.26 eV intensity to indicate a significant contribution of π - π^* -transitions to the intramolecular CT-band that arises from the DA -type interaction of the electron withdrawing thieno[3,4-*b*]thiophene carboxylate with the TPA unit. Similarly, we interpret the red shift of the low-energy band compared to that of **P2** to indicate a higher degree of conjugation, consistent with a stronger contribution of the delocalized π -orbitals. We obtain the same results for the absorption spectra

taken in thin films, except for a small solvent shift. The positions of the absorption peaks are summarized in Table 3.

Table 3. Absorption Peaks (Position of the Center) in a Chlorobenzene Solution at a Concentration of the Repetition Units of $10^{-4} \text{ mol l}^{-1}$ and in the Film, Made from Solutions of 10 mg ml^{-1} in Chlorobenzene.

Polymer	E_{solution} (eV)	E_{film} (eV)
P1	3.22	3.26
P2	2.66, 3.32	2.68, 3.36
P3	2.49, 3.36, 4.11	2.46, 3.34, 4.11

Further information on the nature of excited states in the polymers can be obtained from photoluminescence measurements. First, we find that the three polymers differ strongly in their thin film photoluminescence efficiencies. While integrating sphere measurements taken on thin films give a moderate photoluminescence quantum yield (PL QY) of 3.4 % for homopolymer **P1**, the emission is below the detection threshold of this setup for **P2**, and it is as low as 0.7 % for **P3**. The uncertainty on the PL QY is about 1 %. This trend is consistent with the observed absorption strengths of the lowest energy bands in all three polymers and confirms the indication of a stronger CT-character in **P2** compared to **P3**, and, naturally, of no CT-characteristics in **P1**. Due to the low emission efficiencies, we used the sensitive technique of TCSPC to measure the photoluminescence spectra and lifetimes. The spectra are shown in Figure 4. No reliable data can be obtained for the spectral window from 2.35 to 2.50 eV due to a technical limitation. Photoluminescence decay curves are included as Supporting Information.

We shall discuss the data for the compounds in increasing order of intramolecular CT-character. For homopolymer **P1**, the same emission band with a 0–0 peak at 2.89 eV and vibronic replica at 2.72 and 2.55 eV is seen in solution and, shifted by 40 meV to the red, in film. This emission dominates for a few nanoseconds after excitation with a lifetime of 0.9 ns in solution and 0.3 ns in the film. At longer times, this emission disappears and a weak, structured emission can be observed. It is shifted to the red by about 0.3 eV and has a lifetime of about 6 ns in solution and 5 ns in film. Since this signal is rather weak with poor spectral to noise ratio, we can spectrally resolve it only for the film, where the higher energy emission decays away fast, yet not for

solution. Due to the moderate Stokes's shift of about 0.33 eV between absorption and emission and the concomitant mirror symmetry, we attribute the higher energy emission with 0–0 peak at 2.89 eV to the π - π^* -transition in the TPA-homopolymer, possibly with some mixing of the nonbonding orbital of the nitrogen lone pair. The electronic origin of the lower energy emission at about 2.55 eV is not clear. This emission is present in both phases, solution and film, with the same lifetime, yet in solution it is masked by the stronger higher energy emission. The reduction of the fast component in photoluminescence lifetime in film compared to solution suggests that the weakly red emitting sites can only be populated effectively by energy transfer in the condensed phase of the film.

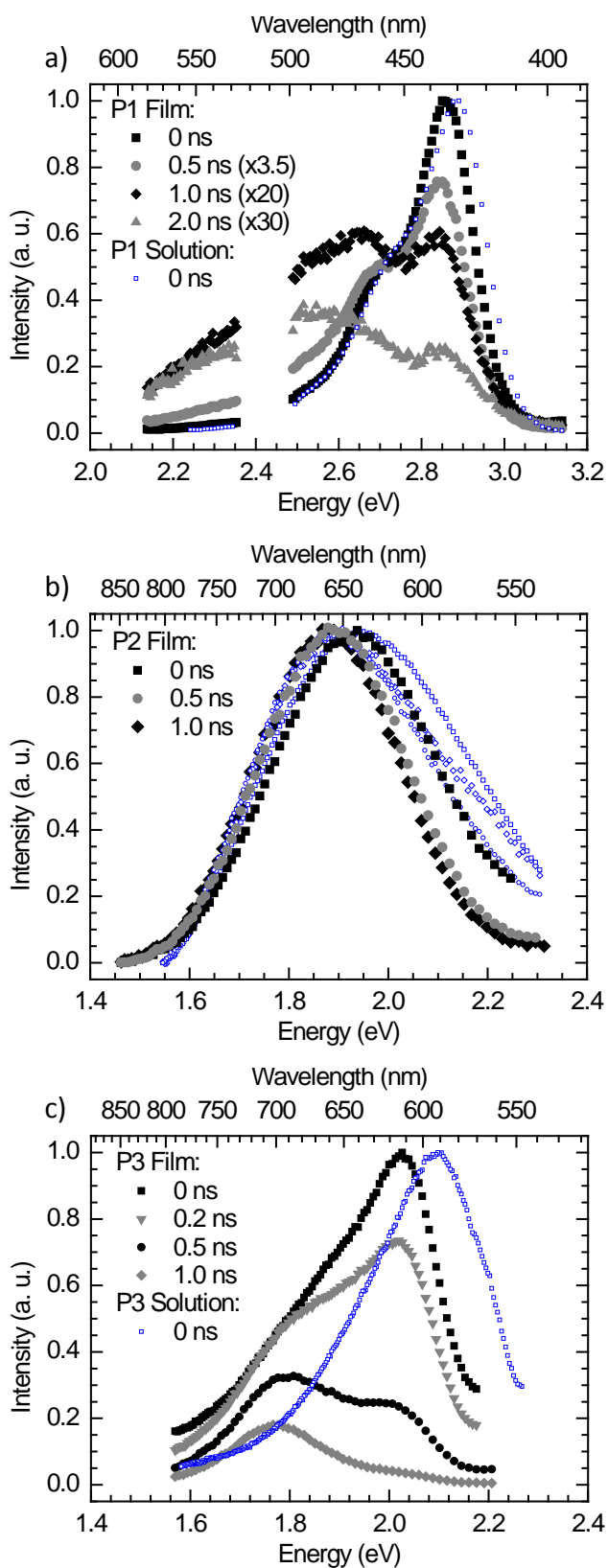


Figure 4. Fluorescence spectra of the polymers in chlorobenzene solutions at a concentration of the repetition units of (**P1**, **P3**: 10^{-5} mol l $^{-1}$, **P2**: 10^{-3} mol l $^{-1}$) and in the film under UV-irradiation (**P1**: 375 nm, **P2**, **P3**: 485 nm) measured in a TCSPC setup. In the spectral window from 2.35 eV to 2.50 eV, no reliable data could be obtained due to a technical limitation.

We next consider the copolymer **P3** where electron-rich and electron-deficient groups alternate in the chain backbone. The spectra in solution and in film immediately after excitation have a spectral shape similar to that in **P1** with similar full width at half-maximum (fwhm) of about 0.2 eV and a comparable Stokes's shift of 0.40 eV. The spectra show a $\theta\theta$ peak at 2.10 eV in solution and slightly below, at 2.03 eV, in film. Whereas no spectral change with time is noticeable in solution, in film the higher energy emission decays and exposes a weak emission centered at 1.79 eV that was initially hidden in the red tail of the higher energy peak. The energy difference between the comparatively intense higher energy emission and the weak lower energy emission bands is similar for **P1** and **P3**. In **P1**, it is about 0.30 eV, and in **P3**, it is 0.24 eV. Overall, the dominant decay lifetimes in copolymer **P3** are longer than those of homopolymer **P1**. For **P3** in solution, the decay is not entirely exponential and can best be approximated by a biexponential decay with lifetimes of 2.0 ns (amplitude 20.000) and 3.2 ns (amplitude 7.000); i.e., the dominant contribution is twice as long as that for **P1**. This is consistent with the reduced oscillator strength of **P3** compared to **P1** that is also manifested in the intensity of the low-energy absorption peak and the photoluminescence quantum yield. For **P3** in film, the luminescence decay proceeds faster and it is characterized by a distribution of lifetimes. In contrast to **P1** and **P3**, for **P2** with the dicyanovinyl in the side group we observe a very weak, broad, unstructured emission centered at about 1.9 eV. To enable detection of this inefficiently emitting compound in solution, we used a concentration of the repetition units of 10^{-3} mol L⁻¹ instead of the 100 times lower value used for **P1** and **P3**. For both, solution and film, the emission does not change with time except for an initial slight red shift that is common for condensed media where spectral diffusion in the density of states prevails.²⁷ We stress that, in particular, in contrast to **P1** and **P3**, there is no significant change of the spectral shape over time. The emission is characterized by a distribution of lifetimes in the nanosecond range, with more longer lived contributions for the film. Such a broad, unstructured weak emission with a distribution of lifetimes is a general signature for a CT-type transition. The overall picture that emerges from the absorption and photoluminescence spectroscopy is that, in **P2**, the excited state is dominated by CT-character, manifested in weak absorption and weak, unstructured emission. The homopolymer **P1** shows the moderately intense emission and good absorption associated with π - π^* -transitions as well as a weak, lower energy emission of unclear origin. The nature of the first excited state in the copolymer **P3** lies between the two limiting cases defined by **P1** and **P2**.

Photocurrent Measurements

We next consider how the different nature of the excited states impacts on their performance as solar cell materials. Therefore, we built bilayer solar cells where C_{60} is evaporated on top of a spin-coated polymer film. Indium–tin-oxide covered by a layer of PEDOT:PSS was used as anode and aluminum as a cathode. The simple device geometry of a bilayer allows for spatially distinct electron and hole pathways to the electrodes, thus preventing the nongeminate recombination of accidentally meeting charge carriers that is inherently problematic in the intermingled morphology of blends. The observed photocurrent characteristics in a bilayer structure can therefore be interpreted as arising mainly from the charge generation at the D–A-interface itself. The current–voltage curves of the bilayer solar cells for the different materials under AM 1.5 illumination are shown in Figure 5, along with the external quantum efficiency (EQE) spectra. The resulting solar cell parameters are given in the Supporting Information.

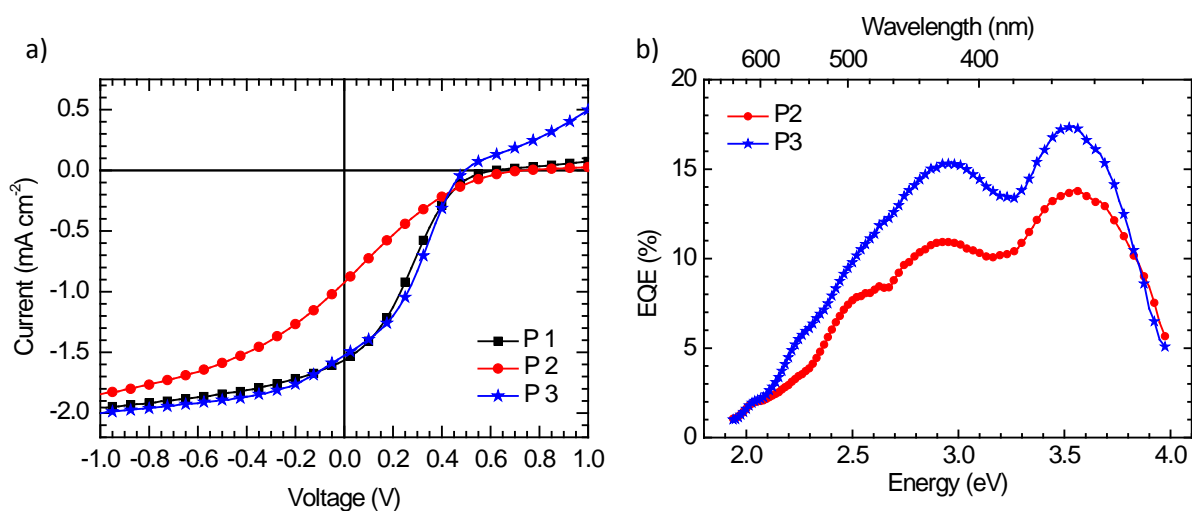


Figure 5. a) Current-Voltage characteristics of bilayer solar cells build with the presented polymers **P1**, **P2**, **P3** and C_{60} under AM 1.5 illumination. b) Corresponding External Quantum Efficiency (EQE) spectra of the copolymers **P2** and **P3**.

Homopolymer **P1** and copolymer **P3** show nearly identical current–voltage (I – V) curves up to the open-circuit voltage V_{oc} , with similarly moderate performance. The moderate performance is expected for bilayer cells with such material combination.¹⁰ Copolymer **P2** that has the stronger CT-character, however, is distinct and displays a reduced short-circuit current I_{sc} and a concomitantly reduced fill factor FF. The lower efficiency of **P2** compared to **P3** over the whole spectral range is also evident in the EQE spectra that largely follow the absorption data of the blend. All three cells have a pronounced “S-shape”, i.e., a zero or low photocurrent for forward

bias, at voltages exceeding the open-circuit voltage. The appearance of low current upon further voltage increase is occasionally reported, and it is tentatively attributed to imbalanced mobilities of the donor and the acceptor in planar heterojunction cells.²⁸

DISCUSSION

The aim of our study is to understand what controls charge separation in D-A-copolymers **P2** and **P3**. The impacts both of dipolar or electrostatic effects and of excited-state delocalization have been demonstrated to be of importance.²⁹⁻³² Here, we try to differentiate between both influences by comparing a homopolymer to two D-A-copolymers that represent two different chemical architectures. D-A-copolymer **P2** with a dicyanovinyl group in the side chain (with reduced delocalization with the main chain) shows a stronger CT-character than **P3** where the acceptor moiety is incorporated in the main chain. This is evident from the reduced oscillator strengths of the first absorption band in **P2** compared to **P1** and a barely detectable, broad, unstructured fluorescence that decays nonexponentially. D-A-copolymer **P3** possesses a weaker CT-character as demonstrated by the absorption and photoluminescence properties (vide supra); this results in a lower prominence of the intrachain CT-character due to significant contributions of delocalized π - and π^* -orbitals. The question is now whether the more dipolar character of **P2** favors charge separation, e.g., by pre-separation of the hole and electron on the copolymer and concomitant dielectric screening,²⁹ or whether the higher degree of excited-state delocalization in **P3** is a more beneficial approach. From the I - V curve in Figure 5, a reduced performance of **P2** compared to **P3** is already evident. The data of Figure 5 can be analyzed by comparison with exciton dissociation models. For this, the photocurrent quantum yield for **P2** and **P3** is plotted as a function of internal electric field in Figure 6. The photocurrent quantum yield has been normalized to unity at the saturation value obtained for high field strengths since, for sufficiently high field, complete exciton dissociation and extraction are obtained.³⁰ The internal field F is calculated by subtracting the applied voltage from the open-circuit voltage and dividing the result by the active layer thickness of the device. The effect of possible deviations in the internal field from the value obtained by this method is discussed in detail in ref 31. Figure 6 shows that a higher electrical field is needed to dissociate all excitons in **P2** ($F_{\text{saturation}} = 1.5 \times 10^5 \text{ V cm}^{-1}$) than in **P3** ($F_{\text{saturation}} = 6 \times 10^4 \text{ V cm}^{-1}$), implying that excitons in **P2** are more tightly bound than those in **P3**. Exciton dissociation at the interface between a polymer donor material and a fullerene acceptor is understood to be assisted by both electrostatic interface effects (“interfacial dipole”, parametrized through a fractional dipole strength α) and charge delocalization. The latter can be parametrized in terms of a heuristic “effective mass” of the hole on the polymer.³¹ Whereas electrostatic effects screen the mutual coulomb attraction of electron and hole, the kinetic energy associated with a delocalized hole helps its escape from the

coulomb potential of its geminate electron.³³⁻³⁵ In order to obtain insight into the observed photodissociation behavior, we have fitted the field-dependent photocurrent quantum yields with a model containing the effects of both interfacial dipoles and hole delocalization (eqs 3, 6, and 7 in ref 31). Good agreement with the experimental data can be obtained when the fractional dipole strength α at the interface to C_{60} is set at 0.050 in **P2** and at 0.045 in **P3**, leading to effective relative hole masses m_{eff}/m_e of 0.44 for **P2** and 0.25 for **P3**, where m_e is the mass of a free electron. These parameter values obtained are consistent with earlier work on homopolymers in bilayers with C_{60} .³¹ The fractional dipole strengths are about twice as high as those measured for homopolymer/ C_{60} interfaces, and the effective masses are in a similar range, depending on the degree of conjugation of the polymers. As detailed in the Supporting Information, it is possible to increase the fractional dipole strength for **P2** while maintaining a good agreement with the data when simultaneously increasing the hole effective mass further.

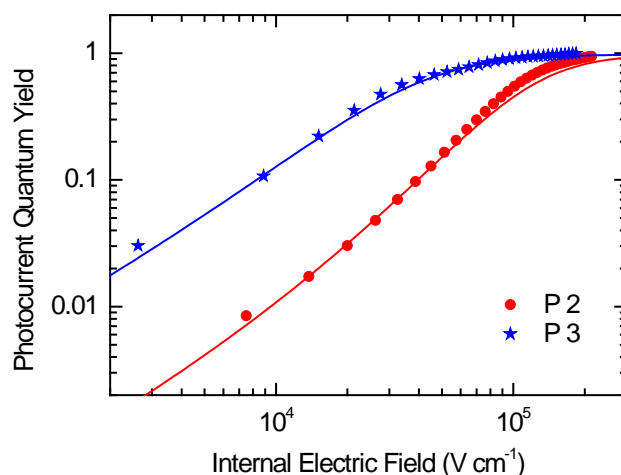


Figure 6. Normalized field dependent photocurrent quantum yields of copolymer/ C_{60} bilayer devices calculated from the photocurrent under AM 1.5 conditions. The lines indicate fits based on an effective mass model that includes interfacial dipole effects.

What is the insight obtained from these values? This analysis tells us that the improved performance of **P3** compared to **P2**, i.e. the higher photodissociation at low internal field strength, and concomitantly the higher short-circuit current and fill factor, are a result of the lower effective mass in **P3**. A more delocalized character of the hole on **P3** is fully consistent with the overall more delocalized character of the excited state in **P3** that is manifested in the optical measurements, and the higher hole mobility in **P3**. Furthermore, the photocurrent analysis shows a more localized hole on **P2** to be associated with a poor photodissociation, while the CT-character of **P2** does not turn out to be of benefit to the charge separation process. A

more localized hole with a higher effective mass derived in the photocurrent fit corresponds well with the reduced hole mobility measured for **P2** in SCLC measurements. The fact that this correlates with a low HOMO level points at trapping effects or localization effects.^{36,37} Comparing these results of field-dependent photocurrent quantum yields with previous work on charge separation emphasizes the importance of a good conjugation to facilitate charge separation.

CONCLUSION

On comparison of the homopolymer **P1** with the two D-Acopolymers **P2** and **P3**, we could get conclusive information regarding the effective design of AD -copolymers for an efficient delocalization/conjugation and good charge generation. The introduction of the strong electron withdrawing dicyanovinyl acceptor unit as side chain in **P2** reduces the electron richness and delocalization of the TPA main chain. As a consequence the HOMO level is lowered in **P2** and the hole mobility is decreased. **P2** has a pronounced excited-state CT character compared to **P3** in which the acceptor enters into delocalization with the backbone. Field-dependent photocurrent measurements in bilayer devices clearly indicate the advantage of the alternating AD -copolymer strategy in which the donor and acceptor moieties exhibit a better conjugation. Thus, for this material system, charge separation is obtained more readily when the acceptor group is located within the copolymer backbone guaranteeing delocalization along the main chain. The concept of adding a strong acceptor to the side group which lowers the delocalization in the main chain, in contrast, results in a lower hole mobility and stronger bound electron hole pairs and thus lower solar cell power conversion efficiency.

ACKNOWLEDGMENTS

We acknowledge the Graduate School GRK 1640 of the Deutsche Forschungsgemeinschaft (DFG) and the Bavarian State Ministry of Science, Research, and the Arts for the Collaborative Research Network "Solar Technologies go Hybrid" for financial support and K.N. thanks the Universität Bayern e.V. for financial support in the form of a scholarship of the Bayerische Graduiertenförderung and the Elitenetzwerk Bayern (ENB). We also thank Sabrina Willer for support in the synthesis work and Sebastian Hoffmann and Stephan Kümmel for fruitful discussions.

REFERENCES

- (1) Deibel, C.; Dyakonov, V., Polymer-Fullerene Bulk Heterojunction Solar Cells. *Rep. Prog. Phys.* **2010**, *73*.
- (2) Green, M. A.; Emery, K.; Hishikawa, Y.; Warta, W.; Dunlop, E. D. Solar Cell Efficiency Tables (Version 40). *Prog. Photovoltaics* **2012**, *20*, 606–614.
- (3) Li, Y. Molecular Design of Photovoltaic Materials for Polymer Solar Cells: Toward Suitable Electronic Energy Levels and Broad Absorption. *Acc. Chem. Res.* **2012**, *45*, 723–733.
- (4) Boudreault, P. L. T.; Najari, A.; Leclerc, M. Processable Low-Bandgap Polymers for Photovoltaic Applications. *Chem. Mater.* **2011**, *23*, 456–469.
- (5) Duan, C. H.; Cai, W. Z.; Huang, F.; Zhang, J.; Wang, M.; Yang, T. B.; Zhong, C. M.; Gong, X.; Cao, Y. Novel Silafluorene-Based Conjugated Polymers with Pendant Acceptor Groups for High Performance Solar Cells. *Macromolecules* **2010**, *43*, 5262–5268.
- (6) Hellström, S.; Lindgren, L. J.; Zhou, Y.; Zhang, F. L.; Inganäs, O.; Andersson, M. R. Synthesis and Characterization of Three Small Band Gap Conjugated Polymers for Solar Cell Applications. *Polym. Chem.* **2010**, *1*, 1272–1280.
- (7) Hou, J. H.; Tan, Z. A.; Yan, Y.; He, Y. J.; Yang, C. H.; Li, Y. F. Synthesis and Photovoltaic Properties of Two-Dimensional Conjugated Polythiophenes with Bi(thienylenevinylene) Side Chains. *J. Am. Chem. Soc.* **2006**, *128*, 4911–4916.
- (8) Zhang, Z. G.; Liu, Y. L.; Yang, Y.; Hou, K. Y.; Peng, B.; Zhao, G. J.; Zhang, M. J.; Guo, X.; Kang, E. T.; Li, Y. F. Alternating Copolymers of Carbazole and Triphenylamine with Conjugated Side Chain Attaching Acceptor Groups Synthesis and Photovoltaic Application. *Macromolecules* **2010**, *43*, 9376–9383.
- (9) Zhang, Z.-G.; Wang, J. Structures and Properties of Conjugated Donor-Acceptor Copolymers for Solar Cell Applications. *J. Mater. Chem.* **2012**, *22*, 4178–4187.
- (10) Zhang, Z. G.; Zhang, K. L.; Liu, G.; Zhu, C. X.; Neoh, K. G.; Kang, E. T. Triphenylamine-Fluorene Alternating Conjugated Copolymers with Pendant Acceptor Groups: Synthesis, Structure-Property Relationship, and Photovoltaic Application. *Macromolecules* **2009**, *42*, 3104–3111.
- (11) Clarke, T. M.; Ballantyne, A.; Shoaee, S.; Soon, Y. W.; Duffy, W.; Heeney, M.; McCulloch, I.; Nelson, J.; Durrant, J. R. Analysis of Charge Photogeneration as a Key Determinant of Photocurrent Density in Polymer: Fullerene Solar Cells. *Adv. Mater.* **2010**, *22*, 5287–5291.

- (12) Clarke, T. M.; Durrant, J. R. Charge Photogeneration in Organic Solar Cells. *Chem. Rev.* **2010**, *110*, 6736–6767.
- (13) Veldman, D.; Ipek, O.; Meskers, S. C. J.; Sweelssen, J.; Koetse, M. M.; Veenstra, S. C.; Kroon, J. M.; van Bavel, S. S.; Loos, J.; Janssen, R. A. J. Compositional and Electric Field Dependence of the Dissociation of Charge Transfer Excitons in Alternating Polyfluorene Copolymer/Fullerene Blends. *J. Am. Chem. Soc.* **2008**, *130*, 7721–7735.
- (14) Tautz, R.; Da Como, E.; Limmer, T.; Feldmann, J.; Egelhaaf, H. J.; von Hauff, E.; Lemaire, V.; Beljonne, D.; Yilmaz, S.; Dumsch, I.; Allard, S.; Scherf, U. Structural Correlations in the Generation of Polaron Pairs in Low-Bandgap Polymers for Photovoltaics. *Nat. Commun.* **2012**, *3*, No. 970.
- (15) Carsten, B.; Szarko, J. M.; Son, H. J.; Wang, W.; Lu, L. Y.; He, F.; Rolczynski, B. S.; Lou, S. J.; Chen, L. X.; Yu, L. P. Examining the Effect of the Dipole Moment on Charge Separation in Donor-Acceptor Polymers for Organic Photovoltaic Applications. *J. Am. Chem. Soc.* **2011**, *133*, 20468–20475.
- (16) Thelakkat, M. Star-Shaped, Dendrimeric and Polymeric Triarylamines as Photoconductors and Hole Transport Materials for Electro-Optical Applications. *Macromol. Mater. Eng.* **2002**, *287*, 442–461.
- (17) Roncali, J. Synthetic Principles for Bandgap Control in Linear Pi-Conjugated Systems. *Chem. Rev.* **1997**, *97*, 173–205.
- (18) deMello, J. C.; Wittmann, H. F.; Friend, R. H. An Improved Experimental Determination of External Photoluminescence Quantum Efficiency. *Adv. Mater.* **1997**, *9*, 230–232.
- (19) Hong, S. Y.; Marynick, D. S. Understanding the Conformational Stability and Electronic Structures of Modified Polymers Based on Polythiophene. *Macromolecules* **1992**, *25*, 4652–4657.
- (20) Liang, Y. Y.; Feng, D. Q.; Guo, J. C.; Szarko, J. M.; Ray, C.; Chen, L. X.; Yu, L. P. Regioregular Oligomer and Polymer Containing Thieno[3,4-*b*]thiophene Moiety for Efficient Organic Solar Cells. *Macromolecules* **2009**, *42*, 1091–1098.
- (21) Schlüter, A. D. The Tenth Anniversary of Suzuki Polycondensation (SpC). *J. Polym. Sci., Part A: Polym. Chem.* **2001**, *39*, 1533–1556.
- (22) Park, J. H.; Seo, Y. G.; Yoon, D. H.; Lee, Y. S.; Lee, S. H.; Pyo, M.; Zong, K. A Concise Synthesis and Electrochemical Behavior of Functionalized Poly(Thieno[3,4-*b*]Thiophenes): New Conjugated Polymers with Low Bandgap. *Eur. Polym. J.* **2010**, *46*, 1790–1795.

- (23) Kun, H.; Yi, H.; Johnson, R. G.; Iraqi, A. Fluoro-Protected Carbazole Main-Chain Polymers as a New Class of Stable Blue Emitting Polymers. *Polym. Adv. Technol.* **2008**, *19*, 299–307.
- (24) Noviandri, I.; Brown, K. N.; Fleming, D. S.; Gulyas, P. T.; Lay, P. A.; Masters, A. F.; Phillips, L. The Decamethylferrocenium/Decamethylferrocene Redox Couple: A Superior Redox Standard to the Ferrocenium/Ferrocene Redox Couple for Studying Solvent Effects on the Thermodynamics of Electron Transfer. *J. Phys. Chem. B* **1999**, *103*, 6713–6722.
- (25) Gräf, K.; Rahim, M. A.; Das, S.; Thelakkat, M. Complementary Co-Sensitization of an Aggregating Squaraine Dye in Solid-State Dye-Sensitized Solar Cells. *Dyes Pigm.* **2013**, *99*, 1101–1106.
- (26) Goh, C.; Kline, R. J.; McGehee, M. D.; Kadnikova, E. N.; Fréchet, J. M. J. Molecular-Weight-Dependent Mobilities in Regioregular Poly(3-Hexyl-thiophene) Diodes. *Appl. Phys. Lett.* **2005**, *86*, No. 122110.
- (27) Meskers, S. C. J.; Hübner, J.; Oestreich, M.; Bäessler, H. Dispersive Relaxation Dynamics of Photoexcitations in a Polyfluorene Film Involving Energy Transfer: Experiment and Monte Carlo Simulations. *J. Phys. Chem. B* **2001**, *105*, 9139–9149.
- (28) Tress, W.; Petrich, A.; Hummert, M.; Hein, M.; Leo, K.; Riede, M. Imbalanced Mobilities Causing S-Shaped IV Curves in Planar Heterojunction Organic Solar Cells. *Appl. Phys. Lett.* **2011**, *98*, No. 063301.
- (29) Carsten, B.; Szarko, J. M.; Lu, L. Y.; Son, H. J.; He, F.; Botros, Y. Y.; Chen, L. X.; Yu, L. P. Mediating Solar Cell Performance by Controlling the Internal Dipole Change in Organic Photovoltaic Polymers. *Macromolecules* **2012**, *45*, 6390–6395.
- (30) Schwarz, C.; Bäessler, H.; Bauer, I.; Koenen, J. M.; Preis, E.; Scherf, U.; Köhler, A. Does Conjugation Help Exciton Dissociation? A Study on Poly(p-Phenylene)s in Planar Heterojunctions with C60 or TNF. *Adv. Mater.* **2012**, *24*, 922–925.
- (31) Schwarz, C.; Tscheuschner, S.; Frisch, J.; Winkler, S.; Koch, N.; Bäessler, H.; Köhler, A. Role of the Effective Mass and Interfacial Dipoles on Exciton Dissociation in Organic Donor-Acceptor Solar Cells. *Phys. Rev. B* **2013**, *87*, No. 155205.
- (32) Verlaak, S.; Beljonne, D.; Cheyns, D.; Rolin, C.; Linares, M.; Castet, F.; Cornil, J.; Heremans, P. Electronic Structure and Geminate Pair Energetics at Organic-Organic Interfaces: The Case of Pentacene/C-60 Heterojunctions. *Adv. Funct. Mater.* **2009**, *19*, 3809–3814.

- (33) Arkhipov, V. I.; Heremans, P.; Bäessler, H. Why Is Exciton Dissociation So Efficient at the Interface between a Conjugated Polymer and an Electron Acceptor? *Appl. Phys. Lett.* **2003**, *82*, 4605–4607.
- (34) Nenashev, A. V.; Baranovskii, S. D.; Wiemer, M.; Jansson, F.; Österbacka, R.; Dvurechenskii, A. V.; Gebhard, F. Theory of Exciton Dissociation at the Interface between a Conjugated Polymer and an Electron Acceptor. *Phys. Rev. B* **2011**, *84*, No. 035210.
- (35) Wiemer, M.; Nenashev, A. V.; Jansson, F.; Baranovskii, S. D. On the Efficiency of Exciton Dissociation at the Interface between a Conjugated Polymer and an Electron Acceptor. *Appl. Phys. Lett.* **2011**, *99*, No. 013302.
- (36) Nicolai, H. T.; Kuik, M.; Wetzelaer, G. A. H.; de Boer, B.; Campbell, C.; Risko, C.; Brédas, J. L.; Blom, P. W. M. Unification of Trap-Limited Electron Transport in Semiconducting Polymers. *Nat. Mater.* **2012**, *11*, 882–887.
- (37) Hoffmann, S. T.; Jaiser, F.; Hayer, A.; Bäessler, H.; Unger, T.; Athanasopoulos, S.; Neher, D.; Köhler, A. How Do Disorder, Reorganization, and Localization Influence the Hole Mobility in Conjugated Copolymers. *J. Am. Chem. Soc.* **2013**, *135*, 1772–1782.

Supporting Information to

Influence of the Excited State Charge-Transfer Character on the Exciton Dissociation in Donor-Acceptor Copolymers

Katharina Neumann, Christian Schwarz, Anna Köhler[#] and Mukundan Thelakkat^{}*

K. Neumann, M. Thelakkat
Applied Functional Polymers, Macromolecular Chemistry I
University of Bayreuth
95440 Bayreuth, Germany

*E-mail: mukundan.thelakkat@uni-bayreuth.de

C. Schwarz, A. Köhler
Experimental Physics II and Bayreuth Institute of Macromolecular Research (BIMF)
University of Bayreuth
95440 Bayreuth, Germany

[#]E-mail: anna.koehler@uni-bayreuth.de

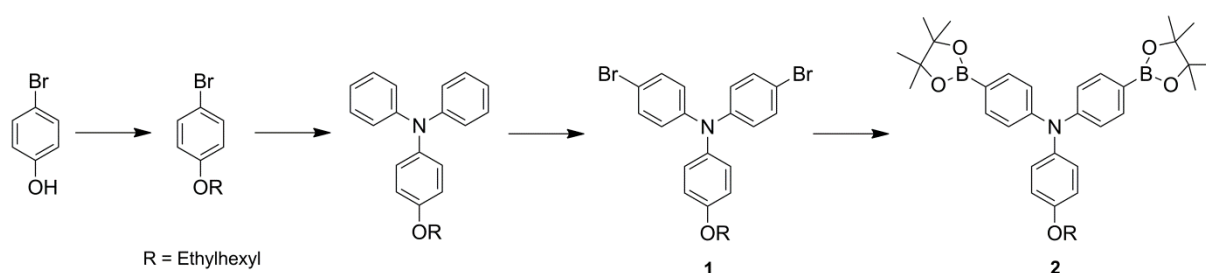
Table of contents

1	Materials
1.1	Monomer 1 and 2
	1-Bromo-4-[(2-ethylhexyl)oxy]-benzene
	4-(2-Ethylhexyloxy)-N,N-diphenylaniline
	4-Bromo-N-(4-bromophenyl)-N-(4-(2-ethylhexyloxy)phenyl)aniline (1)
	4-(2-Ethylhexyloxy)-N,N-bis(4-(4,4,5,5-tetramethyl-1,3,2-dioxaborolan-2-yl)phenyl)aniline (2)
1.2	Monomer 3
	4-(Bis(4-bromophenyl)amino)benzaldehyde (3)
1.3	Monomer 4
	4-Bromothiophene-3-carbaldehyde
	Octyl-thieno[3,4-b]thiophene-2-carboxylate
	Octyl-4,6-dibromo-thieno[3,4-b]thiophene-2-carboxylate (4)
2	¹ H-NMR
3	FT-IR spectra
4	Cyclic voltammetry
5	Space charge limited current measurements
6	Lifetime measurements
7	Photocurrent voltage curve for monochromatic illumination 18
8	P2: fits with the dipole model
9	Solar cell parameters
10	References

Materials

Commercially available starting materials were purchased from Aldrich or abcr and used without further purification. Solvents for chromatography, extraction and reactions were distilled prior to use.

Monomer 1 and 2



1-Bromo-4-[(2-ethylhexyl)oxy]-benzene

4-Bromophenol (18.08 g, 0.1 mol) and K_2CO_3 (33.83 g, 0.24 mol) were dissolved in dry DMF. 2-Ethylhexylbromide (15.45 g, 0.08 mol) was added slowly and the reaction mixture was stirred for 24 h at 60 °C. After cooling, the reaction mixture was extracted with hexane and 1 M HCl. The crude product was used without further purification. Yield: 75 %.

1H NMR (300 MHz, $CDCl_3$, 298 K): δ (ppm) = 7.42 - 7.34 (d, 2H, H_{ar}), 6.84 - 6.75 (d, 2H, H_{ar}), 3.84 - 3.79 (d, 2H, OCH_2), 1.80 - 1.66 (m, 1H, CH), 1.60 - 1.25 (m, 8H, CH_2), 1.00 - 0.83 (m, 6H, CH_3).

MS-EI m/z calcd for $C_{14}H_{21}BrO$ 285.22, found $[M^+]$ 284.

4-(2-Ethylhexyloxy)-N,N-diphenylaniline

Diphenylamine (4.91 g, 0.029 mol), 1-bromo-4-[(2-ethylhexyl)oxy]-benzene (10 g, 0.035 mol), sodium-*tert*-butoxide (3.62 g, 0.038 mol) and 0.07 g (0.30 mmol) $Pd(OAc)_2$ were dissolved in dry toluene. Tri-*tert*-butylphosphine (1 M in toluene, 1ml) was added and the reaction mixture was heated to 60 °C for 24 h. After cooling to room temperature the solution was filtered over Alox N. The solvent was removed by reduced pressure and the crude product was precipitated in MeOH from THF and filtered. The white powder was dried in vacuum. Yield: 87 %.

1H NMR (300 MHz, $CDCl_3$, 298 K): δ (ppm) = 7.26 - 7.16 (m, 4H, H_a), 7.90 - 7.00 (m, 6H, H_{ar}), 6.97 - 6.90 (m, 2H, H_{ar}), 6.87 - 6.80 (m, 2H, H_{ar}), 3.85 - 3.79 (d, 2H, OCH_2), 1.76 - 1.65 (m, 1H, CH), 1.57 - 1.26 (m, 8H, CH_2), 0.97 - 0.86 (m, 6H, CH_3).

MS-EI m/z calcd for $C_{26}H_{31}NO$ 373.53, found $[M^+]$ 373.

4-Bromo-N-(4-bromophenyl)-N-(4-(2-ethylhexyloxy)phenyl)aniline (1)

4-[(2-Ethylhexyl)oxy]-N,N-diphenylaniline (8.36 g, 22.4 mmol) was dissolved in 190 ml of a 5:1 CHCl₃/AcOH mixture and degassed for 30 min with an argon stream. After cooling the solution to -10 °C NBS (7.97 g, 44.8 mmol) was added in small portions under exclusion of light. After stirring for 3.5 h at -10 °C the reaction was quenched with 1 M NaOH. The reaction mixture was extracted with DCM and water. The organic phase was washed with 1 M NaOH and two times with water. After drying over Na₂SO₄ the solvent was evaporated under reduced pressure. 4-Bromo-N-(4-bromophenyl)-N-(4-(2-ethylhexyloxy)phenyl)aniline was achieved as a viscous oil. Yield: 99 %.

¹H NMR (300 MHz, DMSO, 298 K): δ (ppm) = 7.33 - 7.25 (m, 4H, H_a), 7.06 - 6.98 (m, 2H, H_b), 6.92 - 6.81 (m, 6H, H_c), 3.85 - 3.80 (d, 2H, O-CH₂), 1.77 - 1.66 (m, 1H, CH), 1.58 - 1.26 (m, 8H, CH₂), 0.97 - 0.88 (s, 6H, CH₃).

MS-EI *m/z* calcd for C₂₆H₂₉Br₂NO 531.32 , found [M⁺] 531.

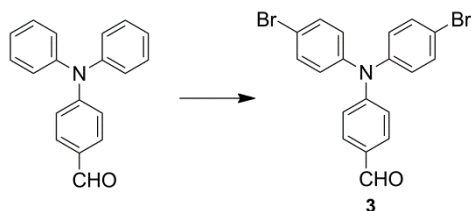
4-(2-Ethylhexyloxy)-N,N-bis(4-(4,4,5,5-tetramethyl-1,3,2-dioxaborolan-2-yl)phenyl)aniline (2)

4-Bromo-N-(4-bromophenyl)-N-(4-(2-ethylhexyloxy)phenyl)aniline **1** (3.30 g, 6.12 mmol) were dissolved in THF under an argon atmosphere. The solution was cooled to -78 °C and a solution of n-BuLi in hexane (8.15 mL, 1.6 M, 13.04 mmol) were added dropwise. After 2 h at -78 °C 2-isopropoxy-4,4,5,5-tetramethyl-1,2,3-dioxaborolane (8.6 ml, 7.80 g, 41.92 mmol) was added quickly. The reaction mixture was warmed to room temperature and stirred for 50 h. The reaction was quenched carefully with water. The following extraction was carried out with DCM and water. After drying over Na₂SO₄ the solvent was evaporated under reduced pressure. The residue was recrystallized in THF hexane (1:8). The non-crystallized part was purified chromatographically (CH:EE; 10:1). Yield: 27 %.

¹H NMR (300 MHz, CHCl₃, 298 K): δ (ppm) = 7.68 - 7.58 (d, 4H, H_a), 7.07 - 6.99 (m, 6H, H_b), 6.86 - 6.79 (m, 2H, H_c), 3.84 - 3.79 (d, 2H, O-CH₂), 1.76 - 1.66 (m, 1H, CH), 1.53 - 1.16 (m, 32H, CH₂, CH₃), 0.97 - 0.85 (m, 6H, CH₃).

MS-EI *m/z* calcd for C₃₈H₅₃B₂NO₅ 625.45, found [M⁺] 625.

Monomer 3



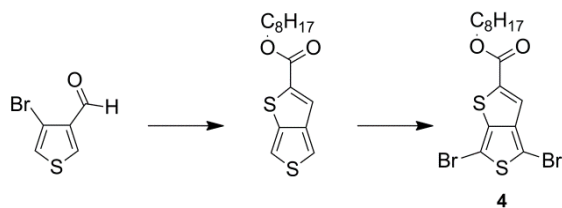
4-(Bis(4-bromophenyl)amino)benzaldehyde (3)

4-Diphenylaminobenzaldehyde (5.0 g, 19.9 mmol) was dissolved in 195 ml CHCl₃/AcOH (5:1) and degassed with an argon stream. The solution was cooled to -5 °C and N-bromosuccinimide (8 g, 45.77 mmol) were added in small portions. After stirring for 10 h the solution was warmed to room temperature and stirred for 30 h. The reaction was quenched with 1 M NaOH, extracted with DCM and washed with brine. The organic phase was dried over Na₂SO₄ and the solvent was evaporated under reduced pressure. The crude product was purified chromatographically (n-hexane:DCM, gradually from 5:1 to 1:1). 4-(Bis(4-bromophenyl)amino)benzaldehyde **3** was obtained as yellow powder. Yield: 81 %

¹H NMR (300 MHz, CDCl₃, 298 K): δ (ppm) = 9.85 - 9.83 (s, 1H, CHO), 7.74 - 7.66 (m, 2 H, H_a), 7.48 - 7.40 (m, 4H, H_b), 7.07 - 6.98 (m, 6H, H_c, H_d).

MS-EI *m/z* calcd 431.12, found [M⁺] 431.

Monomer 4



4-Bromothiophene-3-carbaldehyde

3,4-Dibromothiophene (14.44 g, 0.06 mol) were dissolved in dry diethylether and cooled to -78 °C. Afterwards 37 ml of *n*-BuLi (1.6 M in hexane) were added slowly. After 30 min DMF (5.97 ml, 0.08 mol) was added, the reaction mixture was warmed to room temperature and stirred over night. The reaction was quenched with saturated NH₄Cl solution in water and extracted with diethylether. The organic phase was dried over Na₂SO₄ and the solvent was evaporated under

reduced pressure. The crude product was purified by column chromatography (hexane : diethylether 5:1).

Yield: 56 %.

$^1\text{H NMR}$ (300 MHz, CHCl_3 , 298 K): δ (ppm) = 9.97 (s, 1H, H_{al}), 8.18 (d, 1H, H_{ar}), 7.39 (d, 1H, H_{ar}).

MS-EI m/z calcd for $\text{C}_5\text{H}_3\text{BrOS}$ 191.05, found $[\text{M}^+]$ 191.

Octyl-thieno[3,4-b]thiophene-2-carboxylate

4-Bromothiophene-3-carbaldehyde (5.82 g, 0.03 mol) and thioglycolic acid-octyl ester (6.85 g, 0.03 mol) were dissolved in 50 ml DMF. K_2CO_3 (6.22 g, 0.04 mol) and CuO nanopowder (0.07 g, 0.9 mmol) were added. The reaction mixture was heated to 80 °C for 16 h. The reaction mixture was extracted with DCM and water. The organic phase was dried over Na_2SO_4 and the solvent was evaporated under reduced pressure. The crude product was purified by column chromatography (Hexane : Ethylacetate, 90:1).

Yield: 31 %

$^1\text{H NMR}$ (300 MHz, CHCl_3 , 298 K): δ (ppm) = 7.71 (s, 1H, H_{ar}), 7.61 (d, 1H, H_{ar}), 7.30 (dd, 1H, H_{ar}), 4.33 (t, 2H, OCH_2), 1.78 (q, 2H, CH_2), 1.35 (m, 10H, CH_2), 0.91 (t, 3H, CH_3).

MS-EI m/z calcd for $\text{C}_{15}\text{H}_{20}\text{O}_2\text{S}_2$ 296.45, found $[\text{M}^+]$ 296.

Octyl-4,6-dibromo-thieno[3,4-b]thiophene-2-carboxylate (4)

Octyl-thieno[3,4-b]thiophene-2-carboxylate (2.77 g, 9.34 mmol) were dissolved in 30 ml dry DMF and degassed with an argon stream for 30 minutes. After cooling the solution in an ice bath 4.16 g (23.36 mmol) NBS were added in small portions. The reaction mixture was warmed up to room temperature. After stirring for 12 h the solution was poured into a 10% aqueous solution of $\text{Na}_2\text{S}_2\text{O}_3$ and extracted with diethylether twice. The organic phase was dried over Na_2SO_4 and the solvent was evaporated under reduced pressure. The crude product was purified by column chromatography (DCM).

Yield: 53 %

$^1\text{H NMR}$ (300 MHz, CHCl_3 , 298 K): δ (ppm) = 7.53 (s, 1H, H_{ar}), 4.32 (t, 2H, OCH_2), 1.76 (q, 2H, CH_2), 1.35 (m, 10H, CH_2), 0.89 (t, 3H, CH_3).

MS-EI m/z calcd for $\text{C}_{15}\text{H}_{20}\text{O}_2\text{S}_2$ 453.91, found $[\text{M}^+]$ 454.

$^1\text{H-NMR}$

^1H NMR spectra were recorded using a Bruker Avance 300 spectrometer at 300 MHz at 298 K in deuterated chloroform.

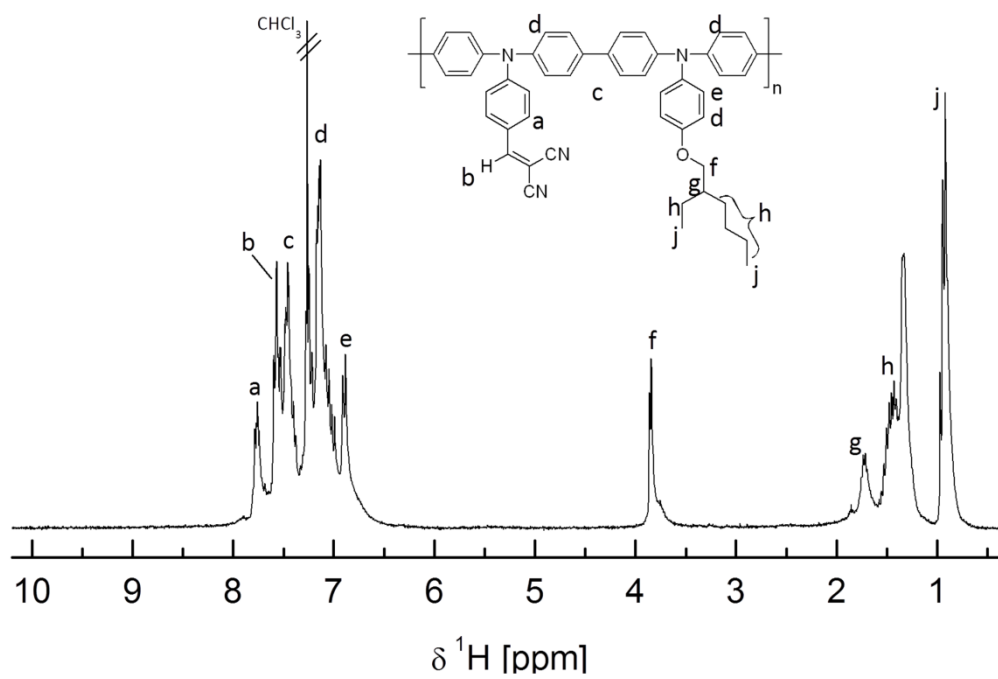


Figure 1. $^1\text{H-NMR}$ spectrum of P3. No signal for the aldehyde group was observed.

FT-IR spectra

FT-IR spectra were recorded on a *Perkin Elmer Spectrum 100* spectrometer in solid using a ATR unit.

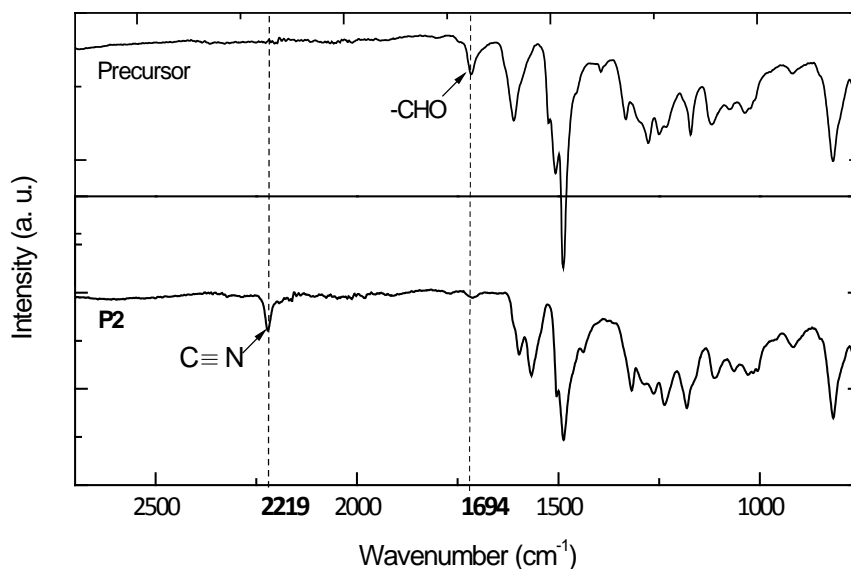


Figure 2. FT-IR-spectra of the precursor alternating copolymer with aldehyde-group showing a typical absorption band of the -CHO group at 1694 cm⁻¹ and the D-A-copolymer **P2** showing the CN-stretching vibration of the dicyanovinyl group at 2219 cm⁻¹.

Cyclic voltammetry

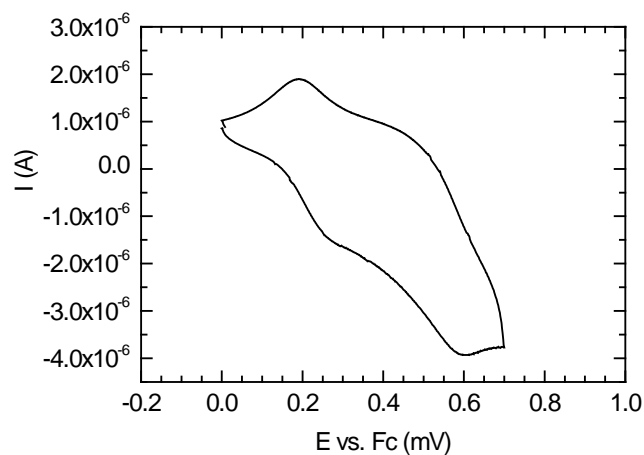


Figure 3. Cyclic voltammogram of **P1**.

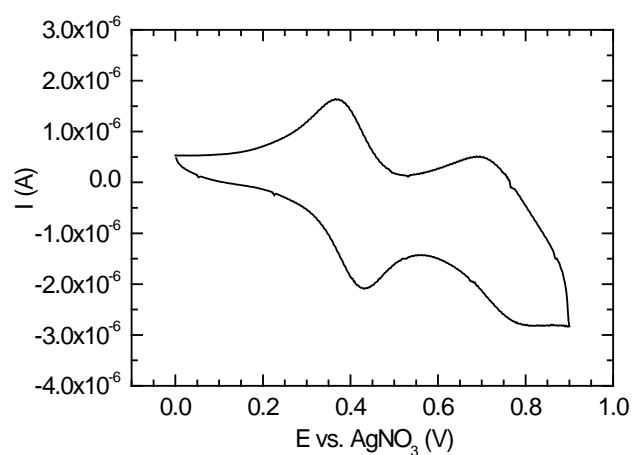


Figure 4. Cyclic voltammogram of **P2**.

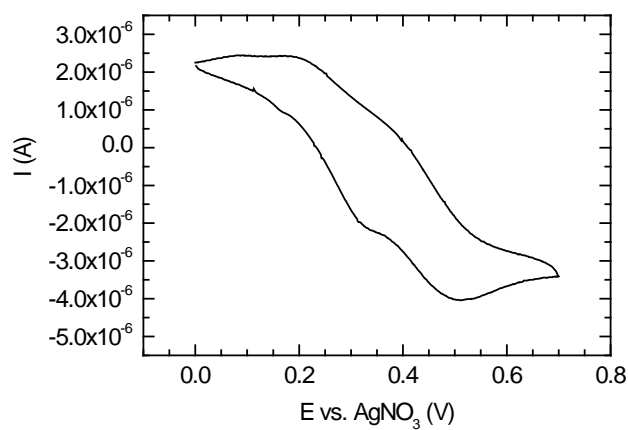


Figure 5. Cyclic voltammogram of **P3**.

Space charge limited current measurements

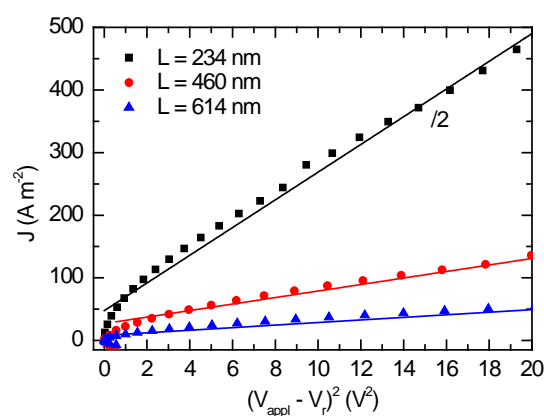


Figure 6. Hole-only devices of **P1** with varied layer thicknesses. The current density values for the layer thickness of 234 nm are divided by a factor of 2 to provide a better view on the other values.

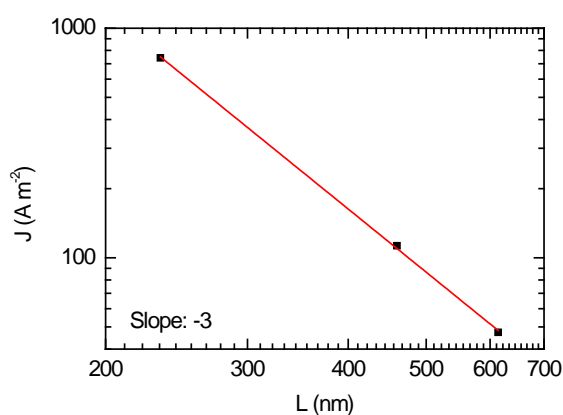


Figure 7. Log-log plot of the thickness dependence of the current density at a fixed bias of 4 V for **P1**. The squares are experimental data and the solid line is the fit according to relation $J \sim V^2/L^3$, where L is the thickness of the sample.

Device	L [nm]	μ_h [$\text{cm}^2\text{V}^{-1}\text{s}^{-1}$]
1	234	$1.8 \cdot 10^{-4}$
2	460	$1.4 \cdot 10^{-4}$
3	614	$1.0 \cdot 10^{-4}$
Average		$1.4 \cdot 10^{-4}$

Table 3. Calculated hole transport mobilities μ_h for three layer thicknesses as well as their average value.

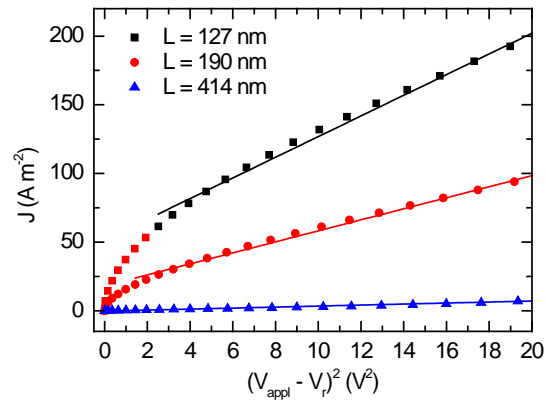


Figure 8. Hole-only devices of P2 with varied layer thicknesses.

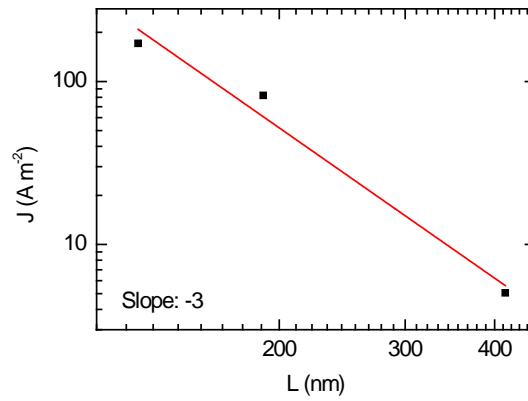


Figure 9. Log-log plot of the thickness dependence of the current density at a fixed bias of 4 V for **P2**. The squares are experimental data and the solid line is the fit according to relation $J \sim V^2/L^3$, where L is the thickness of the sample.

Device	L [nm]	μ_h [$\text{cm}^2\text{V}^{-1}\text{s}^{-1}$]
1	127	$5.0 \cdot 10^{-6}$
2	190	$8.5 \cdot 10^{-6}$
3	414	$9.2 \cdot 10^{-6}$
Average		$7.6 \cdot 10^{-6}$

Table 2. Calculated hole transport mobilities μ_h for three layer thicknesses as well as their average value.

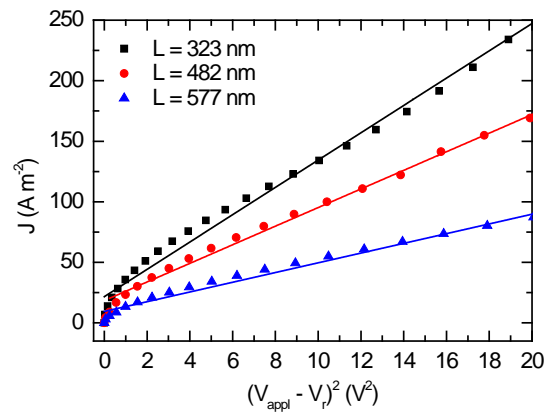


Figure 10. Hole-only devices of **P3** with varied layer thicknesses.

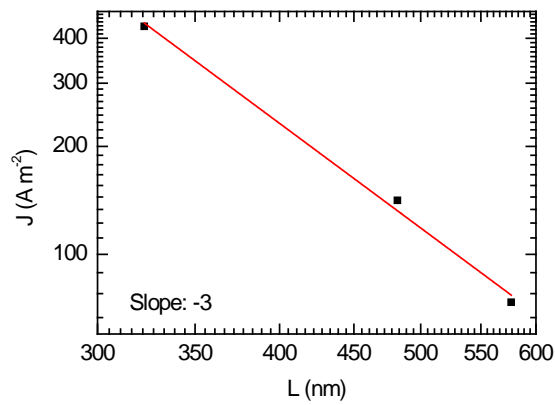


Figure 11. Log-log plot of the thickness dependence of the current density at a fixed bias of 4 V for **P3**. The squares are experimental data and the solid line is the fit according to relation $J \sim V^2/L^3$, where L is the thickness of the sample.

Device	L [nm]	μ_h [cm ² V ⁻¹ s ⁻¹]
1	323	$4.1 \cdot 10^{-4}$
2	482	$2.9 \cdot 10^{-4}$
3	577	$2.4 \cdot 10^{-4}$
Average		$3.1 \cdot 10^{-4}$

Table 3. Calculated hole transport mobilities μ_h for three layer thicknesses as well as their average value.

Lifetime measurements

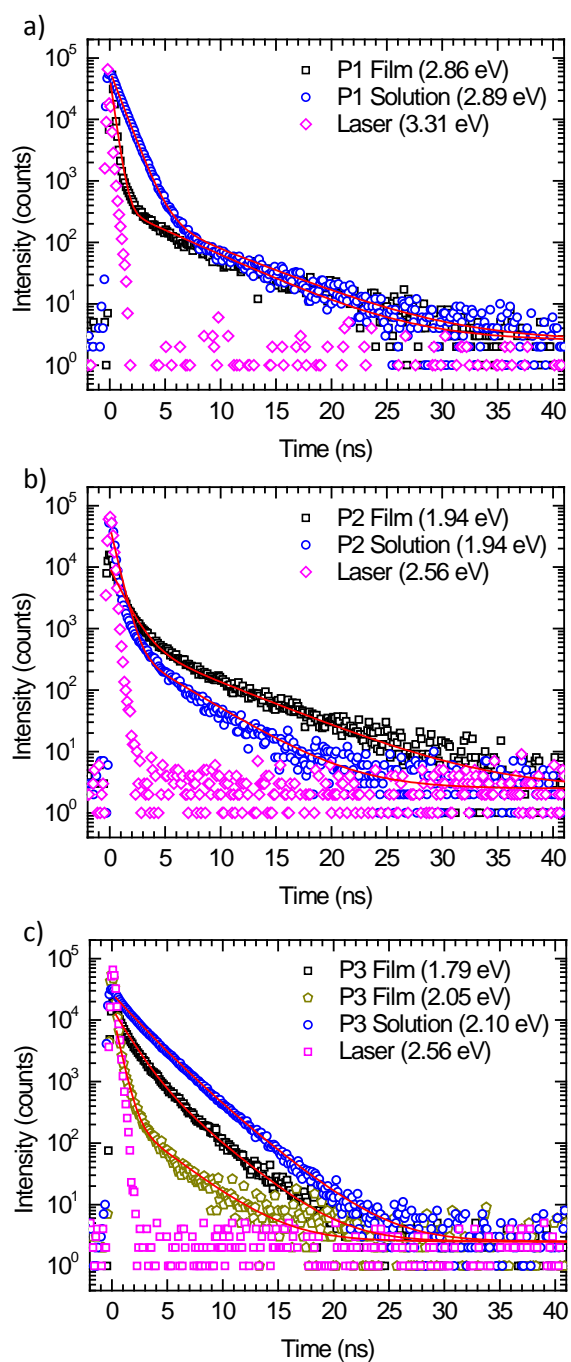


Figure 12. Lifetime measurements of the (co)polymers in a time correlated single photon counting (TCSPC) setup. The fit parameters are shown in table 4.

Polymer	A1	t1 (ns)	A2	t2 (ns)	y ₀
P1 Film	45600	0.3	400	5.3	2.5
P1 Solution	60800	0.9	400	6.0	2.5
P2 Film	9000	1.1	700	6.0	2.5
P2 Solution	45000	0.6	600	4.0	2.5
P3 Film (2.05 eV)	14000	0.5	320	3.2	2.5
P3 Film (1.79 eV)	13000	1.3	2600	3.0	2.5
P3 Solution	20000	2.0	7000	3.2	2.5

Table 4. Fit parameters of the lifetime fits in Figure 12, fitted with the biexponential equation $y = 1 \cdot \exp(-x/t1) + A2 \cdot \exp(-x/t2) + y0$

Photocurrent voltage curve for monochromatic illumination

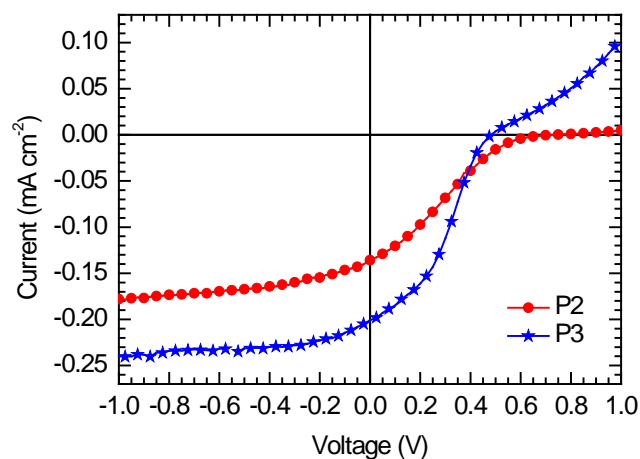


Figure 13. Photocurrent voltage curve of the copolymers under monochromatic illumination at 570 nm.

P2: fits with the dipole model

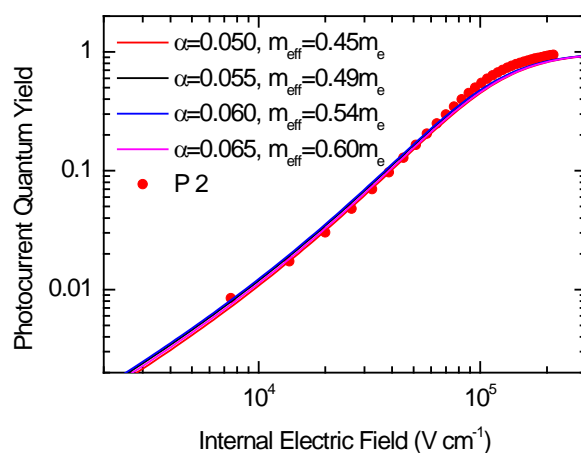


Figure 14. Fits with the dipole model and different fit parameters.¹ It is shown that the data of **P2** can be fitted with increased dipole strength α by increasing the effective mass m_{eff} . All other fit parameters stayed the same. Other fit parameters used (also in the main article): $\tau_0 v_0 \exp(-2\gamma r) = 40$.

Solar cell parameters

Polymer	I_{sc} (mA cm ⁻²)	V_{oc} (V)	FF (%)	PCE (%)
P1	1.56	0.62	24.6	0.23
P2	0.92	0.74	16.4	0.11
P3	1.52	0.50	36.0	0.26

Table 5. Characteristic parameters for the bilayer (co)polymer/ C_{60} solar cells measured under AM 1.5 illumination.

References

1. Wiemer, M.; Nenashev, A. V.; Jansson, F.; Baranovskii, S. D., On the Efficiency of Exciton Dissociation at the Interface between a Conjugated Polymer and an Electron Acceptor. *Appl Phys Lett* **2011**, *99*, 013302.

**Synthesis and characterization of donor-acceptor
copolymers carrying triphenylamine units for
photovoltaic applications**

Katharina Neumann, Mukundan Thelakkat*

**Department of Macromolecular Chemistry I, Applied Functional Polymers, University of Bayreuth,
Universitätsstraße 30, 95440 Bayreuth, Germany*

Published in Proceedings of SPIE

Reproduced with permission from Proceedings of SPIE, 8477, *Organic Photovoltaics XIII* 2012,
84771H, DOI: 10.1117/12.929842

Copyright 2012 Society of Photo Optical Instrumentation Engineers

ABSTRACT

The synthesis and analysis of solution processable polymers for organic solar cells is crucial for innovative solar cell technologies such as printing processes. In the field of donor materials for photovoltaic applications, polymers based on tetraphenylamine (TPA) are well known hole conducting materials. Here, we synthesized two conjugated TPA containing copolymers via Suzuki polycondensation. We investigated the tuning of the energy levels of the TPA based polymers by two different concepts. Firstly, we introduced an acceptor unit in the side chain. The main-chain of this copolymer was built from TPA units. The resulting copolymer 2-(4-((4'-((4-(2-ethylhexyloxy)phenyl)(para-tolyl)amino)biphenyl-4-yl)(para-tolyl)amino)benzylidene)malononitrile **P1** showed a broader absorption up to 550 nm. Secondly, we used a donor-acceptor concept by synthesizing a copolymer with alternating electron donating TPA and electron withdrawing Thieno[3,4-*b*]thiophene ester units. Consequently, the absorption maximum in the copolymer octyl-6-(4-((4-(2-ethylhexyloxy)phenyl)(p-tolyl)amino)phenyl)-4-methylthieno[3,4-*b*]thiophene-2-carboxylate **P2** was red shifted to 580 nm. All three polymers showed high thermal stability. By UV-vis and Cyclic voltammetry measurements the optical and electrochemical properties of the polymers were analyzed.

1. INTRODUCTION

Detailed research has been done in the field of copolymers used in organic photovoltaics. There are various combinations of donor and acceptor monomers to get copolymers with donor-acceptor interactions. This interaction leads to a lowering of the optical gap, mainly via intramolecular charge transfer absorption. Therefore, the copolymer can harvest more efficient light when used in a solar cell. Furthermore, it is possible to adjust the HOMO and LUMO levels of the copolymer, which decides the obtainable photovoltage. Most of the copolymers show hole transport behavior. In this work we want to understand what happens when introducing an acceptor directly in the main chain of the copolymer in contrast to attaching the acceptor moiety in the side chain. This results in two main chain conjugated polymers with different properties. We analyse the optical and electronic properties. The copolymers presented here are based on Triphenylamine (TPA) derivatives. They have been widely studied in the past years as donor molecules.¹ We wanted to combine the good charge carrier transport properties with a very good film forming behavior by synthesizing amorphous copolymers with TPA units.

2. Results

Sec. 2.1 Triphenylamine containing copolymers

Here we synthesized two different TPA containing alternating copolymers by straight forward AA/BB type Suzuki polycondensation. The synthesis will be published elsewhere and the structures are given in **Figure 1**. Firstly, we synthesize an alternating copolymer with a tetraphenylbenzidine (TPD) main chain **P1** with an electron withdrawing dicyanovinyl group. This copolymer was obtained by polymer analogous Knoevenagel condensation of a precursor polymer carrying aldehyde groups in alternating TPA units. Secondly, we prepared a TPA based copolymer with the electron accepting thieno[3,4-*c*]thiophene (TT) comonomer via polycondensation of two monomers. This TT derivative is known to stabilize the quinoid structure. Therefore, we wanted to study the influence of the TT unit in lowering the optical gap of the resulting copolymer.

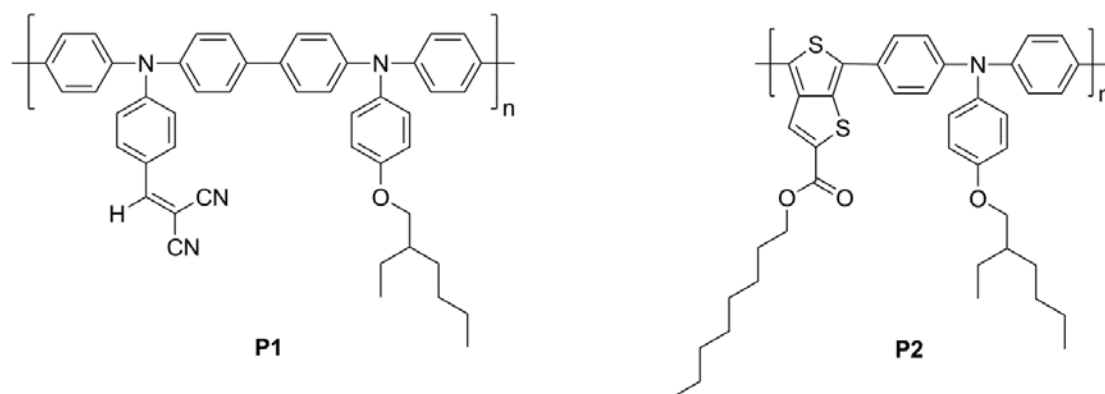


Figure 1. Structures of the copolymers, **P1** with a TPD main chain and an acceptor in the side chain and the copolymer **P2** with an alternating TT unit as electron acceptor and quinoid stabilizing comonomer.

Sec. 1.2 Characterization

The weight-average molecular weights (M_w) of the copolymers **P1** and **P2** were determined by Size exclusion chromatography (SEC). For **P1**, THF and for **P2** chlorobenzene was used as eluent. For calibration, a polystyrene standard was used. **P1** had a M_w of 16030 g/mol with a PDI of 2.60 and **P2** had a M_w of 55360 g/mol with a PDI of 4.91. The values are summarized in **Table 1**.

Table 1. M_w measured by SEC, thermal and optical properties in CHCl_3 solution (0.02 mg/ml) and in film (1 wt.% in CHCl_3) of the copolymers **P1** and **P2**.

Polymer	M_w [g/mol]	PDI	T_g [°C]	$T_{5\%}$ [°C]	$\lambda_{\text{Solution}}$ [nm]	λ_{Film} [nm]
P1	16030	1.35	212	410	371, 468	366, 458
P2	55360	4.91	118	370	298, 366, 500	301, 380, 514

The copolymers showed high thermal stability in thermogravimetric analysis (TGA) with temperatures of 5 % weight loss ranging from 402 to 410 °C. Both copolymers were analyzed by Differential Scanning Calorimetry (DSC). The copolymers show glass transition temperatures at 212 °C and 118 °C for **P1** and **P2** respectively (see **Table 1**). Thus, the copolymers are amorphous and have an excellent film forming behavior without any crystallization effects.

The optical characterization of the copolymers is done by UV-vis spectroscopy in film (**Figure 2**). The spectrum of **P1** clearly shows the transition of the TPD backbone at 376 nm. Additionally, a new band assigned to a charge transfer band at 468 nm occurs. Copolymer **P2** shows two transitions for the TPA (366 nm) and the TT (298 nm) in the backbone. Also a red shifted broad band occurs at 514 nm due to a strong donor acceptor interaction. Additionally, the stronger oscillator strength of copolymer **P2** substantiates that a stronger CT interaction is present.

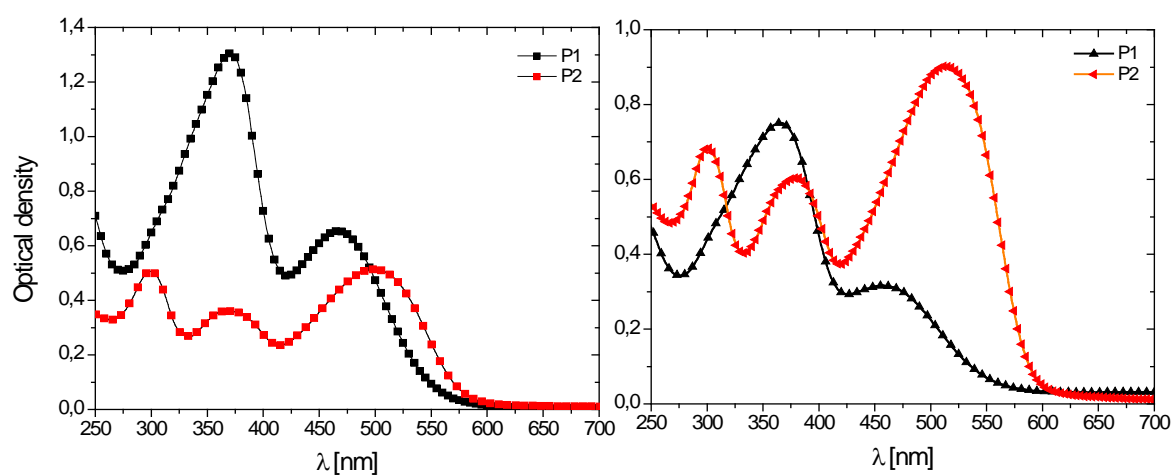


Figure 2. UV-vis spectra of **P1** and **P2** in solution (2 mg/ml in CHCl_3) and in film spin coated from 1 wt % solution in CHCl_3 . **P2** shows the transition of the TPD backbone at 376 nm. The CT band of **P3** is red shifted due to a stronger donor-acceptor interaction.

We also investigated the electronic properties of our copolymers with Cyclic voltammetry (CV). The measurements were carried out in DCM with Ferrocene as reference. The HOMO levels of the copolymers are -5.09 eV and -4.94 eV for **P1** and **P2** respectively. Copolymer **P2** shows a

lower optical gap of 2.10 eV compared to **P1** with an optical gap of 2.24 eV. Therefore, the LUMO level of **P1** is -2.85 eV and -2.84 eV for **P2**.

Tabelle 1. Oxidation Potential vs. Ferrocene (Fc) and HOMO values from CV measurements. LUMO values calculated by the optical gap from UV vis measurements.

Polymer	E_{ox1} vs. Fc [eV]	HOMO [eV]	E_g [eV]	LUMO [eV]
P1	0.29	-5.09	2.24	-2.85
P2	0.14	-4.94	2.10	-2.84

In conclusion, we showed the comparison of two different TPA containing copolymers. One copolymer was synthesized with an electron acceptor in the side chain. The other copolymer had an electron withdrawing comonomer directly in the main chain. These two copolymers are promising materials for the application in organic field effect transistors and other organic electronic applications.

ACKNOWLEDGEMENT

We acknowledge financial support from EU project LARGECELLS (Grant No. 261936) and KN acknowledges support from BayEFG for a stipend.

REFERENCES

1. M. Thelakkat, *Macromol. Mater. Eng.* **2002**, 287, 442–461.

List of publications

- K. Neumann, M. Thelakkat; “Synthesis and characterization of donor-acceptor copolymers carrying triphenylamine units for photovoltaic applications”, *Proceedings of SPIE 8477, Organic Photovoltaics XIII* 201, 84771H.
- P. Goldberg-Oppenheimer; D. Kabra; S. Vignolini; S. Hüttner; M. Sommer; K. Neumann; M. Thelakkat; U. Steiner; “Hierarchical Orientation of Crystallinity by Block-Copolymer Patterning and Alignment in an Electric Field“, *Chemistry of Materials* 2013, 25(7), 1070.
- K. Neumann, C. Schwarz, A. Köhler, M. Thelakkat; “Influence of the Excited-State Charge-Transfer Character on the Exciton Dissociation in Donor-Acceptor Copolymers“, *Journal of Physical Chemistry: C* 2014, 118, 27-36.
- K. Neumann, M. Thelakkat, “Perovskite Solar Cells Involving Poly(tetraphenylbenzidine)s: Investigation of Hole Carrier Mobility, Doping effects and Photovoltaic Properties“, *RSC Advances*, 2014, Accepted Manuscript, DOI: 10.1039/C4RA05564K.

Danksagung

An dieser Stelle bedanke ich mich herzlich bei allen, die direkt oder indirekt zum Gelingen dieser Arbeit beigetragen haben.

Als erstes möchte ich mich ganz besonders bei meinem Betreuer Prof. Mukundan Thelakkat bedanken, der mir die Möglichkeit geboten hat an diesem spannenden und vor allem abwechslungsreichen Thema zu arbeiten. In der Zeit meiner Doktorarbeit hat er mich darin unterstützt mich fachlich als auch persönlich weiterzuentwickeln. Zudem empfand ich die Atmosphäre in der Arbeitsgruppe als sehr positiv. Besonders die vielen Gelegenheiten an internationalen Konferenzen mit eigenem Beitrag teilnehmen zu dürfen sind keine Selbstverständlichkeit. Herzlichen Dank!

Für die finanzielle Unterstützung im Rahmen eines Graduiertenstipendiums möchte ich mich bei der Universität Bayern e. V. bedanken. Dies erlaubte mir die Teilnahme an Konferenzen und meinen Auslandsaufenthalt in Melbourne, Australien.

Außerdem bedanke ich mich beim Graduiertenkolleg „Photophysik synthetischer und multichromophorer Systeme“ für die Möglichkeit mit den Doktoranden aus den anderen Fachrichtungen in Kontakt zu kommen, woraus viele hilfreiche Diskussionen entstanden sind.

Bei Prof. Anna Köhler und Dr. Christian Schwarz vom Lehrstuhl Experimentalphysik II bedanke ich mich für die erfolgreiche und interessante Zusammenarbeit. Beide waren eine sehr große Hilfe für das Gelingen dieser Arbeit. Mein Dank gilt auch dem gesamten Arbeitskreis, die mich stets bei vielen kleinen Arbeitsschritten im Messlabor unterstützt haben. Besonders danke ich hier Frank Schirmer für die Hilfe bei der Substratherstellung und beim Aufdampfen!

Weiterhin bedanke ich mich bei Prof. Ralf Moos und Isabella Marr vom Lehrstuhl Funktionsmaterialien für die Charakterisierung meiner Polymere als aktive Sensormaterialien, welches ohne ihr Zutun nicht möglich gewesen wäre.

Außerdem möchte ich mich bei Sabrina Willer bedanken, die mich während ihrer Zulassungsarbeit tatkräftig mit Synthesen unterstützt hat.

Ganz besonders möchte ich allen Mitarbeitern des Lehrstuhls Makromolekulare Chemie I danken! Die schöne Atmosphäre, Hilfsbereitschaft und Offenheit haben mir die Zeit am Lehrstuhl sehr angenehm gemacht. Ich werde an diese Zeit sehr gerne zurück denken und immer in sehr guter Erinnerung behalten. Die vielen, hilfreichen Diskussionen und Anregungen

sei es im Labor oder im Kaffeezimmer haben mir geholfen den Doktorandenalltag zu bewältigen. Nicht weniger hat der viele Spaß, den wir miteinander am Lehrstuhl hatten zum Erfolg der Arbeit beigetragen! Ganz besonders danke ich hier Anne Neubig, Andreas Ringk, Tina Weller, Andreas Lang, Christian Bartz, Florian Wieberger, Julia Singer, Ruth Lohwasser und dem gesamten Flashgames-Labor (Johannes Heigl, Christian Probst, Andreas Haedler). Vielen Dank auch an Katja Gräf, mit der ich viele erfolgreiche und lustige Stunden bei der Erforschung der Perovskit-Solarzellen gehabt habe, sowie Tanaji Gujar, der ein toller Nachfolger von ihr geworden ist. Besonders danke ich Helga Wietasch für die beste Laboratmosphäre, die man sich vorstellen kann! Außerdem für viele kleine Hilfen im Laboralltag. Vor allem gilt mein Dank auch den Gerätebetreuern und Technikern, die immer mit Rat und Tat zur Hilfe gestanden haben. Danke auch an Petra Weiss und Christina Wunderlich für die Unterstützung bei organisatorischen und bürokratischen Angelegenheiten während der ganzen Zeit.

Zuletzt gilt mein größter Dank meiner Familie! Meiner Mutter Angelika, meinem Vater Werner und meinem Freund Christian! Danke, an meine Eltern, dass sie mir immer die Freiheit gelassen haben meine Entscheidungen selbst zu treffen und mich dabei bedingungslos zu unterstützen. Ihr alle drei habt mir in allen Situationen helfend zur Seite gestanden. Ohne Euch wäre all dies nicht möglich gewesen! Besonders danke ich auch meiner Oma, die mich dazu ermutigt hat immer weiter zu lernen und zu arbeiten, um meine Ziele zu erreichen. Auch Margit und Werner gilt mein herzlichster Dank. Außerdem danke ich Elfriede und Hans sowie Ulrike für ihre Unterstützung.

DANKE!

(Eidesstattliche) Versicherungen und Erklärungen

(§ 8 S. 2 Nr. 6 PromO)

Hiermit erkläre ich mich damit einverstanden, dass die elektronische Fassung meiner Dissertation unter Wahrung meiner Urheberrechte und des Datenschutzes einer gesonderten Überprüfung hinsichtlich der eigenständigen Anfertigung der Dissertation unterzogen werden kann.

(§ 8 S. 2 Nr. 8 PromO)

Hiermit erkläre ich eidesstattlich, dass ich die Dissertation selbständig verfasst und keine anderen als die von mir angegebenen Quellen und Hilfsmittel benutzt habe.

(§ 8 S. 2 Nr. 9 PromO)

Ich habe die Dissertation nicht bereits zur Erlangung eines akademischen Grades anderweitig eingereicht und habe auch nicht bereits diese oder eine gleichartige Doktorprüfung endgültig nicht bestanden.

(§ 8 S. 2 Nr. 10 PromO)

Hiermit erkläre ich, dass ich keine Hilfe von gewerbliche Promotionsberatern bzw. -vermittlern in Anspruch genommen habe und auch künftig nicht nehmen werde.

Bayreuth, den 30.06.2014

Katharina Neumann